

Scientific report

SAC/EP SA/CVD/SR/2020-04

**Stability assessment of point and distributed targets for
satellite and aerial SAR sensors**

Calibration and Validation Division (CVD)

Earth, Ocean, Atmosphere, Planetary Sciences & Applications Area

(EP SA)

Space Applications Centre (ISRO)

Ahmedabad – 380015

&

Institute of Technology,

NIRMA University,

Ahmedabad.

July, 2020

CAL-VAL Team

1. Space Applications Centre (SAC-ISRO), Ahmedabad

Dr. Shweta Sharma- Principal Investigator

Mr. Saurabh Tripathi- Co-Principal Investigator

Dr. A K Mathur- Coordinator, Former Head, CVD/EPISA

Dr. K. N. Babu – Head, CVD/EPISA

2. Nirma University, Ahmedabad

Dr. P. R. Patel- Co-Principal Investigator

B. Sowkhya- Junior Research Fellow (JRF)

DOCUMENT CONTROL SHEET

| | |
|-----------------------------|--|
| 1. Report No. | SAC/EPESA/CVD/SR/2020-04 |
| 2. Publication date | July -2020 |
| 3. Title and subtitle | Stability assessment of point and distributed targets for satellite and aerial SAR sensors |
| 4. Type of report | Scientific |
| 5. Number of pages | 106 |
| 6. Authors | CAL-VAL Team |
| 7. Originating unit | CVD/EPESA/ Space Applications Centre, ISRO |
| 8. Abstract | <p>In this study, assessment of the potential of point target sites (Surat basin, Australia and Rosamond calibration array) and distributed target sites (Amazon rainforest and Canadian Boreal forest) as calibration sites for NISAR was carried out.</p> <p>Results of the temporal stability assessment of the radiometric calibration of Sentinel-1 and radiometric and polarimetric calibration of UAVSAR L-band data using point targets and distributed targets are presented here. Temporal stability assessment of the Radar Cross Section and image quality parameters derived from the SAR response of the deployed corner reflector array at Surat basin, Australia and Rosamond calibration site at California was carried out. Three dates (25th July, 06th August and 18th August 2019) SLC data of Sentinel-1B C-band, and full-polarimetric SLC data of UAVSAR (L-band) of 28 May 2019, have been used for the analysis. Gamma naught stability assessment of Amazon rainforest and Boreal forest during the time period 2015-2017 was also carried out. Intra-annual and inter-annual comparisons of gamma naught values were done and results are reported here for both C- and L-band using available SAR data of Sentinel -1A, 1B and ALOS-2 PALSAR mosaic data.</p> |
| 9. Key words | Radiometric and Phase calibration, Polarimetric calibration, cross talk, channel imbalance, SAR calibration, UAVSAR |
| 10. Security classification | Unrestricted |
| 11. Distribution statement | General |

Table of Contents

1 Introduction 9

2 Objectives 11

3 Study Area 11

4 Data Used 15

5 Methodology 18

6 Results & Discussion 32

7 Summary and Conclusions 101

Acknowledgements 104

References 104

I. List of Figures

| | |
|---|----|
| FIGURE 1: DEPLOYED CORNER REFLECTORS (1.5M) AT SURAT BASIN CALIBRATION SITE, AUSTRALIA. | 11 |
| FIGURE 2: GOOGLE EARTH IMAGE SHOWING STUDY AREA FOOTPRINT (LEFT IMAGE) AND DISPLAY OF DEPLOYED CORNER REFLECTORS AT ROSAMOND DRY LAKE BED (RIGHT IMAGE). | 12 |
| FIGURE 3: SLC IMAGE OF HH-POL SHOWING CORNER REFLECTORS DEPLOYED AT ROSAMOND DRY LAKE | 13 |
| FIGURE 4: STATES OF AMAZONAS - AMAZON RAIN FOREST | 14 |
| FIGURE 5: ONTARIO PROVINCE, CANADA BOREAL FOREST. | 15 |
| FIGURE 6: IMPULSE RESPONSE FUNCTION IN RANGE AND AZIMUTH DIRECTION © (DADHICH, ET AL. 2018) | 20 |
| FIGURE 7: FLOW-CHART SHOWING METHODOLOGY | 31 |
| FIGURE 8: LEFT IMAGE SHOWS THE SELECTION OF WATER PIXELS BASED ON WATER THRESHOLD AND RIGHT IMAGE SHOW THE SELECTION OF WET LAND SOIL AND WATER PIXELS BASED ON INTENSITY VALUES. | 32 |
| FIGURE 9: SCR OF EACH CR ESTIMATED USING SLC HH POL DATA | 35 |
| FIGURE 10: DIFFERENCE BETWEEN THEORETICAL RCS AND ESTIMATED RCS FOR HH POL..... | 36 |
| FIGURE 11: INCIDENCE ANGLE OF EACH CR OBTAINED FROM SLC HH POL DATA. | 36 |
| FIGURE 12: IRF FOR CR19 ON 25 TH JULY, 06 TH AUG, 18 TH AUGUST 2019 USING SLC HH POLARIZATION DATA..... | 38 |
| FIGURE 13: IRF FOR CR27 ON 25 TH JULY, 06 TH AND 18 TH AUGUST 2019 USING SLC HH POLARIZATION DATA. | 39 |
| FIGURE 14: IRF FOR CR30 ON 25 TH JULY, 06 TH AND 18 TH AUGUST 2019 USING SLC HH POLARIZATION DATA | 40 |
| FIGURE 15: IRF FOR CR36 ON 25 TH JULY, 06 TH AND 18 TH AUGUST 2019 USING SLC HH POLARIZATION DATA. | 41 |
| FIGURE 16: IRF FOR CR37 ON 25 TH JULY, 06 TH AND 18 TH AUGUST 2019 USING SLC HH POLARIZATION DATA. | 42 |
| FIGURE 17: IRF FOR CR38 ON 25 TH JULY, 06 TH AND 18 TH AUGUST 2019 USING SLC HH POLARIZATION DATA. | 43 |
| FIGURE 18: IRF FOR CR40 ON 25 TH JULY, 06 TH AND 18 TH AUGUST 2019 USING SLC HH POLARIZATION DATA..... | 44 |
| FIGURE 19: IRF FOR CR41 ON 25 TH JULY, 06 TH & 18 TH AUGUST 2019 USING SLC HH POLARIZATION DATA. | 45 |
| FIGURE 20: IRF FOR CR42 ON 25 TH JULY, 06 TH & 18 TH AUGUST 2019 USING SLC HH POLARIZATION DATA. | 46 |
| FIGURE 21: DIFFERENCE BETWEEN ESTIMATED AND SPECIFIED RESOLUTION IN RANGE (2.329 M) AND AZIMUTH (14.068 M). | 47 |
| FIGURE 22: PEAK TO SIDE LOBE RATIO OBTAINED IN RANGE AND AZIMUTH DIRECTION USING SLC HH POL. DATA..... | 48 |
| FIGURE 23: INTEGRATED SIDE LOBE RATIO OBTAINED IN RANGE AND AZIMUTH DIRECTION USING SLC HH POL. DATA | 49 |
| FIGURE 24: DEVIATION FROM THEORETICAL RCS FOR CR ARRAY (HH AND VV POL.) | 52 |
| FIGURE 25: PEAK POWER VALUES FOR HH AND VV POL. IN LINEAR AMPLITUDE UNITS | 52 |
| FIGURE 26: PEAK POWER DIFFERENCE BETWEEN HH AND VV POL. IN LINEAR AMPLITUDE UNITS | 53 |
| FIGURE 27: PHASE DIFFERENCE HH-VV POL | 54 |
| FIGURE 28: LOCATION OF CR'S IN SLC IMAGE OF HH POL..... | 55 |
| FIGURE 29: IMPULSE RESPONSE FUNCTION OF CR'S USING SLC IMAGE OF HH POL | 58 |
| FIGURE 30: IMPULSE RESPONSE FUNCTION OF CR'S USING SLC IMAGE OF VV POL | 61 |
| FIGURE 31: POLARIMETRIC SIGNATURE OF CORNER REFLECTOR IN IDEAL CASE: CO-POLARIZATION SIGNATURE OF CORNER REFLECTOR BEFORE (AFTER) RADIOMETRIC AND PHASE CALIBRATION SHOWN IN LEFT (RIGHT) PANEL. ©(ALEXANDER, BRUCE AND BRIAN 2014)..... | 64 |
| FIGURE 32: POLARIMETRIC SIGNATURES OF TRIANGULAR TRIHEDRAL CORNER REFLECTOR AFTER RADIOMETRIC AND PHASE CALIBRATION. | 69 |
| FIGURE 33: LOCATION OF CR'S IN SLC IMAGE OF HV POL..... | 70 |
| FIGURE 34: IMPULSE RESPONSE OF CR USING SLC IMAGE OF HV | 73 |
| FIGURE 35: POLARIMETRIC SIGNATURE OF TRIANGULAR TRIHEDRAL CORNER REFLECTOR (IDEAL CASE) © (ABHISEK, SHASHI AND VALENTYN 2019)..... | 74 |
| FIGURE 36: POLARIMETRIC SIGNATURES OF EACH CR AFTER CROSS TALK AND CHANNEL IMBALANCE CALIBRATION..... | 78 |
| FIGURE 37: THE SLC/MLC (LEFT/RIGHT) TILE OF UAVSAR L-BAND DATA SHOWING WINDMILLS..... | 79 |
| FIGURE 38: SHOWING WINDMILLS IN GOOGLE EARTH IMAGE | 80 |
| FIGURE 39: IMPULSE RESPONSE FUNCTION OF WINDMILLS USING SLC HH POL. DATA..... | 84 |

| | |
|---|-----|
| FIGURE 40: INTER-ANNUAL GAMMA NAUGHT VALUES OF AMAZON IN Co & CROSS-POL USING C BAND..... | 85 |
| FIGURE 41: INTRA-ANNUAL GAMMA NAUGHT VALUES OF RAINY (YELLOW) AND DRY (BLUE) SEASONS IN CO & CROSS-POL USING C BAND..... | 87 |
| FIGURE 42: ANNUAL MEAN GAMMA NAUGHT VALUES OF AMAZON IN CO & CROSS-POL USING L BAND..... | 88 |
| FIGURE 43: ANNUAL QUANTITATIVE COMPARISON OF L (BLUE) AND C (ORANGE) BAND'S MEAN GAMMA NAUGHT VALUES IN Co & CROSS-POL. | 89 |
| FIGURE 44: MONTHLY VARIATION OF AVERAGE GAMMA NAUGHT IN VV & VH POL. USING C BAND. | 92 |
| FIGURE 45: SEASONAL VARIATION GRAPH FOR SUMMER AND WINTER IN VV & VH POL. USING C BAND DATA..... | 94 |
| FIGURE 46: MEAN GAMMA NAUGHT IN HH & HV POL USING L BAND | 96 |
| FIGURE 47: COMPARISON OF C AND L BAND, ANNUAL GAMMA NAUGHT IN Co & CROSS-POL | 97 |
| FIGURE 48: RUN OF ERS& JERS BACKSCATTER IN SPARSE (SOLID LINE) AND DENSE FOREST (DASHED LINE) ©(SANTORO 2003), STUDY REGION: KATTABOLE, SWEDEN (PART OF BOREAL FOREST). | 99 |
| FIGURE 49: BOREAL FOREST SEASONAL REFLECTIVITY ©(SATISH K SRIVASTAVA N.D.) | 100 |

II. List of Tables

| | |
|---|----|
| TABLE 1: DATA ATTRIBUTES | 15 |
| TABLE 2: LIST OF PRECISION DATA FILES AND RADAR PARAMETERS OF SLC IMAGERY | 16 |
| TABLE 3: LIST OF PRECISION DATA FILES AND RADAR PARAMETERS OF MULTI LOOK IMAGERY | 16 |
| TABLE 4: DETAILS OF SENTINEL-1 DATA | 17 |
| TABLE 5: DETAILS OF ALOS 2 PALSAR 2 DATA | 18 |
| TABLE 6: DETAILS OF CLUTTER USED FOR RCS ESTIMATION | 33 |
| TABLE 7: CORNER REFLECTOR LOCATIONS IN SLC IMAGE FOR DIFF. DATES | 34 |
| TABLE 8: ESTIMATION OF SCR FOR EACH CR | 34 |
| TABLE 9: ESTIMATION OF RCS AND ITS DIFFERENCE | 34 |
| TABLE 10: ESTIMATED RANGE AND AZIMUTH RESOLUTIONS | 47 |
| TABLE 11: ESTIMATED PSLR IN RANGE AND AZIMUTH DIRECTION | 48 |
| TABLE 12: ESTIMATED ISLR IN RANGE AND AZIMUTH DIRECTION | 49 |
| TABLE 13: ATTRIBUTES USED TO CALCULATE RCS OF EACH CR WITH RESPECT TO INCIDENCE AND AZIMUTH ANGLE | 50 |
| TABLE 14: DETAILS OF CLUTTER AND DEVIATION OF RCS FROM THEORETICAL VALUE | 51 |
| TABLE 15: PEAK PHASE VALUES FOR HH AND VV POLARIZATION | 53 |
| TABLE 16: RANGE AND AZIMUTH RESOLUTION ESTIMATED FROM IRF OF THE POINT TARGETS | 54 |
| TABLE 17: CALCULATED TARGET ENERGY VALUES AFTER SUBTRACTION OF CLUTTER FOR QUAD POL | 62 |
| TABLE 18: ESTIMATION OF CO CHANNEL IMBALANCE (F) | 63 |
| TABLE 19: ESTIMATION OF CROSS CHANNEL IMBALANCE (G) | 63 |
| TABLE 20: ESTIMATED PHASE BIAS IN TRANSMITTER AND RECEIVER FOR CO-POL AND CROSS-POL CHANNELS | 64 |
| TABLE 21: ESTIMATION OF CROSS TALK AND CHANNEL IMBALANCE USING QUEGAN ALGORITHM | 73 |
| TABLE 22: RANGE AND AZIMUTH RESOLUTION AT 3dB WIDTH USING OPPORTUNISTIC TARGETS (WINDMILLS) | 80 |

1 Introduction

Synthetic Aperture Radar (SAR) was first developed for long range mapping and surveillance, geological mapping and monitoring Earth surface (*Freeman, et al., 1994*). SAR is a progressive remote sensing technology used to retrieve the characteristics of Earth's surface targets, which also has capabilities to acquire the data during all weather conditions, day and night imaging capability. The SAR sensors are designed for stable operations, equipped with capabilities to capture multi-frequency, multi-polarized data with different acquisition modes such as Interferometric swath mode (IW), Extra wide swath (EW) mode, Ground Range Detection (GRD) mode. SAR is an active microwave radar system, transmitting horizontal or vertical polarized signal towards the target and receives backscattered energy from the target. Single polarization radar system transmits horizontal (HH) or vertical (VV) polarization signal and receive signal in the same polarization. In case of dual pol. or full pol. radar system, the signal is transmitted alternatively in both the polarization channels but receives simultaneously the signal from the target in both the polarization channels. In hybrid pol. radar system, circular polarized pulse either left or right circular signal is transmitted in horizontal or vertical direction, and backscatter is received in both the polarized channels. These unique microwave characteristics i.e., linear polarization, circular polarization, etc., helps in retrieving additional information about the target. The pixel imaged contains both amplitude and phase information which can be related to the geophysical parameter(s) of the target. Usually the amplitude information is used to extract properties of the imaged target by the radar while phase information is being used in Interferometric SAR and Polarimetric SAR data applications.

The data quality and applications using space-based SAR system are rapidly improved even with un-calibrated images in the past. Though in earlier years radiometric calibration of SAR image was secondary (*Freeman, et al., 1994*), with rapid development in SAR sensors, geometric, radiometric and polarimetric calibration has become mandatory. The radiometric calibration is relating the radar backscatter response of the target to the radar backscatter value of the target within the SAR image. The radiometric calibrated images are required; for comparison with different sensor, extraction of geophysical properties from the target response. Recent advances in calibration techniques made SAR data, represents normalized radar cross section (RCS). The advantage of different polarized SAR data is achieved, unless the different channels can be

compared with one another (*Freeman, et al., 1998*). While in case of Polarimetric radar (HH, HV, VH, VV) data gives amplitude and phase information from the behaviour of the scattered waves from a target. The distortion may occur in the phase and amplitude information of a target.

Usually in dual polarized sensors, errors such as fluctuations in the transmitted power and receiver gain, illumination antenna pattern and system noise are observed. The mentioned errors are accounted in radiometric calibration correction. To extract the behaviours and properties of the target, normalization is required to estimate radar cross section (RCS) or backscatter coefficient on a pixel by pixel basis for targets being imagined by the radar and also known as radiometric calibration (*Freeman, et al., 1998*). To verify the accuracy of the dual pol data, radiometric calibration is made and ensured that the data is calibrated with known calibrated targets such as corner reflectors or transponders (*Freeman, et al., 1994*). While in case of airborne or spaceborne quad (full) pol. SAR data, Channel imbalance and Cross talk are the errors observed. The parameter which obstructs this comparability of measurements from different polarisation channels is known as channel imbalance. The channel imbalance represents both amplitude imbalance and phase imbalance (*Abhisek, Shashi and Valentyn 2019*). To reduce the undesirable attenuation by a polarized channel on the measurements of other polarized channels, isolation of the polarization channels is required. Cross talk is defined as distortions in the polarimetric data due to improper channel isolation. To minimize the error in RCS estimation for PolSAR data, radiometric calibration has to be applied. To ensure the cross-pol reciprocity and to minimize the error due to imperfect isolation of polarimetric channels, calibration techniques for minimisation of crosstalk and channel imbalance are adopted (*Freeman, et al., 1995*).

The SAR image quality depends on spatial resolution, PSLR and ISLR of the target response (*Dadhich, et al., 2018*). Spatial resolution in azimuth and range direction, Peak and Integrated side lobe ratio's (PSLR & ISLR) are obtained during radiometric calibration. PolSAR data assumes backscatter symmetry and is based on statistical comparison of the data with ideal theoretical models (*Pottier et al., 2007*)

2 Objectives

The objectives of this scientific report are:

- Stability analysis for corner reflectors deployed in Surat Basin, Australia.
- Radiometric and Polarimetric calibration of airborne UAVSAR L-band data.
- Gamma Naught stability analysis carried out for Amazon Rainforest and Canadian Boreal forest.

3 Study Area

3.1 Stability analysis for corner reflectors deployed in Surat Basin, Australia

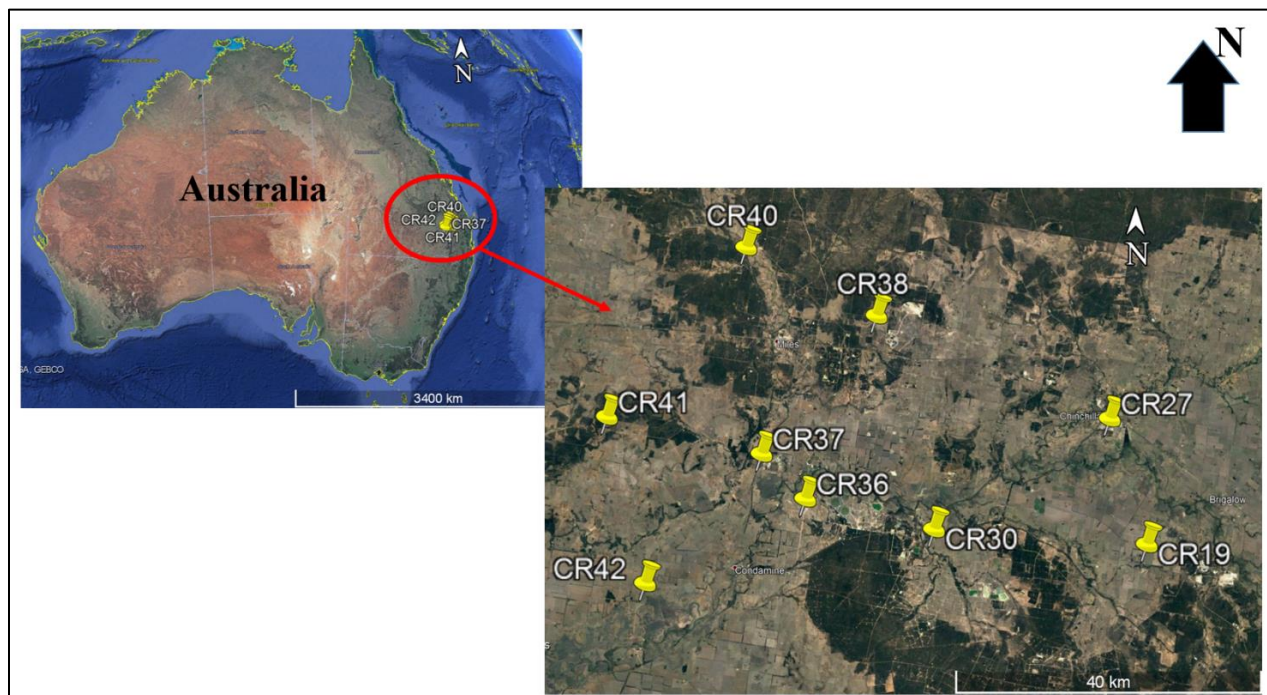


Figure 1: Deployed corner reflectors (1.5m) at Surat basin calibration site, Australia.

The corner reflectors have been deployed in paddocks belongs to a sheep grazing company near Gunning, North of Canberra which is approximately 55km (Figure 1) situated in North-Eastern Surat basin in Queensland, Australia. The calibration site is characterized by hilly and surrounded with trees, dense vegetation, buildings, metallic boundary fences and infrastructure. These corner reflectors are maintained by the Australian Geophysical Observing System (AGOS) and are used for calibration of Synthetic Aperture Radar (SAR) sensors mainly X and C band. This facility offers reliable means to perform ongoing radiometric, geometric, and impulse response

measurements for calibration of Synthetic Aperture Radar (SAR) instruments on space borne or airborne platforms (*Garthwaite, et al. 2015*).

3.2 Radiometric and polarimetric calibration of airborne UAVSAR L-band data, Rosamond, USA

The Rosamond dry lake placed between Antelope Valley and Mojave Desert in the southern California state, USA (Figure 2). It is naturally formed dry lakebed with a large flat surface of 35km². This site is best suited for calibration purpose, because the study area is characterised by least amount of vegetation and the surface has curvature variation of less than 40 cm (*Abhisek, Shashi and Valentyn 2019*). At the dry lake, array of trihedral corner reflectors of different sizes (4.8 m, 2.4 m, 0.7 m) have been deployed for calibration purpose (L band, P band and Ka band sensor respectively). For L band there are 10 CR with East facing (350 heading) and 13 CR with West facing (-170 heading) with respect to North (*Ronald, Elaine and Alex Fore 2015*). Figure 3 shows the response of trihedral corner reflectors of SLC image (HH-pol.)

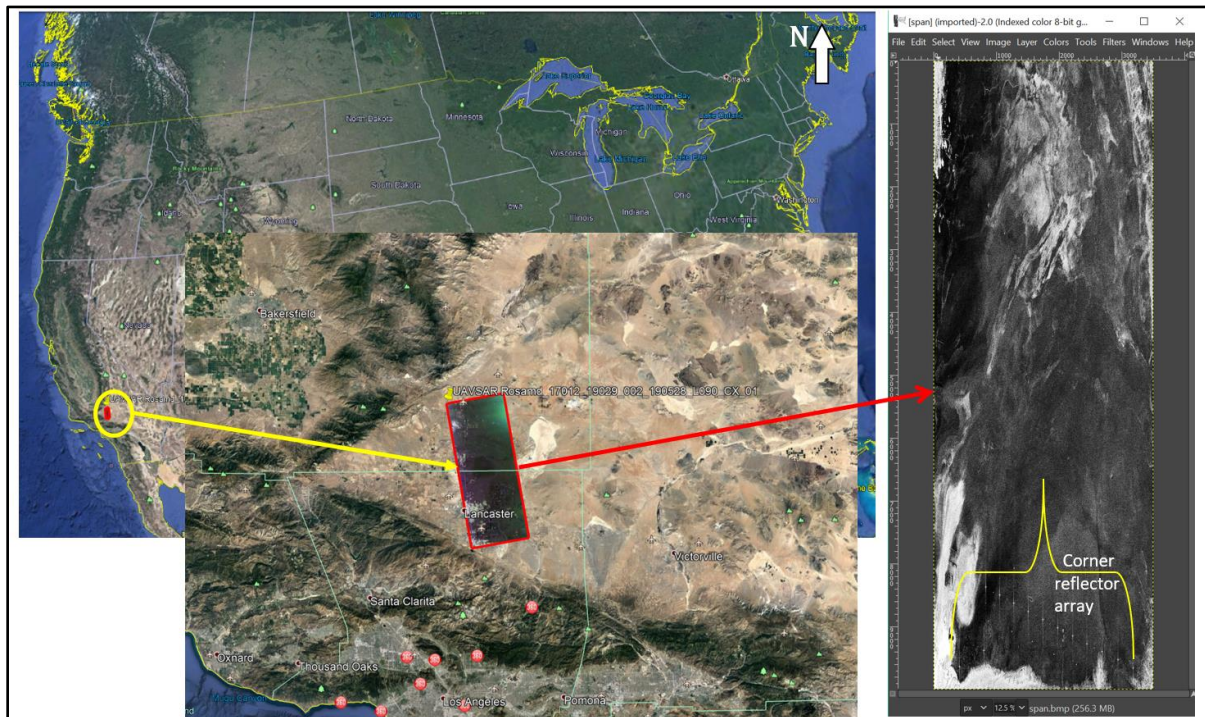


Figure 2: Google Earth image showing study area footprint (left image) and display of deployed corner reflectors at Rosamond dry lake bed (right image).

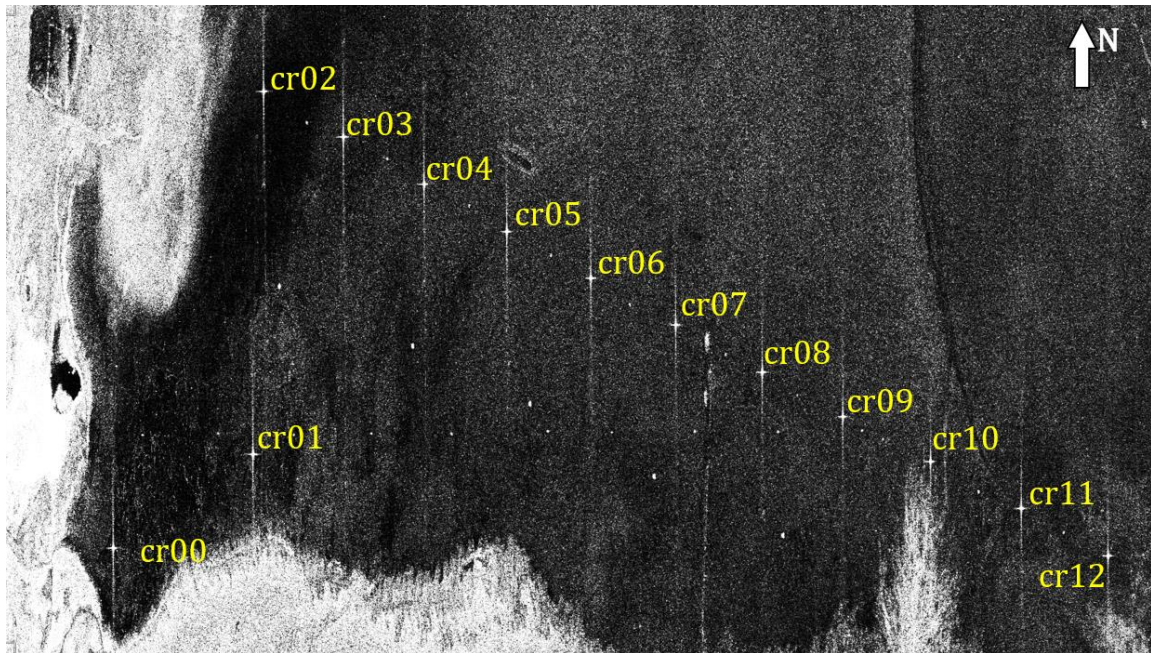


Figure 3: SLC image of HH-pol showing corner reflectors deployed at Rosamond dry lake

3.3 Gamma Naught stability analysis over Amazon Rainforest and Canadian Boreal Forest

Amazon Rainforest is widely used as distributed target site for Synthetic Aperture Radar (SAR) calibration (Figure 4). Amazon Rainforest is a moist broadleaf forest in the Amazon biome that covers most of the Amazon basin of South America. It is geographically located at **3.4653° S, 62.2159° W**. This basin encompasses 7,000,000 km² (2,700,000 sq. mi), of which 5,500,000 km² (2,100,000 sq. mi) are covered by the rainforest. This region includes territory belonging to nine nations. The majority of the forest is contained within Brazil, with 60% of the rainforest, followed by Peru with 13%, Colombia with 10% and with minor amounts in Venezuela, Ecuador, Bolivia, Guyana, Suriname and French Guiana. Although it is a natural dense rainforest, deforestation and fires are reducing the current forest coverage, and also widespread tree mortality. The response of this site in radar data shows a remarkably high degree of homogeneity over a large area, but still it has some spatial and temporal variability due to deforestation effects and seasonal variability which impacts the SAR calibration accuracy.

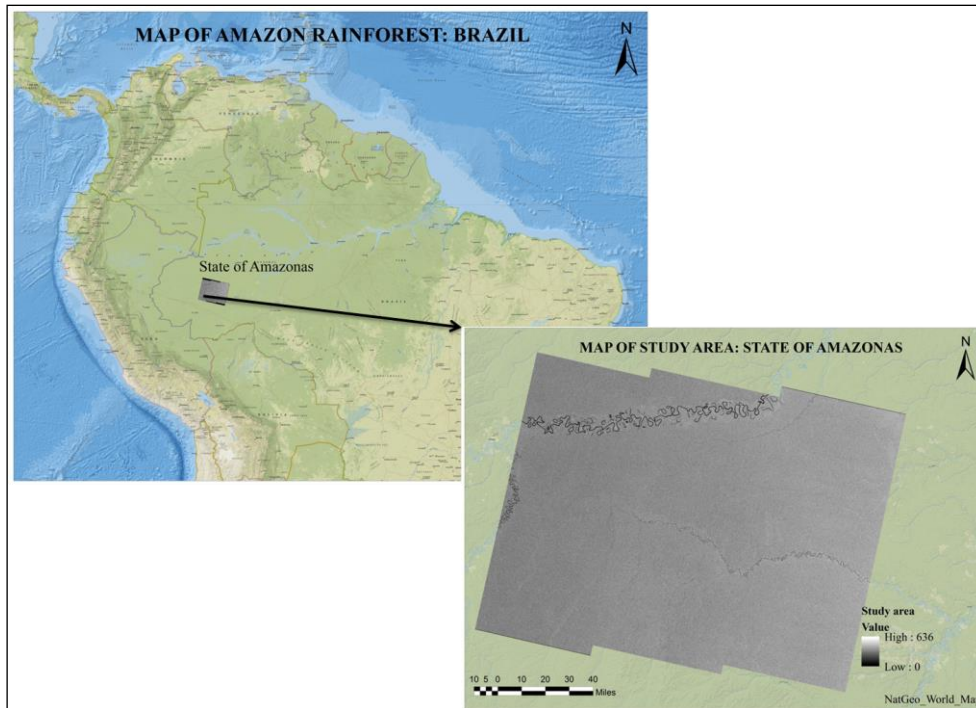


Figure 4: States of Amazonas - Amazon Rain Forest

Figure 5 shows the Ontario province situated in Canada Boreal Forest. Boreal forests have both a fundamental economic and environmental role. Boreal zone consists of Sweden, Finland, Russia and Canada. Boreal forests cover almost the entire land surfaces in the northern hemisphere between 60° N and 70° N, reaching 50° N in East Siberia and West Canada (SANTORO 2003). Canada's Boreal forest comprises about one third of the circumpolar boreal forest that ringed the Northern Hemisphere, mostly north of the 50° N. The area is dominated by coniferous forests, particularly spruce, with vast wetlands, mostly bogs and fens. The boreal forest zone consists of closed crown conifer forests with a conspicuous deciduous element (Canadian Boreal forest n.d.) The boreal region is far from being “just” a cold area. Temperatures lie above and below 0° C. The monthly average winter temperatures decrease and the summer average increase. Precipitation is mainly in the form of snowfall but is remarkably less frequent. As a consequence, the growing season for the vegetation is longer in Sweden and Finland, although the growth rate per year is bigger in Siberia. (SANTORO 2003).

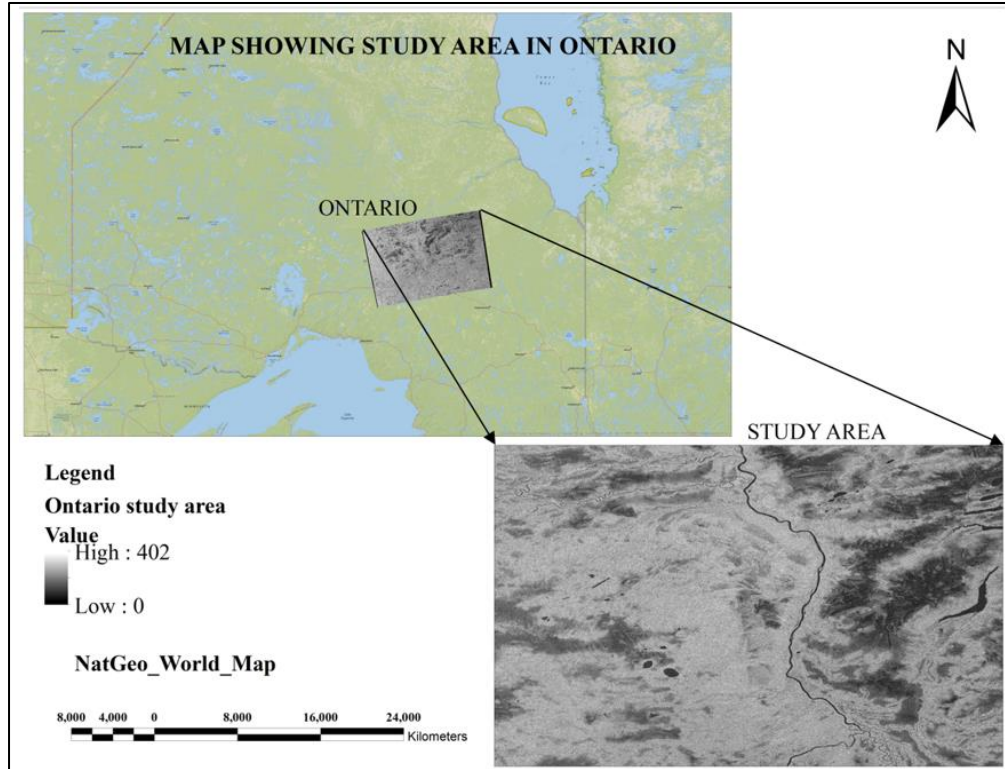


Figure 5: Ontario province, Canada Boreal forest.

4 Data Used

4.1 Stability analysis for corner reflectors deployed in Surat Basin, Australia

The following table 1 gives the information of the data used for this study and it is downloaded from Alaska data facility- ASF (<https://search.asf.alaska.edu/#/>).

Table 1: Data Attributes

| | | | |
|----------------------|---------------------------------------|------------------------|---|
| Satellite | Sentinel-1B | Data type | SLC |
| Date of Acquisition | 25/07/2019, 06/08/2019 & 18/8/2019 | Polarization | HH |
| Beam mode | Interferometric Wide (IW) | Latitude, Longitude | 27 ⁰ 26'2.4" S; 148 ⁰ 47'52.8" E |
| Frequency | 5.405 GHz, C-band | Range Resolution | 2.33 meters |
| Looking direction | Right look | Azimuth Resolution | 14.066 meters |

| | | | |
|-----------------|----------------|------------------------|----------|
| Incidence angle | 33.406 degrees | Data Path & Data Frame | 45 & 684 |
|-----------------|----------------|------------------------|----------|

4.2 Data used for radiometric and polarimetric calibration of airborne UAVSAR L-band data.

Uninhabited Aerial Vehicle Synthetic Aperture Radar (UAVSAR) operates at 1.25 GHz frequency which gives fully polarimetric SAR data. UAVSAR carry the radar instrument which is in a pod mounted to the fuselage of a Gulfstream III jet as shown in figure 35. The aircraft flies at an altitude of 12.5 km and maps a 20 km swath with incidence angles ranging from 25⁰ to 65⁰. Fully polarimetric Single Look Complex (SLC) images are available with range and azimuth pixels spacing of 1.66 m and 1 m respectively. The data sets are downloaded from <http://uavsar.jpl.nasa.gov/> the other attributes are Table 2.

Table 2: List of precision data files and radar parameters of SLC imagery

| Data type | Data files | | Rows | Columns |
|------------------------------|---|---------------------------|---------------------------|---------------------------|
| Data acquisition: 28/05/2019 | | | | |
| SLC | Rosamd_17012_19029_002_190528_L090HH_CX_01.sl | | 92253 | 9900 |
| | Rosamd_17012_19029_002_190528_L090HV_CX_01.sl | | | |
| | Rosamd_17012_19029_002_190528_L090VH_CX_01.sl | | | |
| | Rosamd_17012_19029_002_190528_L090VV_CX_01.sl | | | |
| | Site | Rosamond, California, USA | Data frequency | 1.2575 GHz (L band) |
| | Looking direction | Left | Acquisition mode | Quad pol (HH, HV, VH, VV) |
| | Byte order | Little Endian | Complex type | F-Complex |
| | Range Resolution | 1.8 m | Azimuth Resolution | 0.8 m |
| | Bore sight | 90 degree | | |

Table 3: List of precision data files and radar parameters of Multi look imagery

| Data type | Data files | Rows | Columns |
|-----------|------------|------|---------|
|-----------|------------|------|---------|

| Data acquisition: 28 th May 2019 | | | |
|---|--|---------------------------|------------------------|
| GRD | Rosamd_17012_19029_002_190528_L090HHHH_CX_01_ML 3X3.grd | 3192 | 2083 |
| | Rosamd_17012_19029_002_190528_L090HHHV_CX_01_ML 3X3.grd | | |
| | Rosamd_17012_19029_002_190528_L090HHVV_CX_01_ML 3X3.grd | | |
| | Rosamd_17012_19029_002_190528_L090HVHV_CX_01_ML 3X3.grd | | |
| | Rosamd_17012_19029_002_190528_L090HVVV_CX_01_ML 3X3.grd | | |
| | Rosamd_17012_19029_002_190528_L090VVVV_CX_01_ML 3X3.grd | | |
| Data frequency | 1.2575 GHz (L band) | Acquisition mode | Quad pol |
| Byte order | Little Endian | Bore sight | 90 degree |
| Range Resolution | -0.000166680 degrees | Azimuth Resolution | 0.000166680 degrees |

4.3 Gamma Naught stability analysis carried out for Amazon Rainforest and Boreal Forest- Canada.

Sentinel-1 data specifications

Sentinel-1 is equipped with a SAR sensor operating at C-band (5.405 GHz). The data acquired is level -1 GRD (Ground Range Detected). This product consists of focused SAR data that has been detected, multi-looked and projected to ground range using an Earth ellipsoid model. Ground range coordinates are the slant range coordinates projected onto ellipsoid of the Earth. Pixel values represent detected magnitude. Phase information is lost. (Hub, n.d.)

GRD products available in three resolutions, characterized by the acquisition mode and the level of multi looking applied. Full Resolution, High Resolution, Medium Resolution. Product resolutions by mode: Strip Map GRD, Interferometric Wide Swath GRD, Extra Wide Swath GRD.

Table 4: Details of Sentinel-1 data

| | |
|---------------------|------------------------|
| Satellite | Sentinel-1 |
| Product Type | Ground Resolution Data |

| | |
|-------------------------------------|---------------------------------|
| Sensor mode | Interferometric Wide swath (IW) |
| Acquisition mode | Dual Polarization |
| Radar Center Frequency (GHz) | 5.404999 |
| Radar Wavelength(m) | 0.055466 |
| Study Year | 2015, 2016,2017 |
| Spatial Resolution | 10* 10 m |

Table 5: Details of ALOS 2 PALSAR 2 data

| | |
|-------------------------------------|-------------------|
| Satellite | ALOS 2 |
| Product Type | HDR |
| Sensor mode | PALSAR 2 |
| Acquisition mode | Dual Polarization |
| Radar Center Frequency (GHz) | 1.2 |
| Study Year | 2015, 2016, 2017 |
| Spatial Resolution | 25m * 25m |

Software's: Open source software such as PolSARpro V.6.0, ENVI Classic V.5.4 and GammaMsys-2 (licensed software) software's were used in this study.

5 Methodology

5.1 Stability analysis for corner reflectors deployed in Surat Basin, Australia

To estimate RCS for each corner reflector and derive image quality parameters using IRF of the corner reflector, the following steps are used:

- As the SAR system is linear, for a point target like corner reflector, impulse response function was generated to determine the image quality parameters. The location of each corner reflector is identified based on peak intensity value of the target from the SAR image.
- To eliminate the influence of background noise present in the pixel containing corner reflector, location for the clutter background is selected near to the point target.

- Theoretical radar cross section (σ_0) of the point target is estimated by using equation 1 which is dependent on frequency of the SAR system and size of the corner reflector.

$$\sigma_0 = \frac{4\pi a^4}{3\lambda^2} \quad (1)$$

λ = radar wavelength (5.4 GHz)

a = inner leg length of triangular trihedral plate (1.5 m)

- Gamma software generate the impulse response functions for a given corner reflector by area integration method based on CR size, shape and theoretical RCS. This method minimizes the calibration error caused by the speckle and receiver noises (*Shimada 1996*).
- Calibration factor k is derived by calculating integrated power of a point target from interpolated background corrected intensity image with estimation of incidence angle at each corner reflector location.

$$k_i = \frac{\varepsilon_{pi}}{\sigma_{ref} \sin \theta_i} \quad (2)$$

where, k_i = calibration constant of the i^{th} corner reflector,

ε_{pi} = energy associated with the point-target,

σ_{ref} = theoretical radar cross section of the corner reflector,

θ_i = incidence angle of the i^{th} corner reflector.

- Signal to clutter ratio (SCR) is the ratio between point target energy corrected for clutter and average clutter energy per pixel. SCR is determined for each corner reflector and is considered when signal to clutter ratio is greater than 20 dB. The corresponding values are then used for further analysis of the SAR image.
- Image quality parameters like spatial resolution in range & azimuth direction, Peak Side Lobe Ratio (PSLR), Integrated Side Lobe Ratio (ISLR), Signal to clutter ratio are measured.
- Spatial resolution is derived from width of the main lobe at a power level, 3dB width from the peak of the impulse response function measured in both azimuth and range direction as shown in Figure 6. Azimuth resolution is estimated by using Equation 3 and Range resolution is estimated using Equation 4 (*Dadhich, et al. 2018*).

$$\text{Azimuth resolution } \rho_{az} = \frac{L}{2}; \quad (3)$$

Range resolution consist of slant range and ground range resolution:

$$\begin{aligned} \text{slant range resolution } \rho_{rs} &= \frac{c}{2B} \\ \text{ground range resolution } \rho_{rg} &= \frac{\rho_{rs}}{\sin\varphi} \end{aligned} \quad (4)$$

where,

L = antenna length in azimuth direction

c= speed of the light

B= chirp bandwidth

φ = local incidence angle

- PSLR is the power ratio of highest side lobe power to peak power in main lobe, which is power resolution between main lobe and side lobe of the IRF (P.V, et al. 2016), as shown in Figure 6 and the PSLR formulae is given by Equation 5.

$$\text{PSLR} = 20 \cdot \log_{10} \left(\frac{P_{\text{side-lobe}}}{P_{\text{main-lobe}}} \right) \quad (5)$$

- ISLR is the ratio of the integrated side-lobe energy to the integrated main-lobe energy, which describes the extent of energy spread around main lobe (P.V, et al. 2016), shown in Figure 6 and the ISLR formulae is given by Equation 6.

$$\text{ISLR} = 20 \cdot \log_{10} \left(\frac{\text{side lobe energy}}{\text{main lobe energy}} \right) \quad (6)$$

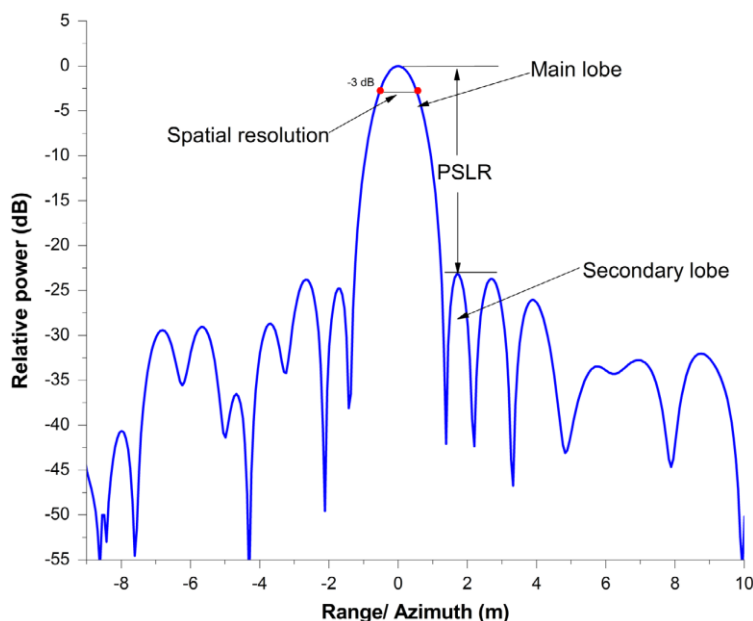


Figure 6: Impulse Response Function in range and azimuth direction © (Dadhich, et al. 2018)

5.2 Radiometric and polarimetric calibration of airborne UAVSAR L-band data.

The below mentioned methodology is followed to achieve the radiometric and polarimetric calibration of airborne UAVSAR sensor (L-band) in this work. Primarily the un-calibrated full pol. dataset is used to obtain the parameters mentioned in the steps below.

- Absolute calibration constant (A) was estimated using the methodology given in (Alexander, Bruce and Brian 2014) and (Shweta, et al. 2017).
- Co-pol. channel imbalance (f_i) parameter and co-pol. channel phase difference ($\phi_t + \phi_r$) are estimated at each corner reflector. Cross-pol channel imbalance (g) and cross-pol channel phase difference $\phi_t - \phi_r$ are derived from a sufficiently large homogenous featureless patch (distributed target) of the scene.
- Estimated values of A, f_i , g, $\phi_t + \phi_r$ and $\phi_t - \phi_r$ are used in the correction of the dataset to obtain radiometric and phase calibrated dataset. Since phase difference between polarized channels (HH and VV) is 1.5° and less than the specified value of 5° , it is assumed that the dataset is well radiometrically and phase calibrated.
- Polarimetric signatures are generated using the above corrected dataset, and these signatures should match the ideal signature of corner reflector.
- Cross talks (u, v, w, z) and channel imbalance (α , k) are estimated using the radiometric and phase corrected dataset. Quegan's algorithm (Quegan 1994) and Ainsworth algorithm (Ainsworth and Ferro-Famil 2006) are best calibration techniques which can be used to minimize the cross talks and channel imbalance. In this study, Quegan's algorithm was used to generate polarimetric distortion matrix (PDM).
- The above estimated u, v, w, z, α and k values are then used in the cross talk and channel imbalance correction, generating polarimetric calibrated dataset.
- Polarimetric signatures are generated using the above corrected dataset and should match the ideal signature of corner reflector.

Polarimetric Target Descriptions

Radar polarimetry is science of acquiring, processing and analysing the polarization state of an electromagnetic wave (Pottier, Lee and Famil 2007). The polarization information contained in the backscatter wave is highly related to the targets geometrical structure, orientation and

geographical properties such as humidity, roughness and soil conductivity. This characteristic information can be completely described by scattering matrix S or coherent matrix T or covariance matrix C.

Scattering Matrix (S)

SAR system is a high-resolution radar capable of measuring the complex form of reflectivity of the target. A SAR image represents the scattering matrix element S_{pq} in complex form or radar cross section σ_{pq} in terms of intensity for the receive (q) and transmit (p) waves of the radar (Freeman 1995). The horizontal and vertical components helps to describe electromagnetic wave (E) and given by **Error! Reference source not found.7**:

$$\begin{pmatrix} E_h^s \\ E_v^s \end{pmatrix} = \frac{e^{jk_0R}}{R} \begin{pmatrix} S_{hh} & S_{hv} \\ S_{vh} & S_{vv} \end{pmatrix} \begin{pmatrix} E_h^i \\ E_v^i \end{pmatrix} \quad (7)$$

Where,

i = electric field vector of the incident wave.

s = electric field vector of the scattered wave.

k_0 = wavenumber of the illuminating wave.

R = radar distance between target and radar antenna.

The four elements of the scattering matrix are complex and these elements are measured from the magnitudes and phases measured by the four channels of a polarimetric radar. These scattering properties vary with frequency and look angle of the radar. For linear polarization the scattering matrix (S) is measured using two polarized antennas and as defined by **Error! Reference source not found.8**, which is a 2x2 matrix:

$$[S] = \begin{bmatrix} S_{HH} & S_{HV} \\ S_{VH} & S_{VV} \end{bmatrix} \quad (8)$$

The intensity in the cross-polarization terms is much lesser than the co-pol terms, which is influenced by background and instrument noise. In case of mono-static configuration, scattering matrix is assumed symmetrical, reciprocity theorem $S_{HV} = S_{VH}$ is applied, and has three independent elements in a full polarimetric system. In case of bi-static configuration, scattering matrix is not symmetric. Various polarimetric features can be derived from the scattering matrix

or vector. The scattering matrix is transformed into scattering vector on Pauli basis and used for decomposition techniques and is given by **Error! Reference source not found.9**.

$$\text{Scattering vector, } V = \frac{1}{\sqrt{2}} \begin{bmatrix} S_{HH} + S_{VV} \\ S_{HH} - S_{VV} \\ 2S_{HV} \end{bmatrix} \quad (9)$$

Covariance (C) and Coherency (T) Matrices

The covariance and coherence matrices are derived from scattering matrix. It explains the relation between received signals in the channels of polarimetric radar and describes the scattering properties of the target. In mono static condition, reciprocity symmetry is assumed and 3x3 matrices were obtained such as Equation 112 and **Error! Reference source not found.**. In case bi-static, symmetry cannot be assumed, and 4x4 matrices were obtained such as **Error! Reference source not found.13** and **Error! Reference source not found.15**.

A covariance or coherence matrix is a second order statistics of scattering matrix elements and it is Hermitian semi definite positive matrix. These matrices are constructed from a unitary target vector obtained from the projection of a scattering matrix onto a reduced and modified Pauli spin matrix set.

Covariance Matrix

System vectors such as 10 and **Error! Reference source not found.** are constructed from the backscattering matrix [S], that helps to extract information of the target. The matrix is based on lexicographic combinations of scattering matrix elements. The factor $\sqrt{2}$ helps to keep the norm of the target vector invariant, which is equal to the total power scattered by the target. (*Pottier, Lee and Famil 2007*)

$$k_{3L} = [S_{11} \quad S_{12}\sqrt{2} \quad S_{22}] \quad (10)$$

$$k_{4L} = [S_{11} \quad S_{12}S_{21}S_{22}] \quad (11)$$

$$[C_3] = k_{3L}k_{3L}^\dagger = \begin{bmatrix} |S_{hh}|^2 & \sqrt{2}S_{hh}S_{hh}^* & S_{hh}S_{vv}^* \\ \sqrt{2}S_{hv}S_{hv}^* & 2|S_{hv}|^2 & \sqrt{2}S_{hv}S_{vv}^* \\ S_{vv}S_{hh}^* & \sqrt{2}S_{vv}S_{hv}^* & |S_{vv}|^2 \end{bmatrix} \quad (12)$$

Equation 1. Covariance 3x3 matrix for mono-static case

Where * represents the conjugate and † represents the conjugate transpose.

$$[C_4] = k_{4L} k_{4L}^\dagger = \begin{bmatrix} \langle |S_{HH}|^2 \rangle & \langle S_{HH} S_{HV}^* \rangle & \langle S_{HH} S_{VH}^* \rangle & \langle S_{HH} S_{VV}^* \rangle \\ \langle S_{HV} S_{HH}^* \rangle & \langle |S_{HV}|^2 \rangle & \langle S_{HV} S_{VH}^* \rangle & \langle S_{HV} S_{VV}^* \rangle \\ \langle S_{VH} S_{HH}^* \rangle & \langle S_{VH} S_{HV}^* \rangle & \langle |S_{VH}|^2 \rangle & \langle S_{VH} S_{VV}^* \rangle \\ \langle S_{VV} S_{HH}^* \rangle & \langle S_{VV} S_{HV}^* \rangle & \langle S_{VV} S_{VH}^* \rangle & \langle |S_{VV}|^2 \rangle \end{bmatrix} \quad (13)$$

Coherency Matrix

Coherency matrix is obtained from scattering matrix in Pauli basis form and same as the covariance matrix.

$$[T_3] = k_{3L} k_{3L}^\dagger = \frac{1}{2} \begin{bmatrix} \langle |S_{HH} + S_{VV}|^2 \rangle & \langle (S_{HH} + S_{VV})(S_{HH} - S_{VV})^* \rangle & 2 \langle (S_{HH} + S_{VV}) S_{HV}^* \rangle \\ \langle (S_{HH} - S_{VV})(S_{HH} + S_{VV})^* \rangle & \langle |S_{HH} - S_{VV}|^2 \rangle & 2 \langle (S_{HH} - S_{VV}) S_{HV}^* \rangle \\ 2 \langle S_{HV} (S_{HH} + S_{VV})^* \rangle & 2 \langle S_{HV} (S_{HH} - S_{VV})^* \rangle & 4 \langle |S_{HV}|^2 \rangle \end{bmatrix} \quad (14)$$

$$[T_4] = k_{4L} k_{4L}^\dagger = \begin{bmatrix} T_{11} & T_{12} & T_{13} & T_{14} \\ T_{12}^* & T_{22} & T_{23} & T_{24} \\ T_{13}^* & T_{23}^* & T_{33} & T_{34} \\ T_{14}^* & T_{24}^* & T_{34}^* & T_{44} \end{bmatrix} \quad (15)$$

The Eigen values of the above matrices are positive, real semi definite Hermitian (*Pottier, Lee and Famil 2007*). Span of the data is defined as the sum of the diagonal elements is proportional to the total received power from the polarimetric channels. The first diagonal elements of the matrices give the single bounce scattering information, the second diagonal elements give double bounce scattering information and third diagonal elements gives information about volume scattering.

Radiometric and Phase Calibration

While applying the radiometric correction, two types of error occurs (a) SAR cross track antenna pattern error due to wrong measurement in the elevation angle between the radar and pixel location and (b) error in the slant range to ground range project of the pixel area due to misreading in the local incidence angle of that particular pixel (*Freeman 1995*). The correction for the above two errors are applied to the dataset and are distributed by the JPL/NASA. Radiometric correction

is to convert image pixel values into normalized radar cross section (σ_{cr}) from Equation 13 which is an important goal in calibrating SAR images and estimated. Phase calibration is to minimize the phase bias present in both co-pol and cross-pol channels. Neglecting the cross talks and channel imbalances, radiometric and phase calibration is applied to the datasets as per Equation 16.

$$S' = A \begin{bmatrix} s_{vv}f^2 e^{i(\phi_{t,v}+\phi_{r,v})} & s_{vh}(\frac{f}{g})e^{i(\phi_{t,h}+\phi_{r,v})} \\ s_{hv}fg e^{i(\phi_{t,v}+\phi_{r,h})} & s_{hh}e^{i(\phi_{t,h}+\phi_{r,h})} \end{bmatrix} \quad (16)$$

Where, S' = radiometric and phase calibrated scattering matrix from transmitted polarization 't' and received polarization 'r'.

$S_{vv}, S_{hh}, S_{vh}, S_{hv}$ = observed scattering matrix

A = absolute calibration factor

f = co-pol channel imbalance parameter

g = cross-pol channel imbalance parameter

$\phi_{x,j}$ = phase error in-current when transmitting or receiving polarization 'j'

After removal of the arbitrary phase, Equation 16 reduces to Equation 17

$$S' = A \begin{bmatrix} s_{vv}f^2 e^{i(\phi_t+\phi_r)} & s_{vh}(\frac{f}{g})e^{i(\phi_r)} \\ s_{hv}fg e^{i(\phi_t)} & s_{hh} \end{bmatrix} \quad (17)$$

Where, $\phi_t = \phi_{t,v} - \phi_{t,h}$; $\phi_r = \phi_{r,v} - \phi_{r,h}$

Estimation of Absolute Calibration Parameter (A):

Absolute calibration parameter (A) is the calibration factor relating the SAR image intensity and radar cross section of the target (*Masanobu, et al. 2013*). It is obtained using Equation 18 (*Alexander, Bruce and Brian 2014*) and Equation 19 (*Ronald, Elaine and Alex Fore 2015*).

$$10 \log_{10} \left[\frac{\sigma_{cr}}{(s_{hh}s_{hh}^*)} \right] = -10 \log_{10}(A^2) \quad (18)$$

$$\sigma_{cr} = 4\pi l^4 / \lambda^2 [\Omega(\theta_{cr}, \phi_{cr}) - 2/\Omega(\theta_{cr}, \phi_{cr})]^2 \quad (19)$$

Where, σ_{cr} = RCS of a triangular trihedral corner reflector

$\Omega(\theta_{cr}, \phi_{cr}) = \cos\theta_{cr} + (\sin\phi_{cr} + \cos\phi_{cr}) \sin\theta_{cr}$

θ_{cr} : Incidence angle relative to the triangular trihedral corner reflector

ϕ_{cr} : Azimuth angle relative to one of the vertical side of the corner reflector (max. response of the corner reflector is at 45 deg.)

λ : Wavelength of the radar signal

L = length of inner side of the triangular corner reflector (2.4384 meters)

Estimation of co-pol channel imbalance (f) and phase difference phi_t

Co-pol channel imbalance parameters f and $\phi_t + \phi_r$ are estimated using equation 14 for each corner reflectors and mean value of them is considered as effective value. Phase anomaly $\phi_t + \phi_r$ between HH and VV polarizations are estimated using equation 15

$$f = \left[\frac{s_{vv}s_{vv}^*}{s_{hh}s_{hh}^*} \right]^{1/4} \quad (20)$$

$$\phi_s = \mathbf{arg}(s_{vv}s_{hh}^*) \quad (21)$$

Where, $\phi_s = \phi_t + \phi_r$

Estimation of cross-pol channel imbalance (g) and phase difference phi_r

Cross-pol channel imbalance parameters g is estimated using homogenous distributed target of 700 x 700 pixels from the image as per equation 22 and phase anomaly $\phi_t - \phi_r$ between HV and VH polarizations are estimated using equation 23.

$$g = \left[\frac{\langle s_{hv}s_{hv}^* \rangle}{\langle s_{vh}s_{vh}^* \rangle} \right]^{1/4} \quad (22)$$

$$\phi_d = \mathbf{arg}(s_{hv}s_{vh}^*) \quad (23)$$

Where, $\phi_d = \phi_t - \phi_r$

Phase anomaly at transmission ϕ_t and reception ϕ_r is estimated using equation 21 and equation 23

$$\phi_t = \frac{\phi_s + \phi_d}{2}$$

$$\phi_r = \frac{\phi_s - \phi_d}{2}$$

Polarimetric Calibration

Polarimetric SAR data calibration is an important process to ensure accurate extraction of the geophysical properties of the target. Calibration is required to understand polarimetric signatures of the target and also to compare observations between scenes and theory (Quegan 1994). To transform data into quantitative parameter such as biophysical or geophysical properties, it is necessary to assure that dataset is not contaminated. The distortion matrices which is estimated express the polarimetric transformation between transmission and reception using channel imbalance and cross talks (Chen, Tao and Xueliang 2011). In Airborne SAR system, the cross talk is range dependent and cannot be neglected which becomes an important step for the polarimetric calibration procedure. Well established Quegan and Ainsworth cross talk correction models are available and detailed description of these models are defined in the following sections.

Distortion Models-Quegan's Algorithm

The calibration algorithm proposed by Quegan is more general approach and widely used as standards for cross talk calibration of the polarimetric data. This unified approach has been applied to the scattering matrix and it relies on the scene dominated targets. The algorithm requires unsymmetrical data and uses quantities derived from the covariance matrix. It permits ready interpretation of the terms in the calibration procedure without system reciprocity assumption. The following are the assumptions are used to perform cross talk calibration. The acquired dataset is fully polarimetric and available in the form of the scattering matrix.

- 1) The observed scattering matrix can be modeled as a linear system.
- 2) Scattering reciprocity is satisfied unless the target is physically altered $S_{ij} = S_{ji}$.
- 3) In case of distributed targets, cross polarized channels are not correlated $\langle S_{ij} S_{ij}^* \rangle = 0$.
- 4) The off diagonal terms of the matrices [R] and [T] are small compared to the diagonal terms.

The systems effects are modeled by two stage linear process so that observed data matrix S' can be written as

$$S' = RST + N$$

Where, R and T are phase and amplitude distortions introduce on receive and transmit and N is system noise. The above expression can be rewritten as

$$[S'] = [M][S] + [N]$$

Where,

[S'] = observed scattering matrix in the form of $(S'_{HH}, S'_{HV}, S'_{VH}, S'_{VV})^T$

[S] = True scattering matrix in the form of $(S_{HH}, S_{VH}, S_{VV})^T$

[M] = Distortion matrix of dimension (4x3)

[N] = System noise matrix $(N_{HH}, N_{HV}, N_{VH}, N_{VV})^T$

Due to condition (3) and (4), the region being calibrated is dominated by targets for, which the vector S of the covariance matrix $\langle C_s \rangle$ gets reduced to (24)

$$\langle C_s \rangle = \begin{bmatrix} \sigma_{HH} & 0 & \rho \\ 0 & \sigma_{VH} & 0 \\ \rho^* & 0 & \sigma_{VV} \end{bmatrix} \quad (24)$$

Where,

$$\sigma_{ij} = \langle S_{ij} S_{ij}^* \rangle; \quad \rho = \langle S_{HH} S_{VV}^* \rangle = \langle S_{VV} S_{HH}^* \rangle^*$$

Now, observed covariance matrix (C) of [S'] is given by (25) ignoring system noise

$$C = M C_s M^\dagger \quad (25)$$

Where M^\dagger is the conjugate transpose of M

Distortion matrix can be expressed as

$$M = Y \begin{pmatrix} \alpha & v + \alpha w & vw \\ \alpha u & \alpha & v \\ \alpha z & 1 & w \\ \alpha uz & u + \alpha z & 1 \end{pmatrix} \begin{pmatrix} k^2 & 0 & 0 \\ 0 & k & 0 \\ 0 & 0 & 1 \end{pmatrix} \quad (26)$$

This distortion matrix consists six unknowns u, v, w, z are the complex crosstalk parameters and α, k are the complex channel imbalance parameters. u, v, w, z can be obtained from equation (27)

$$\left. \begin{aligned} u &= (C_{44} C_{21} - C_{41} C_{24}) / \Delta \\ v &= (C_{11} C_{24} - C_{21} C_{14}) / \Delta \\ z &= (C_{44} C_{31} - C_{41} C_{34}) / \Delta \\ w &= (C_{11} C_{34} - C_{31} C_{14}) / \Delta \\ \Delta &= C_{11} C_{44} - |C_{14}|^2 \end{aligned} \right\} \quad (27)$$

The term α can be derived as shown in equation (28), assuming the random noises in cross polarized channels are equal, i.e. $N_{VH} = N_{HV}$

$$\alpha = \frac{|\alpha_1 \alpha_2| - 1 + \sqrt{(|\alpha_1 \alpha_2| - 1)^2 + 4|\alpha_2|^2}}{2|\alpha_2|} \frac{\alpha_1}{|\alpha_1|}$$

$$\alpha_1 = \frac{c_{22} - u c_{12} - v c_{42}}{X}$$

$$\alpha_2 = \frac{X^*}{C_{33} - z^* C_{31} - w^* C_{34}}$$

$$X = C_{32} - z C_{12} - w C_{42}$$

$$k = \frac{1}{\sqrt{\alpha}}$$
(28)

Polarimetric signatures

Polarization signature is defined as a plot of the backscattered power received from the target (corner reflector) as a function of the polarization of the incident wave and backscattered electromagnetic wave. It helps in visualization and analysis of backscatter behaviour of a target (Polarimetric Analysis of Airborne DLR-ESAR for Vegetation Characterization 2012). The polarization of a wave is described by four independent variables:

- (a) Ellipticity of the incident wave
- (b) Orientation of the incident wave
- (c) Ellipticity of the backscattered wave
- (d) Orientation of the backscattered wave.

Only two variables either ellipticity and orientation of the incident wave/ backscattered wave are used at a time to portray the co-pol and cross-pol signatures.

In co-pol case, the polarization of the scattered wave is same as polarization of the incident wave, while for the case of cross-polarization, the polarization of the scattered wave is orthogonal to the polarization of the incident wave. Co-polarization signature of “ridge shape” and Cross-polarization signature of “valley shape” are generated due to change in ellipticity sign of the polarimetric data. For linear polarization, the co-pol response is unity and cross-pol response is zero. These signatures help in identifying different surface scatterer.

The polarimetric signature can be generated using electromagnetic wave synthesis. The synthesised scattering matrix ($[S_{syn}]$) can be generated from the actual scattering matrix ($[S]$) with respect to varying ellipticity angle (χ) and orientation angle (ψ).

$$S_{syn} = [R_{\psi}][S][R_{\chi}]$$

Where,

$$[R_{\psi}] = \begin{bmatrix} \cos\psi & -\sin\psi \\ \sin\psi & \cos\psi \end{bmatrix}; [R_{\chi}] = \begin{bmatrix} \cos\chi & -j \sin\chi \\ -j \sin\chi & \cos\chi \end{bmatrix}$$

5.3 Gamma Naught stability analysis carried out for Amazon Rainforest and Boreal Forest- Canada.

Stability evaluation of the gamma naught values for Amazon Rain Forest and Boreal forest: - Rain forest is a uniform, distributed and reference target for relative (range and azimuth antenna pattern determination) and absolute calibration target. Reflectivity estimates (sigma or gamma naught) are calculated which helps to understand the stability over Amazon rainforest. To calculate gamma naught values, the below mention equation (29 & 30) is used.

$$\sigma^{\circ} = 10 \log_{10}\langle DN^2 \rangle + CF \quad (29)$$

$$\gamma^{\circ} = \sigma^{\circ} / \cos \varphi \quad (30)$$

DN = digital number of the intensity image.

CF = calibration factor, -83.0 dB

The following procedure is used to calculate gamma naught values for both C and L band data: common area shared by both C and L band data was selected. The coordinates for Amazon rainforest are **49°58'34'' N, 84°00'00'' W; 50°59'54'' N, 84°59'57'' W** and Boreal forest are **49°58'34'' N, 84°00'00'' W; 50°59'54'' N, 84°59'57'' W**. Pre-processing of data is required to apply gamma naught formula. Calibration is the important step providing the pixel values that are directly related to the radar backscatter of the scene. Though un-calibrated SAR imagery is sufficient for qualitative use, calibrated SAR images are essential for quantitative use of SAR data. For performing the calibration step, following equation is used:

$$\text{Value (i)} = \frac{DN^2}{Ai^2}$$

where, value (i) = original DN

$$A_i = \text{dn}(i), \text{Gamma Naught}$$

For masking out the water pixels, two methods can be utilized:

- Based on the intensity values: In this method, histogram is generated for the intensity image and from the histogram, minimum value was used to select water pixels. Either sigma naught or gamma naught may be used to select water pixel. The condition applied is “ $IF \text{Sigma_VV} < 1.25E^{-2} \text{ then } 1 \text{ else } 0$ ”. This condition selects the water pixels.
- Based on sample water pixels’ histogram: In this method, samples of water pixels are selected and histogram is generated. The threshold values observed were pixels, which lie between -27 dB to -12 dB.

In this study, water pixels were masked out by using histogram method. The steps explained above is shown in Figure7. Figure 8 shows water pixels and wetland pixels masked. The intermediate layer contains only forest pixels i.e., without water, which is used to calculate gamma naught values. The calculated gamma naught values are in linear scale which is converted to decibel scale for further observations.

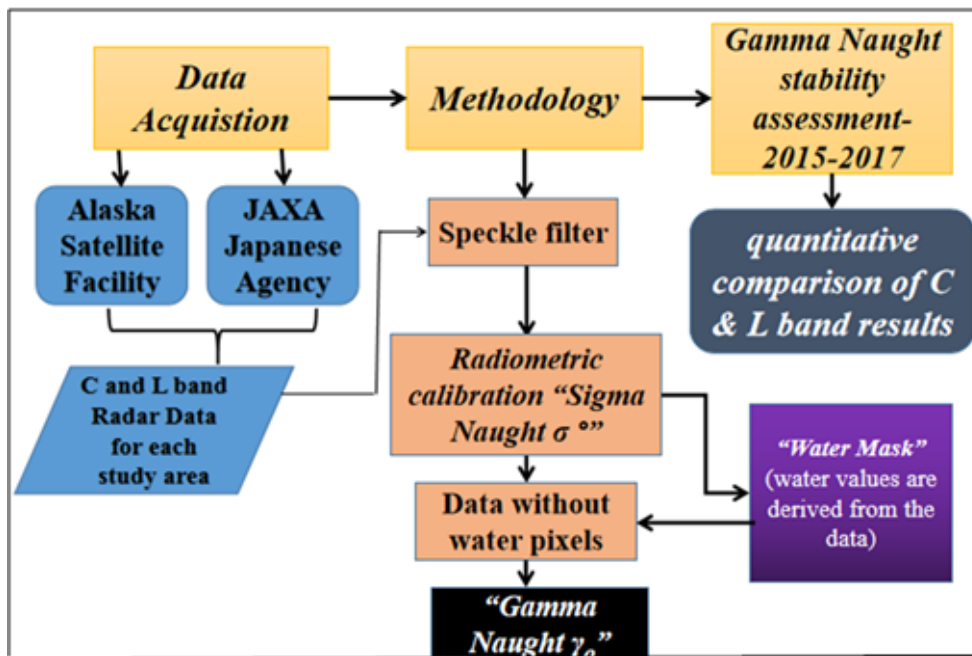
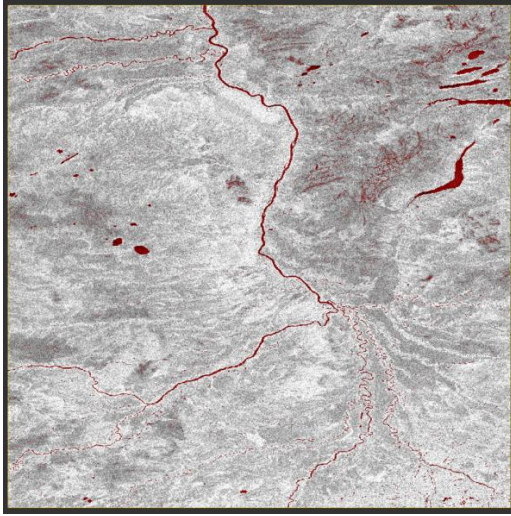


Figure 7: Flow-chart showing methodology

Showing water pixels



Showing water and wetland pixels

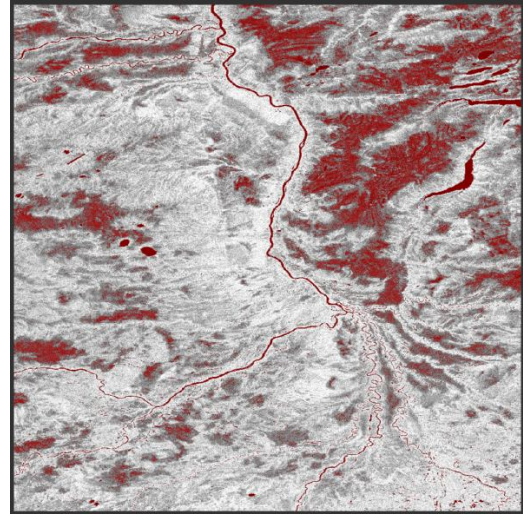


Figure 8: Left image shows the selection of water pixels based on water threshold and right image show the selection of wet land soil and water pixels based on intensity values.

6 Results & Discussion

6.1 Stability analysis for corner reflectors deployed in Surat Basin, Australia

Estimation of Signal to Clutter ratio (SCR) and RCS

The sentinel-1 c-band data of 25th July 19, 06th August 19 and 18th August 19 are used for estimation of RCS, calibration constant, PSLR, ISLR, azimuth and range resolutions.

Signal to Clutter ratio (SCR)

It is defined as the ratio between peak power in the target impulse response to the mean background clutter power. The background targets surrounding corner reflector has their own backscatter which influence the impulse response of the corner reflector. The unwanted background noise and background scattering from the other objects is termed as clutter. Table 6 contains pixel values of the clutter used for the IRF analysis. This clutter and noisy environment should be considered while estimating the impulse response of the corner reflector, to obtain backscattered energy of the corner reflector without clutter energy from other objects. SCR can be calculated using the formulae given by Equation 31 and fig 9 shows the signal to clutter ratio derived for each corner reflector.

$$SCR = \frac{\sigma_p}{\sigma_o A_{res}} \quad (31)$$

where,

σ_p = backscattered energy of the corner reflector,

$\sigma_o A_{res}$ = mean backscattered energy of the clutter.

Table 6: Details of clutter used for RCS estimation

| Clutter_ID | Sample | Lines | Clutter_ID | Sample | Lines |
|------------|--------|-------|------------|--------|-------|
| C1 | 18953 | 530 | C6 | 8761 | 4538 |
| C2 | 18823 | 1824 | C7 | 11961 | 7367 |
| C3 | 12462 | 1057 | C8 | 3459 | 3139 |
| C4 | 8784 | 1765 | C9 | 3484 | 1247 |
| C5 | 7744 | 2329 | | | |

Table 7 contains the pixel values of each corner reflector location, derived from SLC HH pol. data for the considered study period (25th July 19, 06th & 18th August 19) and are used for RCS estimation. The signal to clutter ratio for each corner reflector and RCS differences were estimated and given in Table 8 and Table 9. It is observed that difference between estimated RCS and theoretical RCS to be less than 1 dB (Figure 10). The mean RCS was found to be 37.84 ± 0.334 dB which is maintained for each CR except CR40. For CR40 abrupt change in incidence angle and signal to clutter ratio was observed (Figures 11 & 9). The high RCS difference at CR40 is due to high impulse response whose RCS for the CR is 40 dBm² and is used for ASAR sensor (5.3 GHz) calibration (Thankappan, Williams and Dawson 2011). The temporal variation in signal to clutter ratio are found to be greater than the specified value of 20 dB. Higher SCR value was noticed for CR40 whose estimated RCS value is greater than other CR RCS values, which also corresponds to brightness of CR of 45 dBm² at c-band. The mean SCR was found to be 35.55 ± 1.94 dB.

**ASAR sensor operates at 5.3 GHz frequency. The incidence angle of this ASAR is around 15-45 degrees with 5 to 8.4 meter azimuth resolution and 9.5 to 4.8 meter resolution for IMS and APS mode respectively (Thankappan, Williams and Dawson 2011).

Table 7: Corner reflector locations in SLC image for diff. dates

| CR_ID | Sample | Lines | Sample | Lines | Sample | Lines |
|-------|----------------------------|-------|------------------------------|-------|------------------------------|-------|
| | 25 th July 2019 | | 06 th August 2019 | | 18 th August 2019 | |
| CR19 | 18985 | 486 | 18987 | 486 | 18995 | 484 |
| CR27 | 18835 | 1850 | 18837 | 1849 | 18844 | 1847 |
| CR30 | 12440 | 1101 | 12443 | 1101 | 12449 | 1098 |
| CR36 | 8770 | 1812 | 8772 | 1812 | 8779 | 1810 |
| CR37 | 7784 | 2317 | 7786 | 2316 | 7793 | 2314 |
| CR38 | 8795 | 4545 | 8797 | 4545 | 8803 | 4541 |
| CR40 | 12020 | 7356 | 12022 | 7356 | 12028 | 7353 |
| CR41 | 3500 | 3153 | 3502 | 3150 | 3508 | 3149 |
| CR42 | 3524 | 1264 | 3527 | 1263 | 3532 | 1261 |

Table 8: Estimation of SCR for each CR

| CR_ID | Clutter ID | Incidence angle (deg.) | Signal to Clutter ratio (in dB) | | |
|-------|------------|------------------------|---------------------------------|------------------------------|------------------------------|
| | | | 25 th July 2019 | 06 th August 2019 | 18 th August 2019 |
| CR19 | C1 | 35.716 | 34.420 | 34.438 | 36.103 |
| CR27 | C2 | 35.678 | 37.722 | 36.608 | 36.701 |
| CR30 | C3 | 33.983 | 31.862 | 32.034 | 30.577 |
| CR36 | C4 | 32.950 | 36.993 | 36.261 | 35.008 |
| CR37 | C5 | 32.663 | 36.105 | 38.663 | 37.727 |
| CR38 | C6 | 32.957 | 36.919 | 35.949 | 35.076 |
| CR40 | C7 | 33.867 | 42.140 | 40.679 | 41.400 |
| CR41 | C8 | 31.375 | 35.467 | 34.836 | 34.106 |
| CR42 | C9 | 31.383 | 36.711 | 36.833 | 36.195 |

Table 9: Estimation of RCS and its difference

| CR_ID | Clutter ID | Incidence angle (deg.) | Estimated RCS (dB) | Theoretical RCS (dB) | Estimated RCS (dB) | Theoretical RCS (dB) | Estimated RCS (dB) | Theoretical RCS (dB) |
|-------|------------|------------------------|----------------------------|----------------------|------------------------------|----------------------|------------------------------|----------------------|
| | | | 25 th July 2019 | | 06 th August 2019 | | 18 th August 2019 | |
| CR19 | C1 | 35.716 | 38.168 | 0.210 | 38.188 | 0.190 | 38.182 | 0.196 |
| CR27 | C2 | 35.678 | 37.663 | 0.715 | 37.834 | 0.544 | 37.695 | 0.683 |

| | | | | | | | | |
|------|----|--------|--------|--------|--------|--------|--------|--------|
| CR30 | C3 | 33.983 | 37.270 | 1.108 | 37.432 | 0.946 | 37.179 | 1.199 |
| CR36 | C4 | 32.950 | 38.399 | -0.021 | 38.465 | -0.087 | 38.241 | 0.137 |
| CR37 | C5 | 32.663 | 37.601 | 0.777 | 37.982 | 0.396 | 37.731 | 0.647 |
| CR38 | C6 | 32.957 | 37.693 | 0.685 | 37.844 | 0.534 | 37.621 | 0.757 |
| CR40 | C7 | 33.867 | 45.039 | -6.661 | 44.861 | -6.483 | 45.149 | -6.771 |
| CR41 | C8 | 31.375 | 38.127 | 0.251 | 37.978 | 0.400 | 37.879 | 0.499 |
| CR42 | C9 | 31.383 | 37.608 | 0.770 | 37.862 | 0.516 | 37.596 | 0.782 |

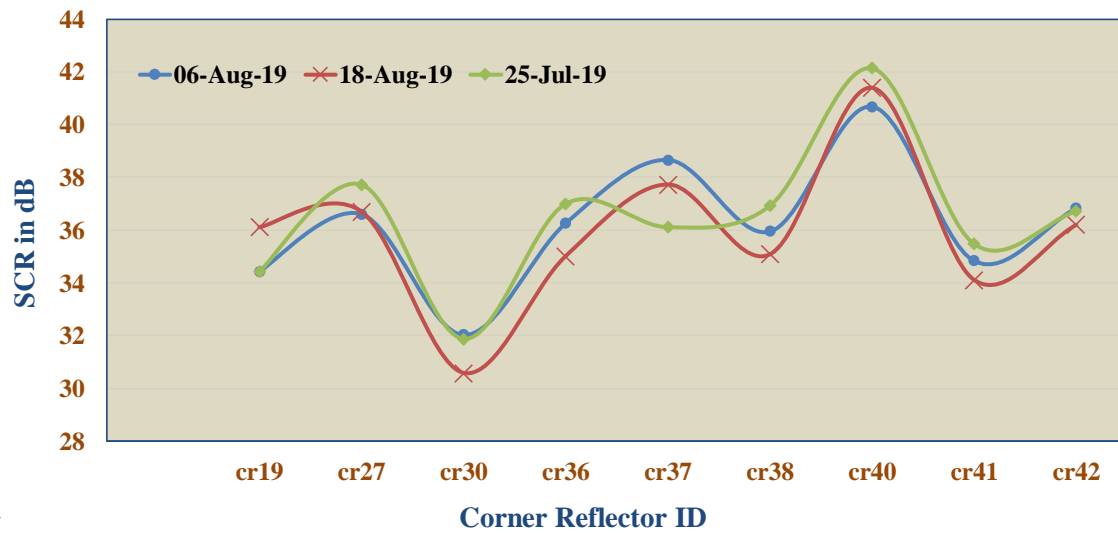


Figure 9: SCR of each CR estimated using SLC HH pol data

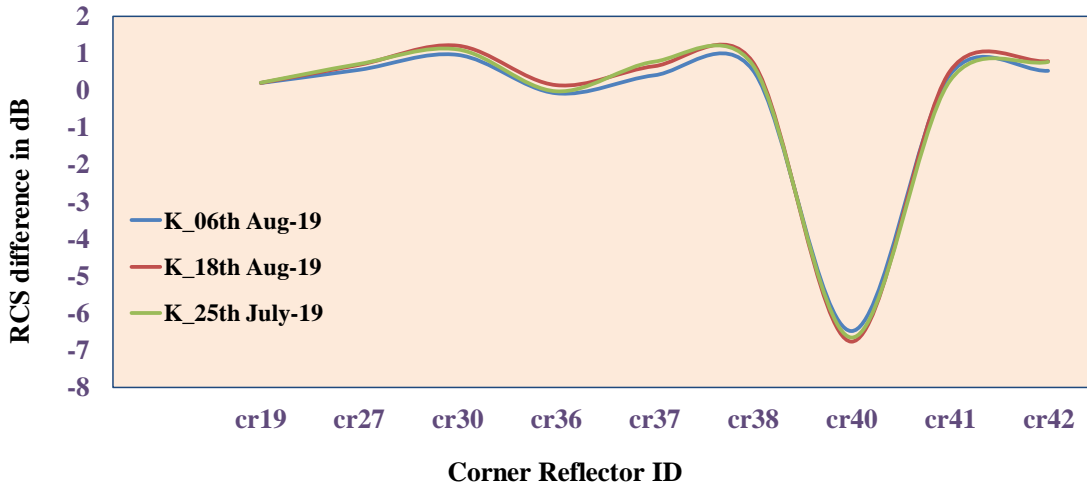


Figure 10: Difference between theoretical RCS and estimated RCS for HH pol.

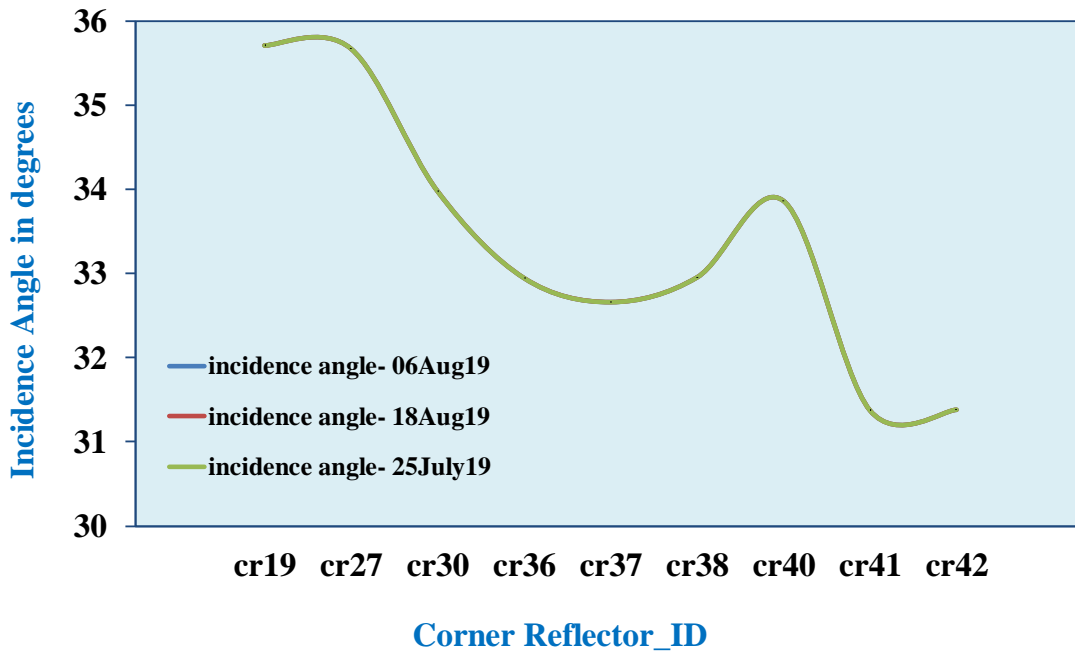


Figure 11: Incidence angle of each CR obtained from SLC HH pol data.

Impulse Response Functions of each CR's identified from SLC - HH pol. Data:

Impulse Response Function (IRF) is the radar response from the corner reflector with negligible thermal noise and background reflectivity. Impulse response functions are generated for each corner reflector for all the SAR images acquired. IRF are generated from GAMMA software based on integral method. Target window size of 16*16 and clutter window size of 8*8 are used to generate IRF. The following figures show two dimensional IRF of each corner reflector for the

considered time period which is a sin function of main lobe and many secondary lobes. To estimate spatial resolution, ISLR, PSLR of a corner reflector, the IRF is measured in both azimuth and range direction.

Spatial resolution: It is defined as between two objects on the ground, when the targets appear clear and distinct. It is derived from width of the main lobe at a power level, 3dB width from the peak of the impulse response function (Figure 6), measured in both azimuth and range direction as detailed in Table10. The ideal spatial resolution of a SAR system is given in the product file and is compared with the estimated value obtained from impulse response function of a target. The azimuth and range resolution can be obtained by using the below Equation (3) and (4). 2.33 meters and 14.06 meters are the specified range and azimuth resolutions respectively. Difference between specified resolution and estimated resolution for azimuth and range resolution is determined as shown in Figure 21. The Figures 13 – 20 show response of CR's used in this study and their impulse response functions.

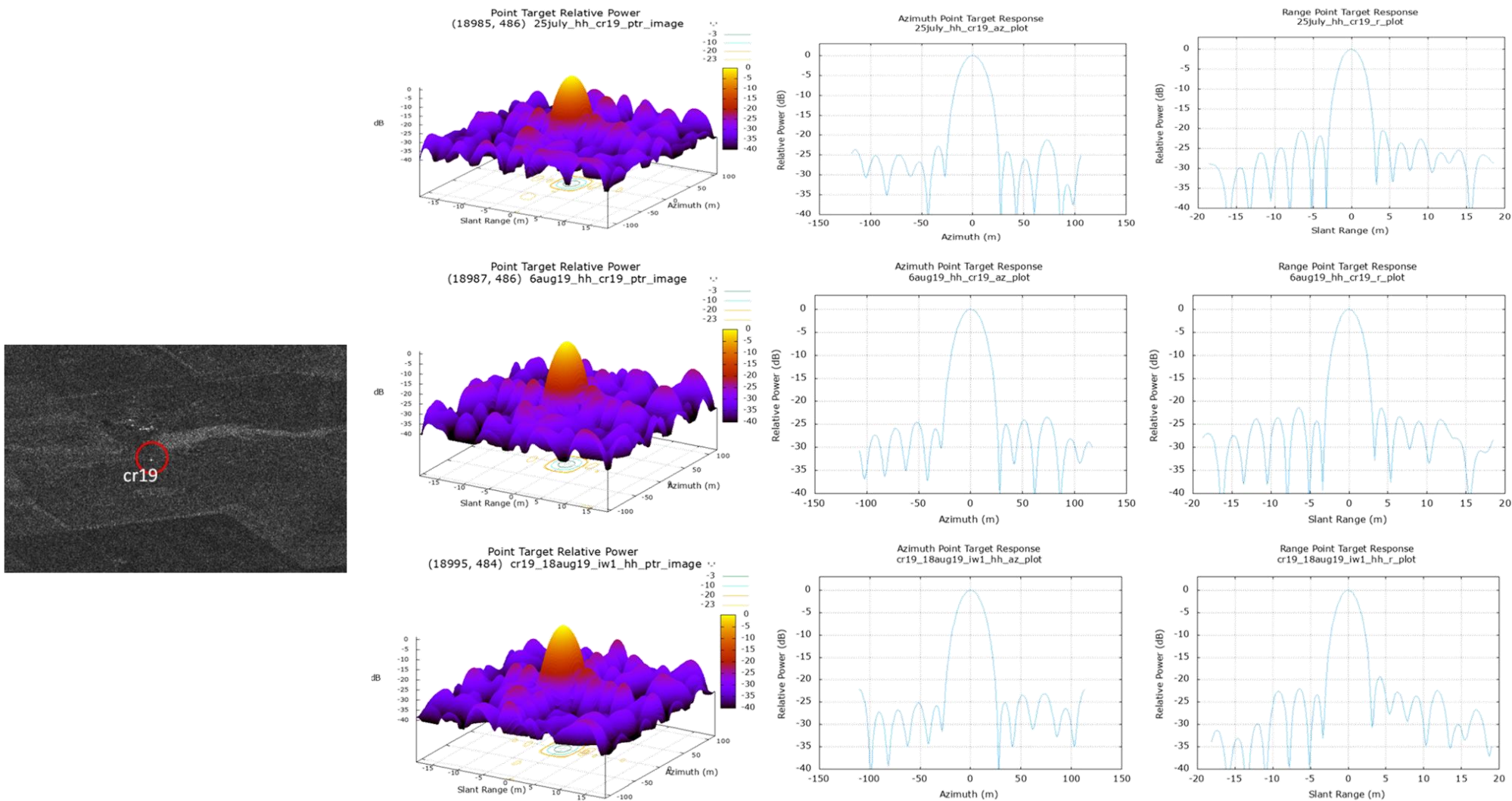


Figure 12: IRF for CR19 on 25th July, 06th Aug, 18th August 2019 using SLC HH polarization data.

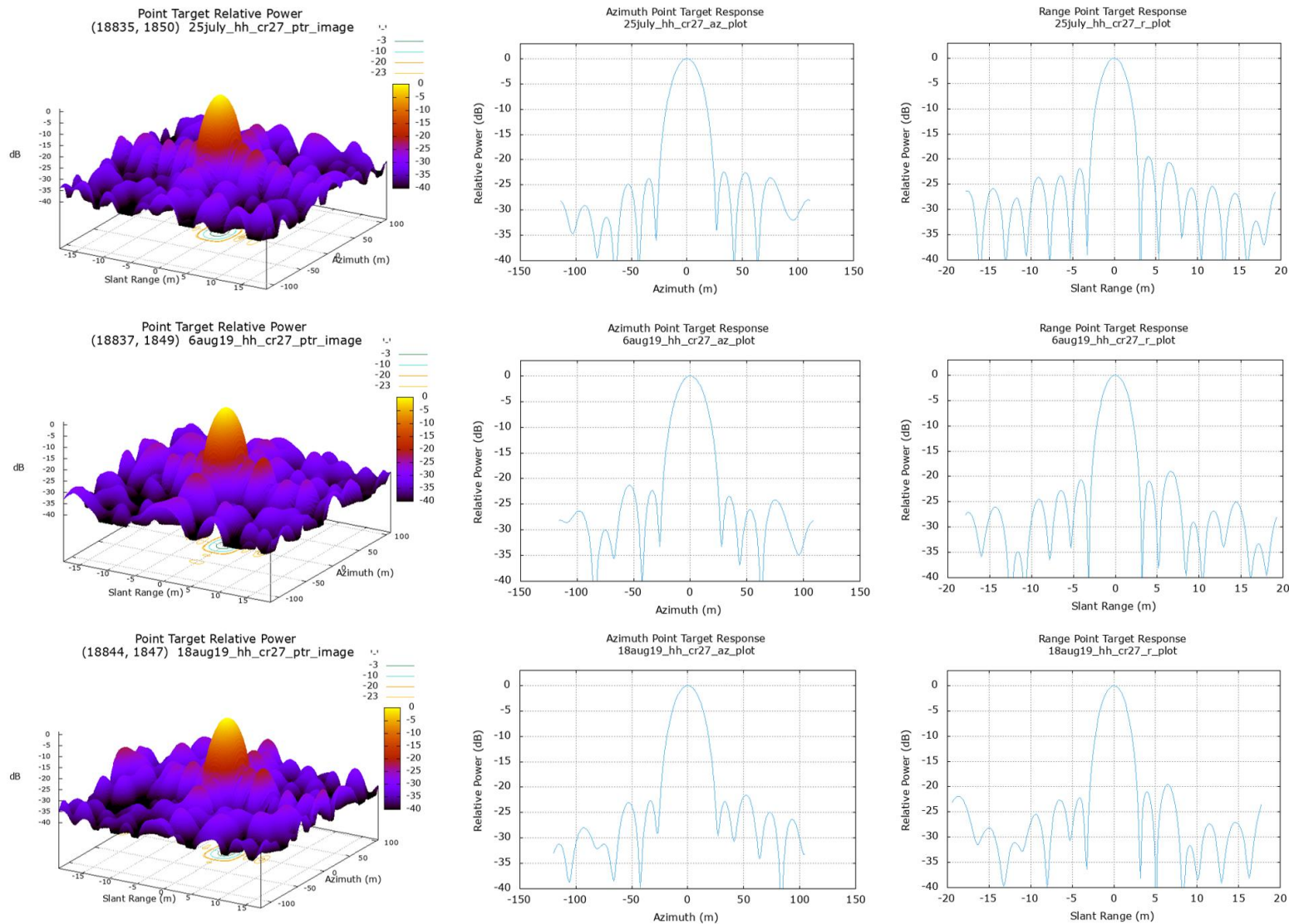
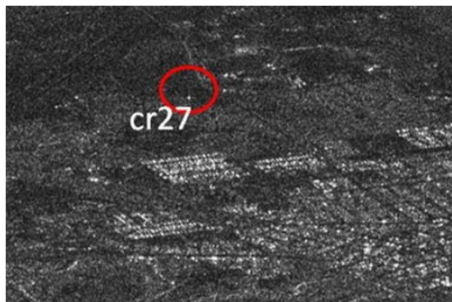


Figure 13: IRF for CR27 on 25th July, 06th and 18th August 2019 using SLC HH polarization data.

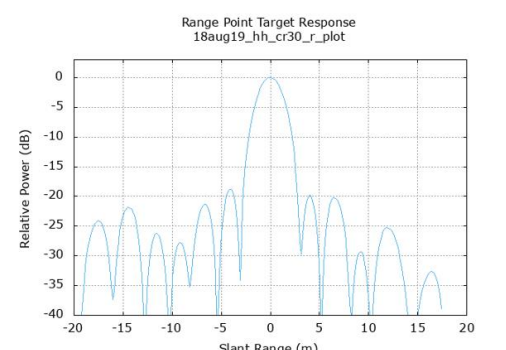
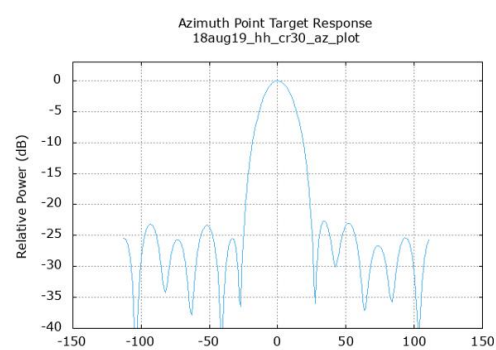
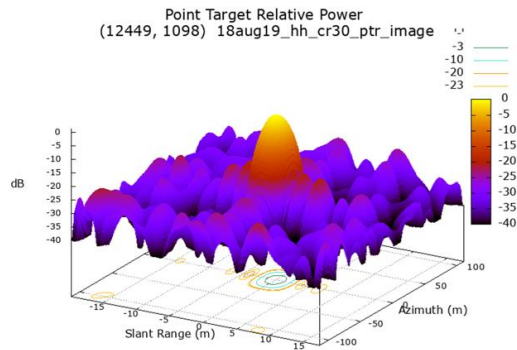
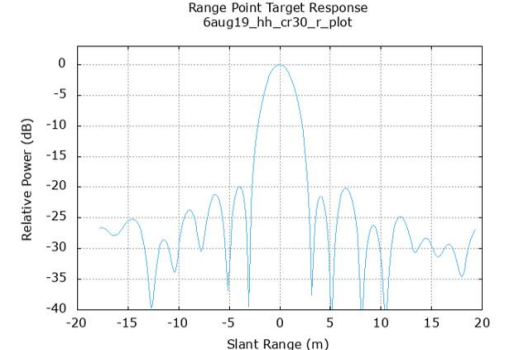
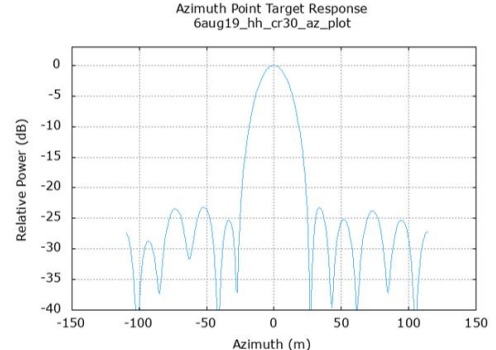
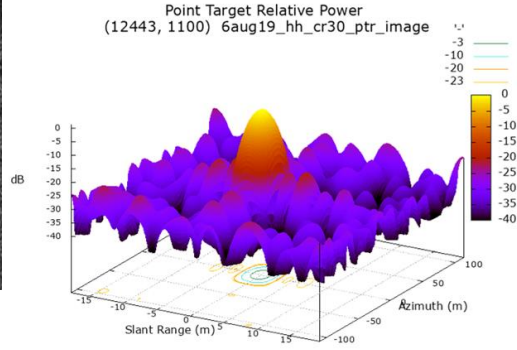
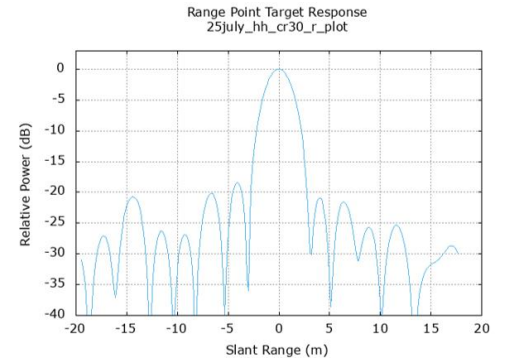
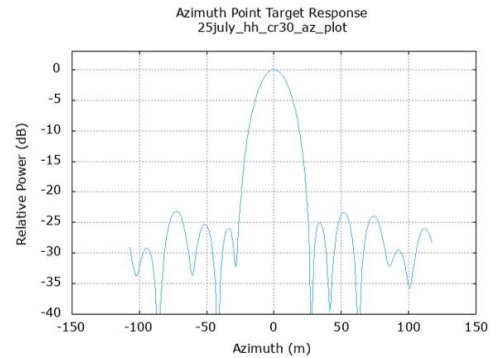
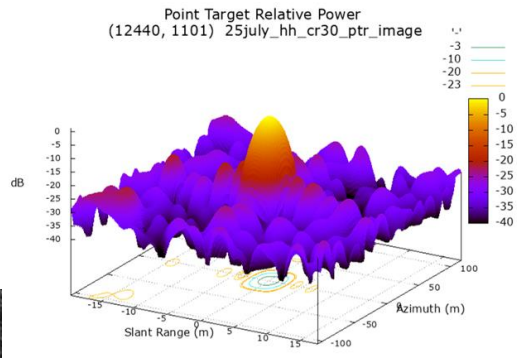
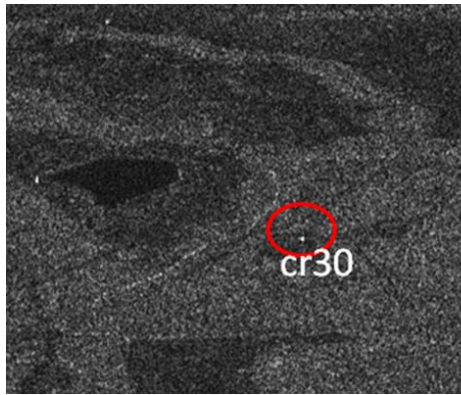


Figure 14: IRF for CR30 on 25th July, 06th and 18th August 2019 using SLC HH polarization data

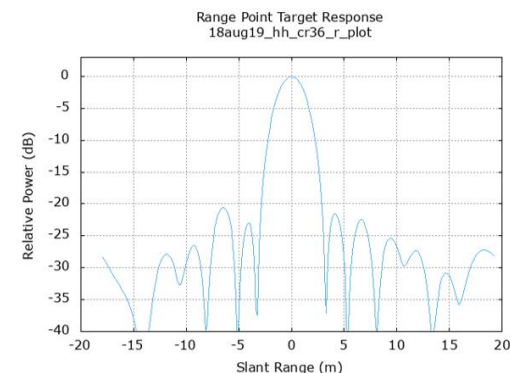
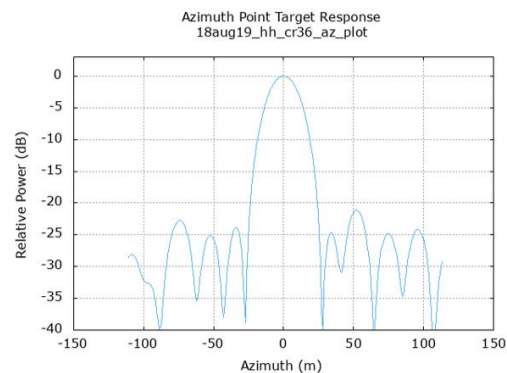
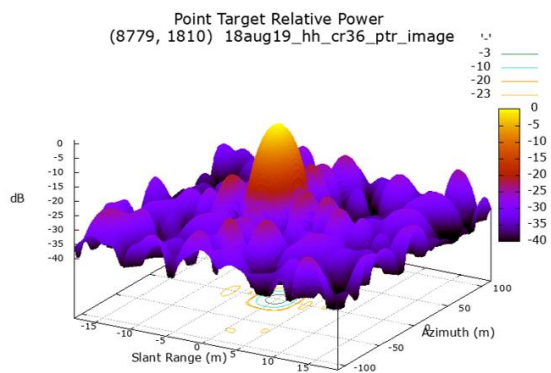
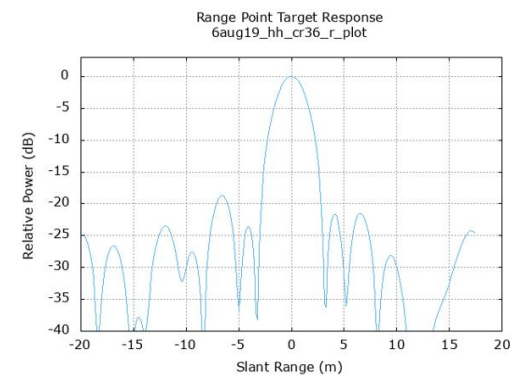
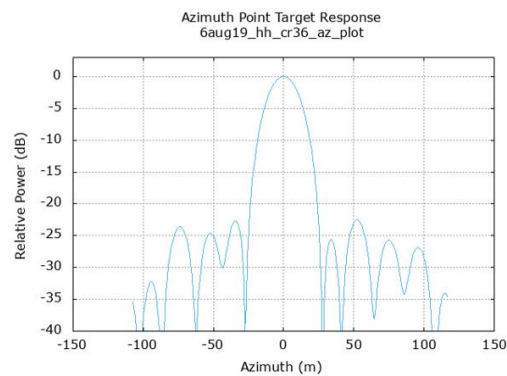
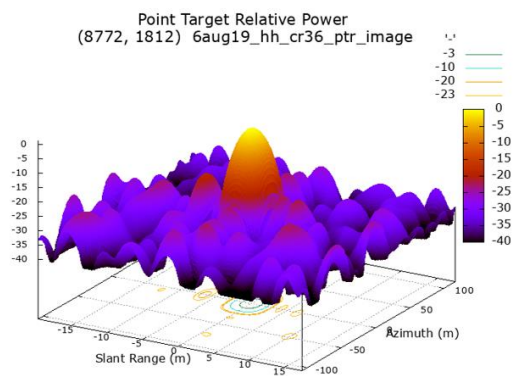
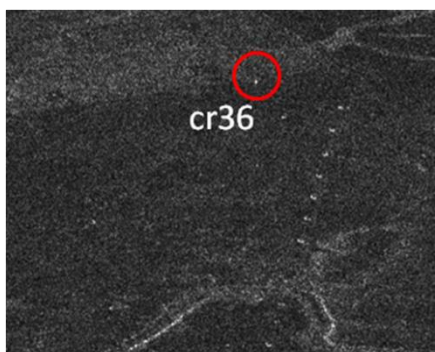
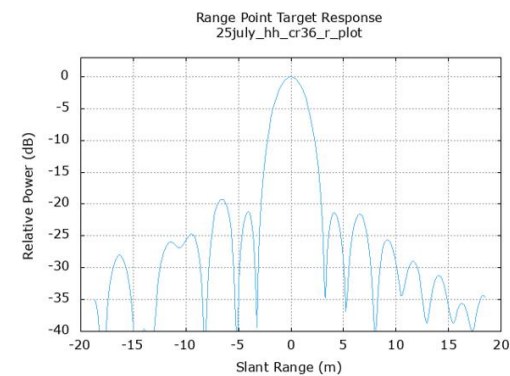
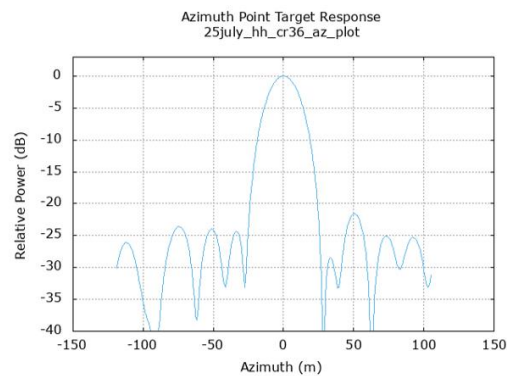
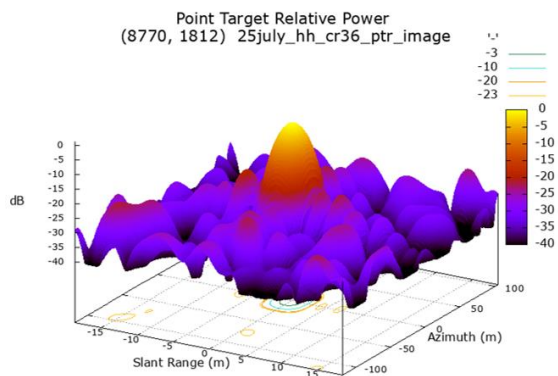


Figure 15: IRF for CR36 on 25th July, 06th and 18th August 2019 using SLC HH polarization data.

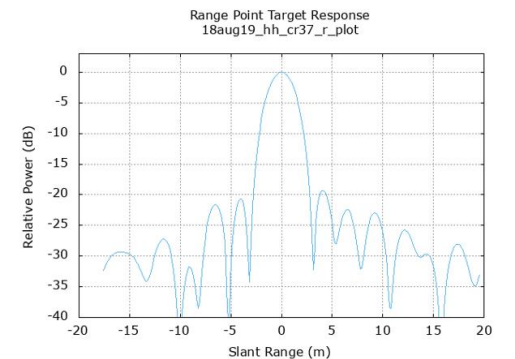
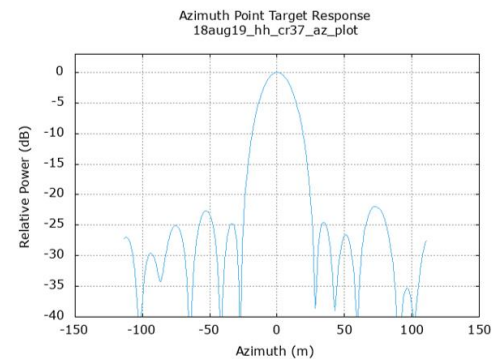
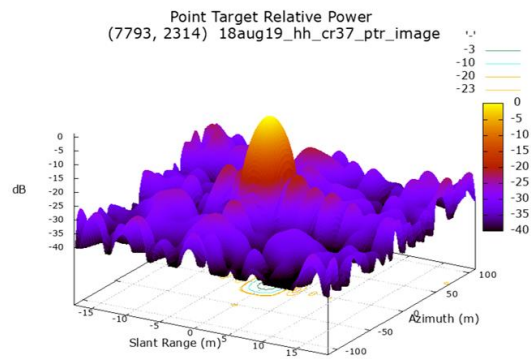
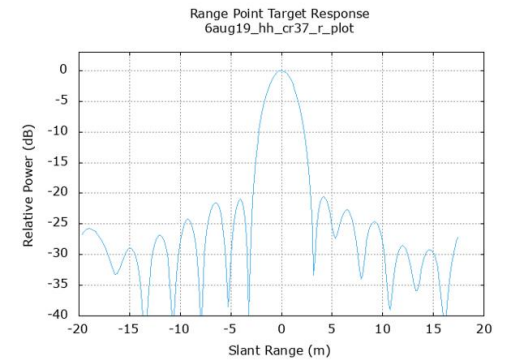
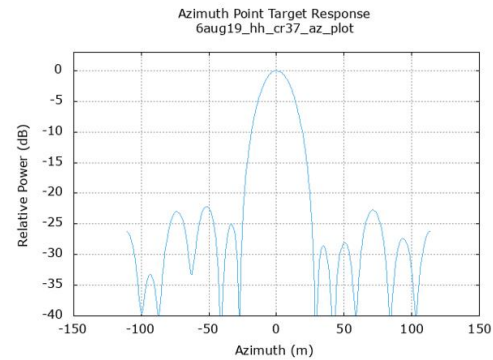
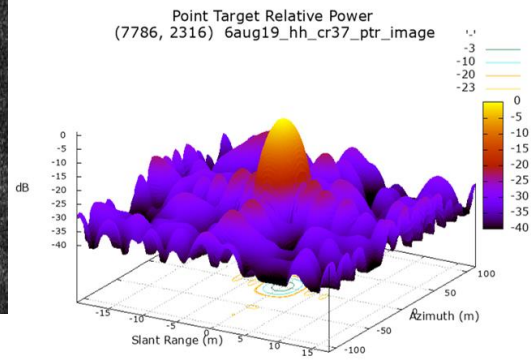
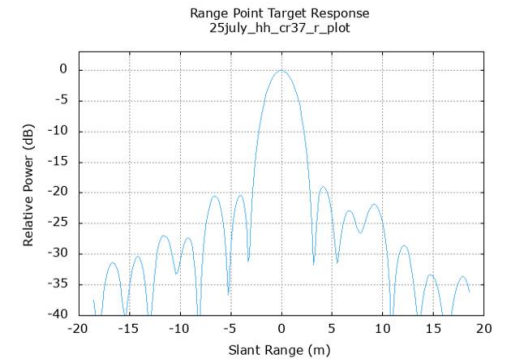
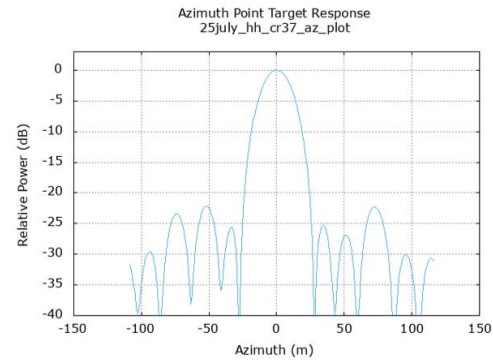
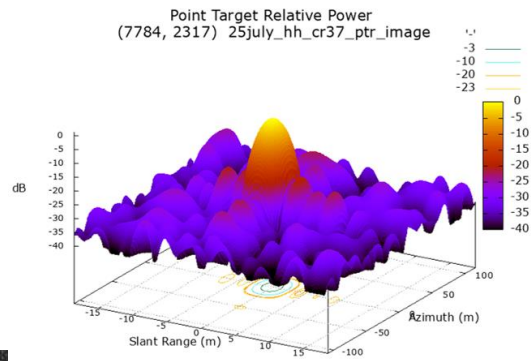
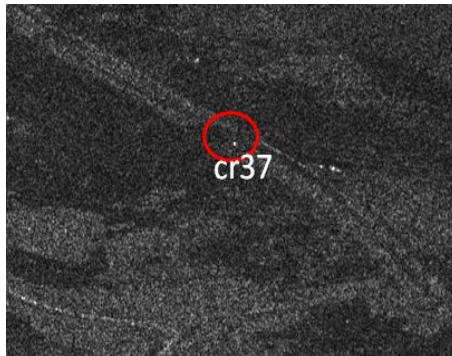


Figure 16: IRF for CR37 on 25th July, 06th and 18th August 2019 using SLC HH polarization data.

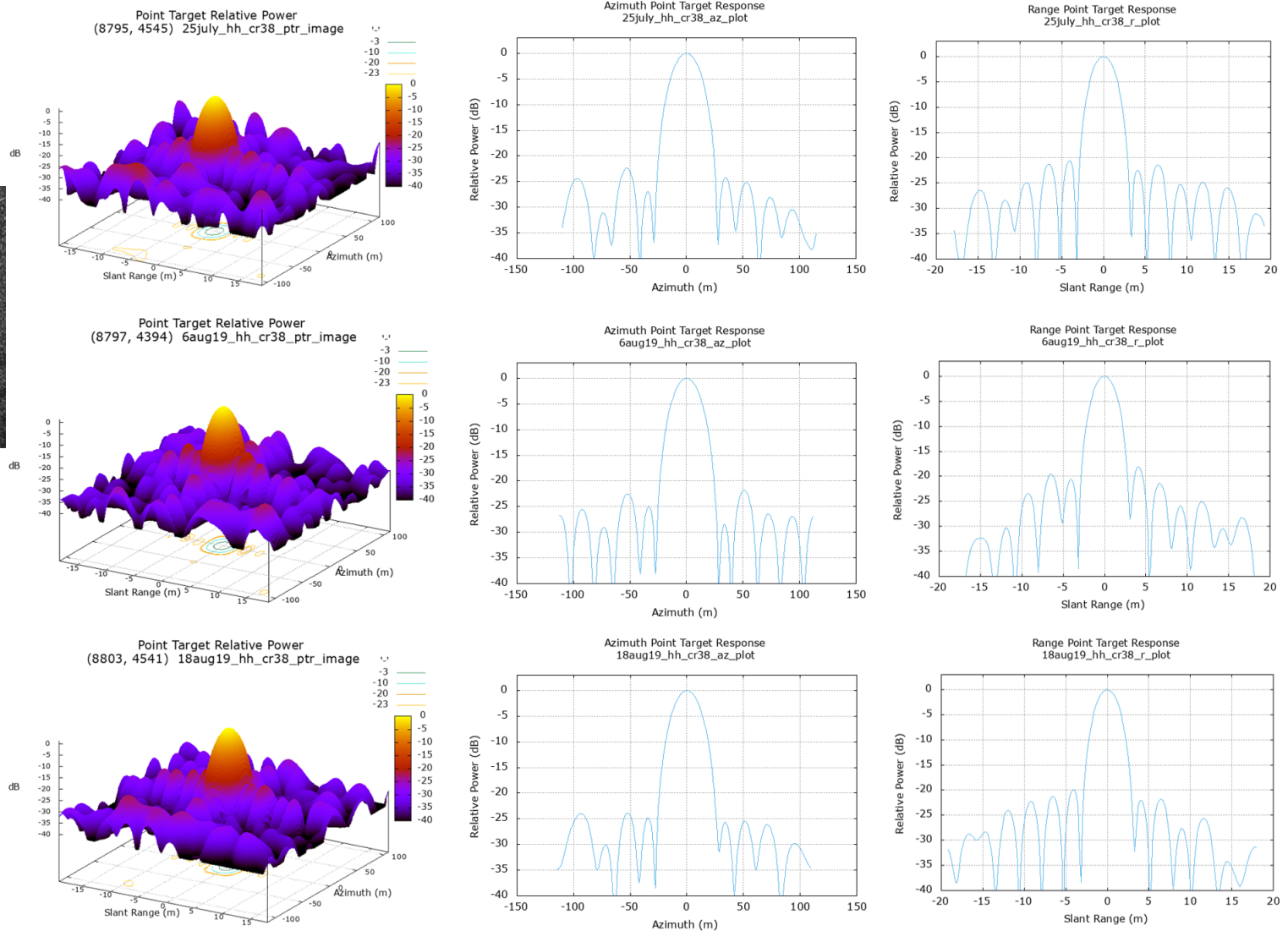
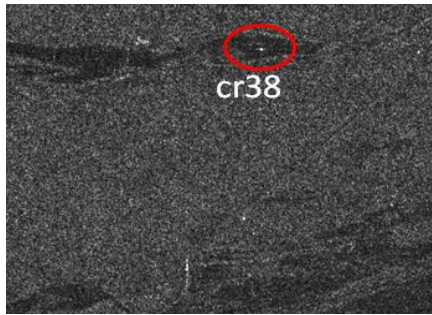


Figure 17: IRF for CR38 on 25th July, 06th and 18th August 2019 using SLC HH polarization data.

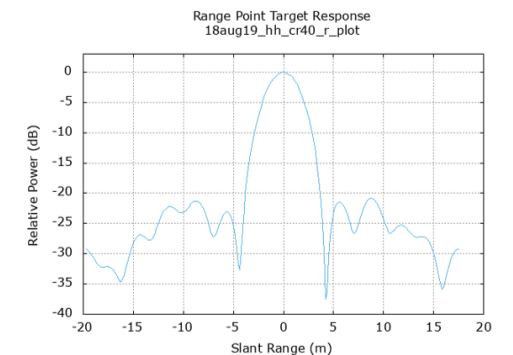
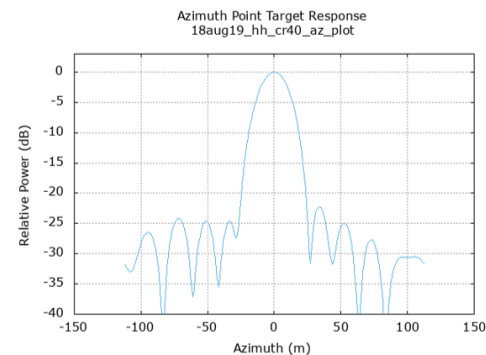
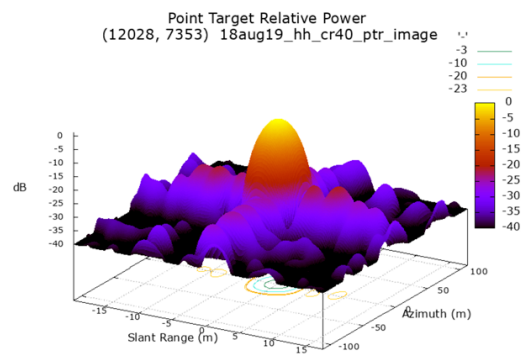
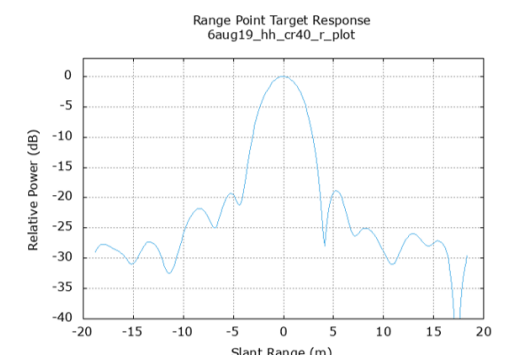
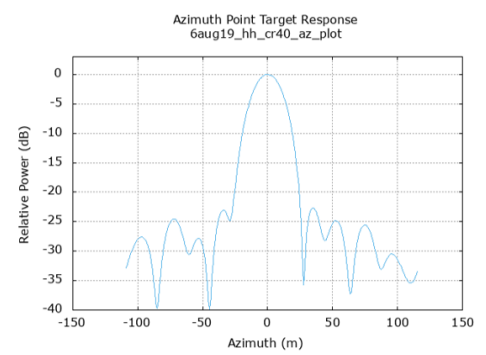
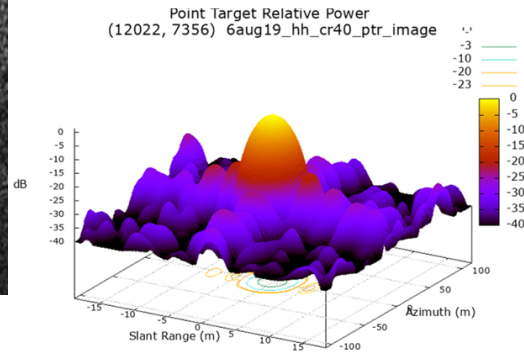
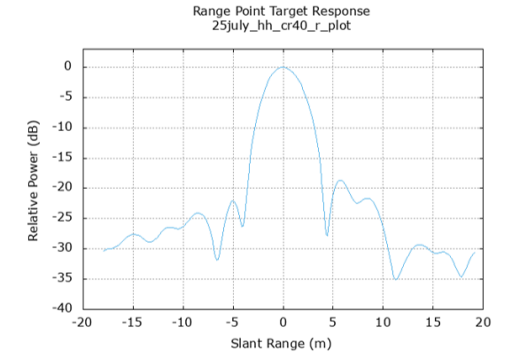
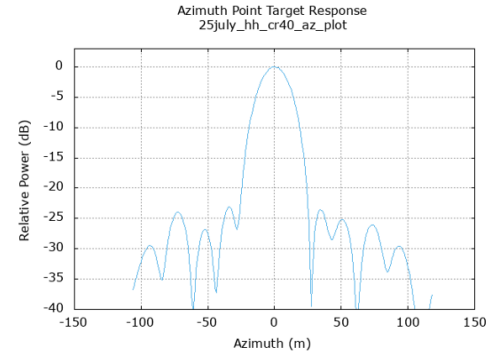
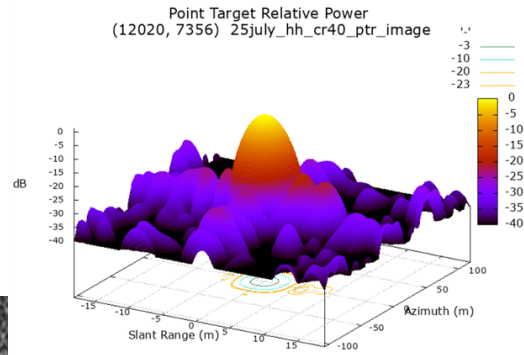
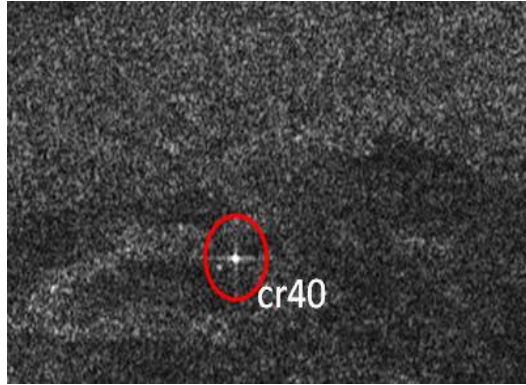


Figure 18: IRF for CR40 on 25th July, 06th and 18th August 2019 using SLC HH polarization data

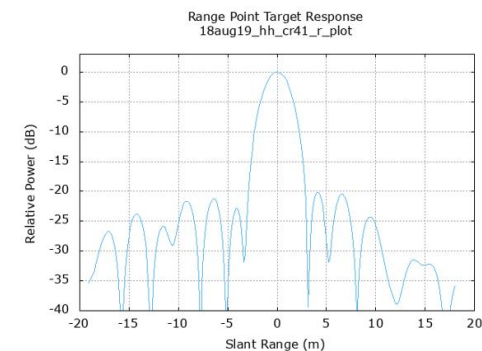
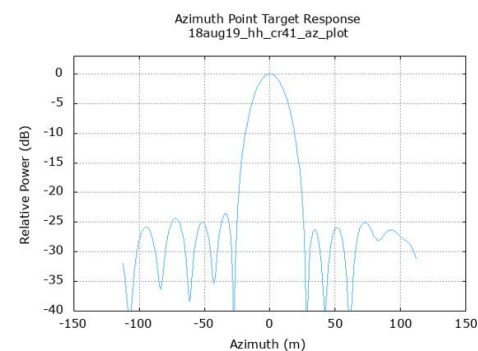
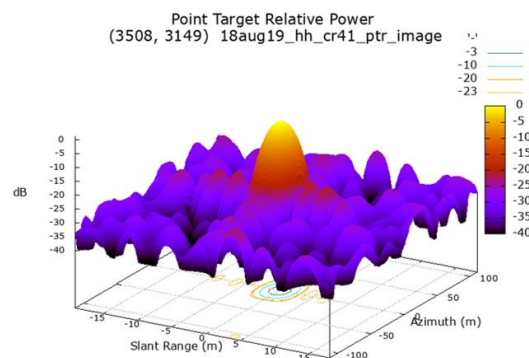
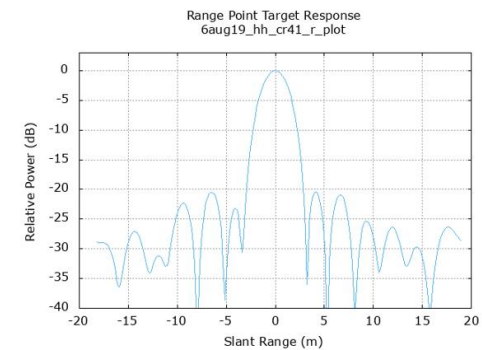
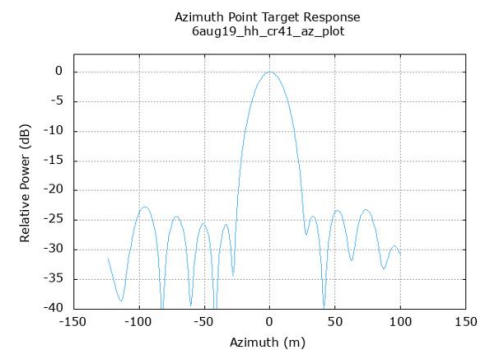
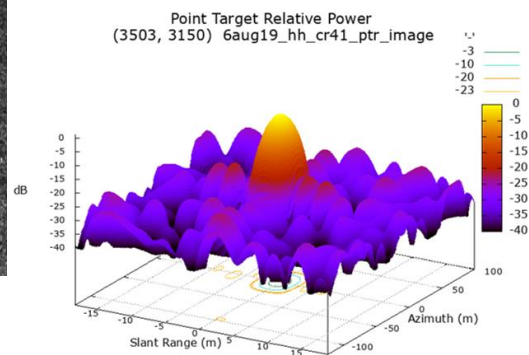
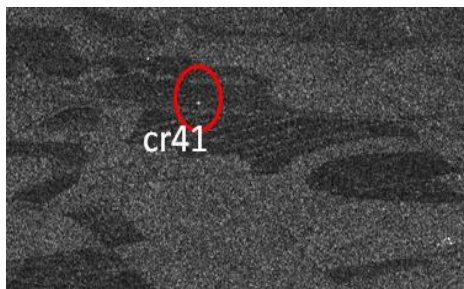
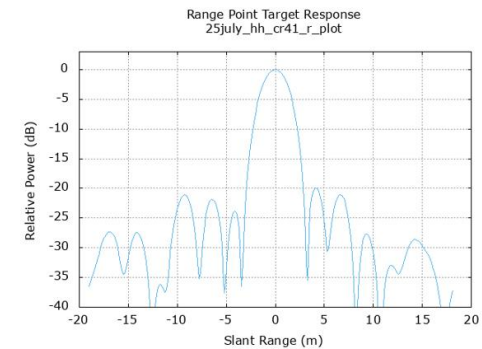
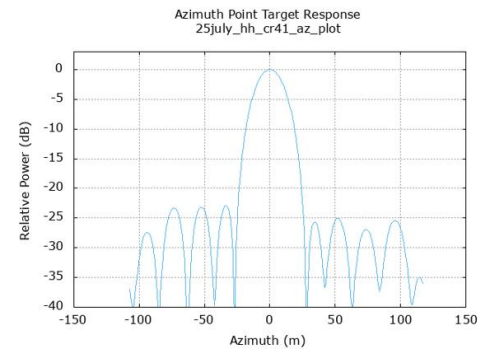
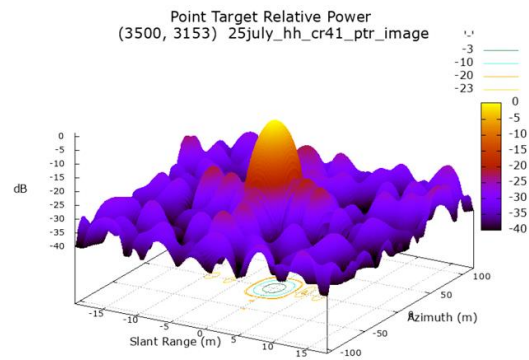


Figure 19: IRF for CR41 on 25th July, 06th & 18th August 2019 using SLC HH polarization data.

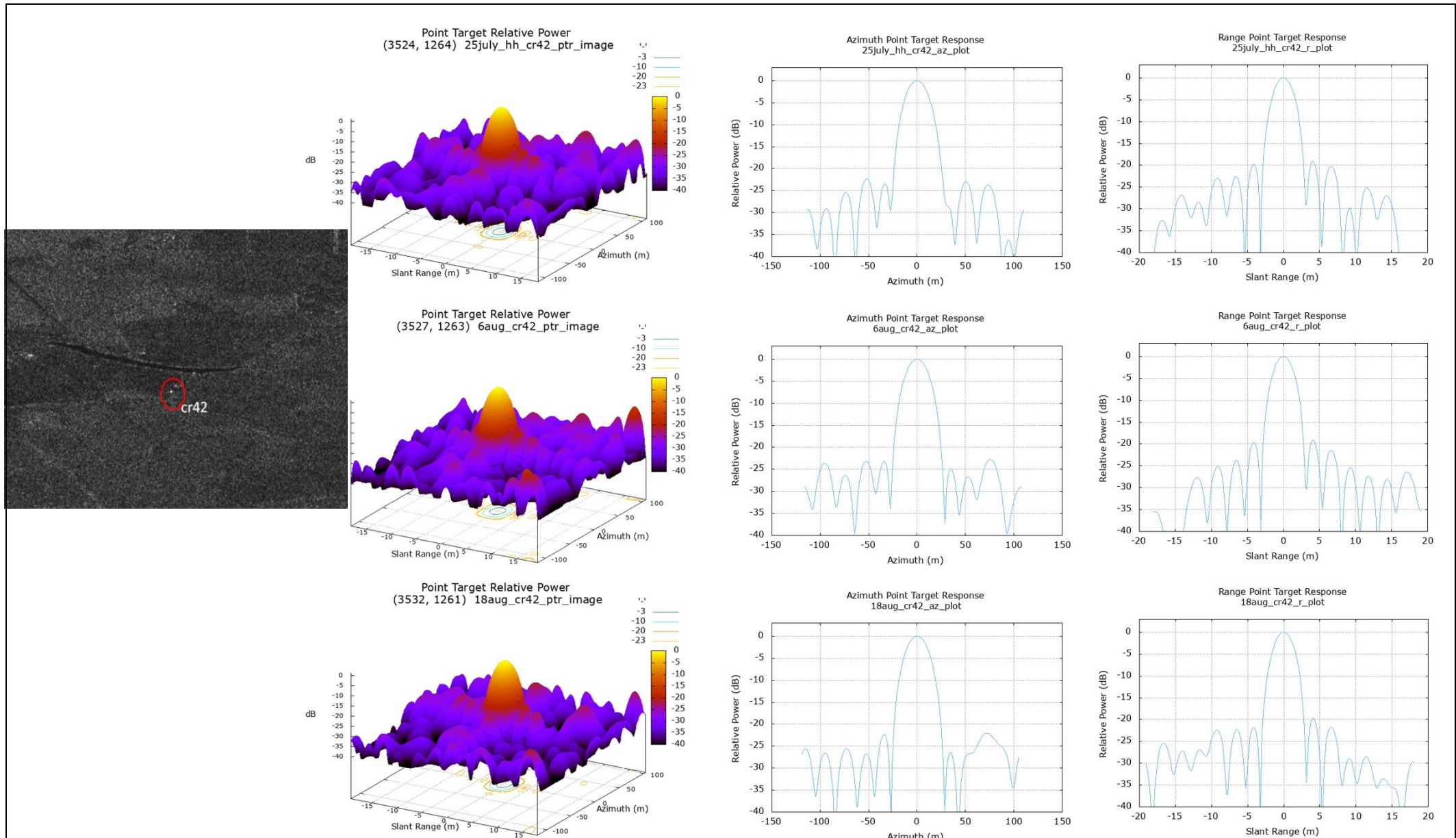


Figure 20: IRF for CR42 on 25th July, 06th & 18th August 2019 using SLC HH polarization data.

Table 10: Estimated range and azimuth resolutions

| CR_ID | Range_3dB width (meters) | Azimuth_3dB width (meters) | Range_3dB width (meters) | Azimuth_3dB width (meters) | Range_3dB width (meters) | Azimuth_3dB width (meters) |
|-------|----------------------------|----------------------------|------------------------------|----------------------------|------------------------------|----------------------------|
| | 25 th July 2019 | | 06 th August 2019 | | 18 th August 2019 | |
| CR19 | 2.793 | 23.317 | 2.773 | 21.784 | 2.75 | 22.177 |
| CR27 | 2.703 | 21.778 | 2.611 | 21.241 | 2.605 | 22.466 |
| CR30 | 2.535 | 21.673 | 2.681 | 21.533 | 2.683 | 21.583 |
| CR36 | 2.688 | 22.399 | 2.713 | 22.369 | 2.677 | 21.977 |
| CR37 | 2.783 | 21.995 | 2.61 | 21.894 | 2.466 | 22.601 |
| CR38 | 2.639 | 21.728 | 2.584 | 21.12 | 2.792 | 21.085 |
| CR40 | 3.789 | 21.695 | 3.545 | 21.997 | 3.298 | 22.468 |
| CR41 | 2.531 | 22.257 | 2.667 | 21.914 | 2.71 | 22.077 |
| CR42 | 2.596 | 22.895 | 2.573 | 22.802 | 2.727 | 22.996 |

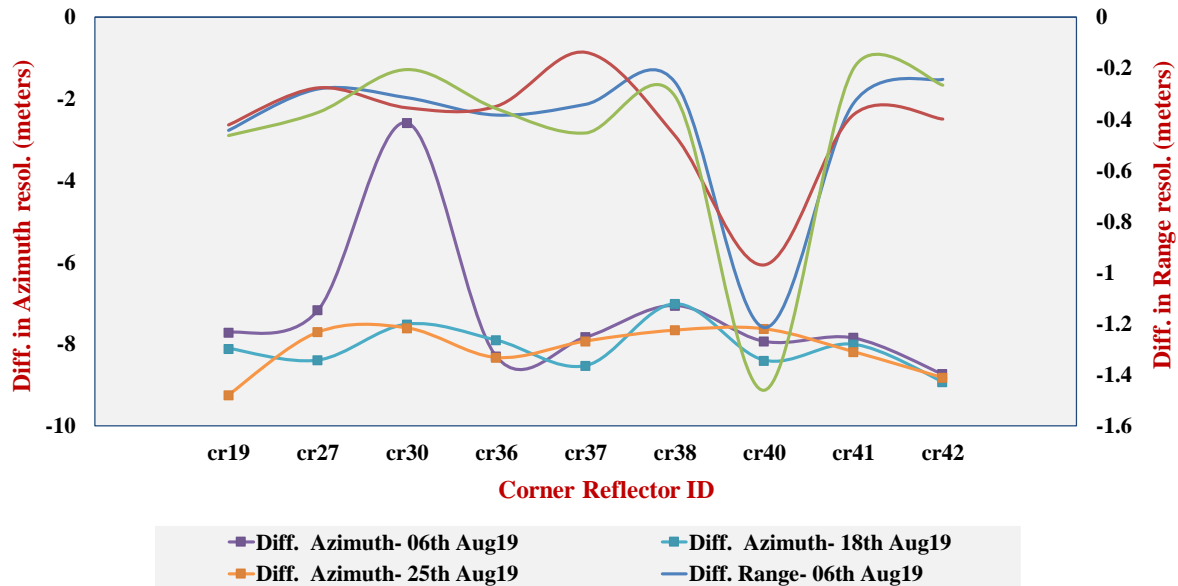


Figure 21: Difference between Estimated and Specified resolution in Range (2.329 m) and Azimuth (14.068 m).

The azimuth and range resolution are estimated for each corner reflector is given in Table 10 and graph is plotted for difference estimated from specified for both azimuth and range direction in Figure 21. At CR40 the range resolution is 3.54 m, 3.29 m, 3.78 m for 25th July19, 06th and 18th Aug19, which is greater than specified range resolution of 2.39 m. The estimated spatial resolution in range and azimuth direction are same and consistent for each corner reflector. The estimated range resolution is 2.66 ± 0.09 m and azimuth resolution is 21.87 ± 1.25 m.

Peak Side Lobe Ratio (PSLR)

The Range and Azimuth peak to side lobe ratios are estimated from the impulse response function of each CR, given in Table 11 and in Figure 22. The mean peak to side lobe ratio in range direction is -19.51 ± 0.87 dB and in azimuth direction PSLR found to be -22.23 ± 0.94 dB.

Table 11: Estimated PSLR in range and azimuth direction

| CR_ID | PSLR | PSLR | PSLR | PSLR | PSLR | PSLR |
|-------|----------------------------|----------|------------------------------|----------|------------------------------|----------|
| | Range_ | Azimuth_ | Range_ | Azimuth_ | Range_ | Azimuth_ |
| | dB | dB | dB | dB | dB | dB |
| | 25 th July 2019 | | 06 th August 2019 | | 18 th August 2019 | |
| CR19 | -20.440 | -21.246 | -21.342 | -23.449 | -19.34 | -22.144 |
| CR27 | -19.471 | -22.493 | -18.998 | -21.353 | -19.592 | -21.563 |
| CR30 | -18.486 | -23.201 | -19.885 | -23.176 | -18.791 | -22.75 |
| CR36 | -19.257 | -21.532 | -18.7 | -22.507 | -20.549 | -21.113 |
| CR37 | -18.997 | -22.137 | -20.63 | -22.198 | -19.30 | -21.92 |
| CR38 | -20.542 | -22.353 | -18.051 | -21.77 | -19.908 | -23.912 |
| CR40 | -18.633 | -23.118 | -18.212 | -22.716 | -17.867 | -22.245 |
| CR41 | -17.756 | -22.879 | -20.415 | -22.749 | -20.175 | -23.577 |
| CR42 | -19.096 | -22.373 | -19.126 | -22.787 | -19.606 | -22.063 |

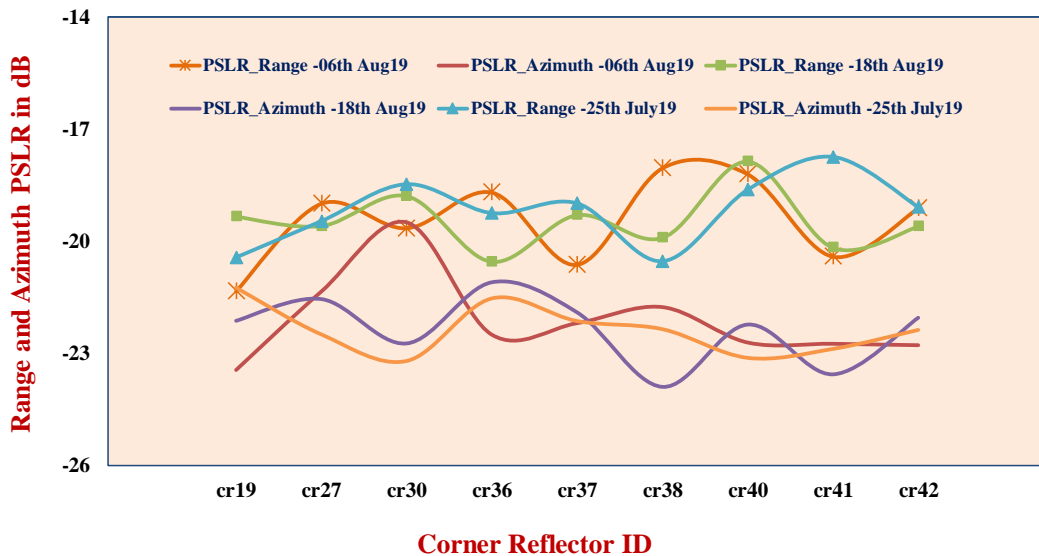


Figure 22: Peak to Side Lobe Ratio obtained in Range and Azimuth direction using SLC HH pol. Data

Integrated Side Lobe Ratio (ISLR)

The Range and Azimuth integrated side lobe ratios are estimated from the impulse response function of each CR, given in Table 12 and in Figure 23. The mean integrated side lobe ratio in range direction is -18.59 ± 0.64 dB and in azimuth direction ISLR found to be -21.29 ± 1.35 dB.

Table 12: Estimated ISLR in range and azimuth direction

| CR_ID | ISLR Range_ dB | ISLR Azimuth_ dB | ISLR Range_ dB | ISLR Azimuth_ dB | ISLR Range_ dB | ISLR Azimuth_ dB |
|-------|----------------------------|------------------|------------------------------|------------------|------------------------------|------------------|
| | 25 th July 2019 | | 06 th August 2019 | | 18 th August 2019 | |
| CR19 | -18.910 | -21.213 | -20.268 | -22.883 | -18.691 | -21.790 |
| CR27 | -18.435 | -20.510 | -17.992 | -20.004 | -18.912 | -20.270 |
| CR30 | -18.576 | -23.995 | -17.869 | -20.215 | -17.711 | -20.984 |
| CR36 | -18.265 | -19.954 | -18.348 | -20.492 | -19.646 | -19.847 |
| CR37 | -17.457 | -20.528 | -18.488 | -20.384 | -18.188 | -20.116 |
| CR38 | -19.213 | -22.257 | -17.381 | -22.048 | -18.421 | -22.208 |
| CR40 | -17.486 | -20.650 | -17.257 | -20.343 | -17.277 | -20.525 |
| CR41 | -19.165 | -21.433 | -18.736 | -21.059 | -18.846 | -22.872 |
| CR42 | -17.884 | -18.868 | -18.453 | -20.218 | -18.868 | -20.114 |

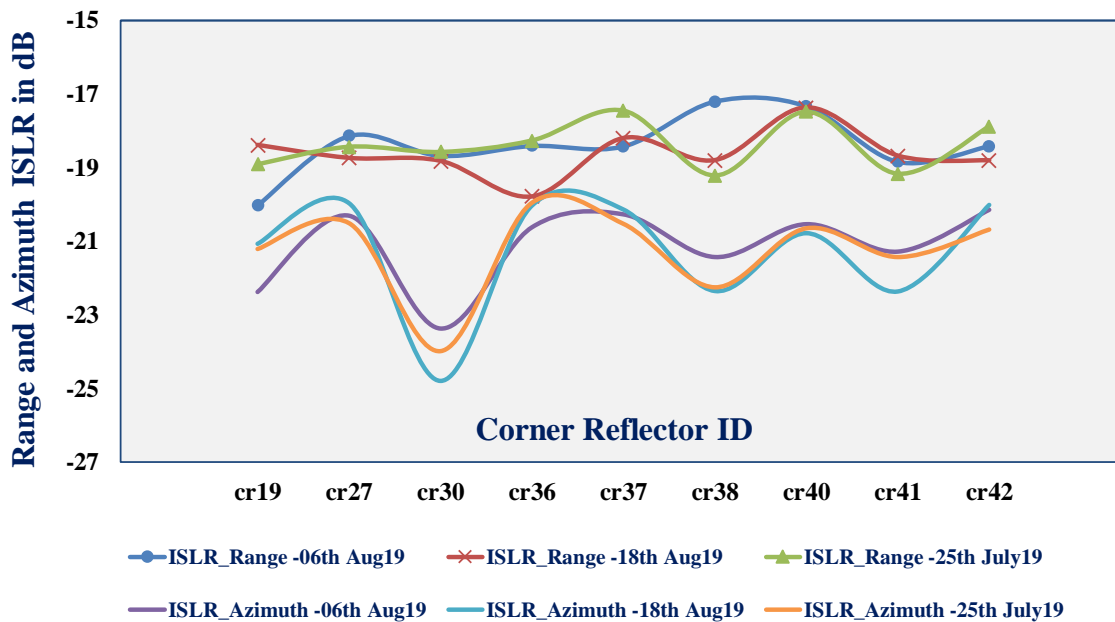


Figure 23: Integrated Side Lobe Ratio obtained in Range and Azimuth direction using SLC HH pol. data

6.2 Radiometric and polarimetric calibration of airborne UAVSAR L-band data.

6.2.1 Radiometric and Phase Parameters

The inputs used to estimate Radar Cross Section (RCS) of each corner reflector are given in Table 13. The difference between theoretical RCS and estimated RCS for HH and VV polarization is estimated using GAMMA –Msys 2 software. GAMMA software estimates the RCS, by using integral power method (*Shweta, et al. 2017*). Table 14 gives the pixel values of number of clutters locations considered in the process of RCS estimation and deviation from theoretical RCS. The RCS difference of each CR is found to be less than 1dB for both the polarization channels as shown in Figure 24, which shows that the dataset is radiometrically corrected. Impulse response function of each corner reflector is generated for HH polarization as show in Figure 29 and IRF in VV polarizations as shown in Figure 30 respectively. The average peak power value of each CR in HH and VV polarization are shown in Figure 25. The difference between peak powers of HH and VV channels are illustrated in Figure 26 respectively.

Table 13: Attributes used to calculate RCS of each CR with respect to Incidence and Azimuth angle

| Corner reflector ID | Elevation angle + incidence angle @CR (deg) | incidence angle (in radians) | $\Omega = \cos(\theta) + (\sin\phi + \cos\phi)\sin(\theta)$ | $\frac{4*\pi*a*a*a}{\lambda*\lambda}$ | Square $(\Omega-2/\Omega)$ | RCS |
|---------------------|---|------------------------------|---|---------------------------------------|----------------------------|----------|
| 0 | 53.4286 | 0.9325 | 1.7316 | 7816.58 | 0.332467 | 2598.752 |
| 1 | 57.11211 | 0.9968 | 1.730561 | 7816.58 | 0.330472 | 2583.158 |
| 2 | 56.88715 | 0.9929 | 1.73083 | 7816.58 | 0.330987 | 2587.186 |
| 3 | 57.93546 | 1.0112 | 1.72935 | 7816.58 | 0.328153 | 2565.037 |
| 4 | 58.14773 | 1.0149 | 1.72898 | 7816.58 | 0.327446 | 2559.51 |
| 5 | 58.36418 | 1.0186 | 1.728579 | 7816.58 | 0.326679 | 2553.514 |
| 6 | 60.01325 | 1.0474 | 1.724708 | 7816.58 | 0.319328 | 2496.056 |
| 7 | 62.91842 | 1.0981 | 1.714417 | 7816.58 | 0.300128 | 2345.974 |
| 8 | 60.67854 | 1.0590 | 1.722742 | 7816.58 | 0.315621 | 2467.08 |
| 9 | 62.44762 | 1.0899 | 1.716385 | 7816.58 | 0.30376 | 2374.367 |
| 10 | 61.16324 | 1.0675 | 1.721163 | 7816.58 | 0.312658 | 2443.917 |
| 11 | 62.92029 | 1.0982 | 1.714409 | 7816.58 | 0.300113 | 2345.858 |
| 12 | 63.11911 | 1.1016 | 1.713543 | 7816.58 | 0.29852 | 2333.409 |

Azimuth angle in radians (ϕ) = 0.785398163 (45 deg.)

Table 14: Details of clutter and deviation of RCS from theoretical value

| CR | Clutter | Polarization | Theoretical RCS in m² | Deviation of RCS from theoretical (in dB) |
|------------------------------------|---------------------|---------------------|--|--|
| CR00 (2412,49637) | C1 (2452, 49683) | HH VV | 2598.752 | -1.0138 -1.0135 |
| CR01 (2801,49376) | C1 | HH VV | 2583.158 | -0.8127 -0.6759 |
| CR02 (2831,48368) | C2 (4132, 48936) | HH VV | 2587.186 | -0.9197 -0.6197 |
| CR03 (3053,48494) | C2 | HH VV | 2565.037 | -0.4903 -1.1652 |
| CR04 (3277,48626) | C2 | HH VV | 2559.51 | -0.0193 -0.1678 |
| CR05 (3508,48758) | C2 | HH VV | 2553.514 | -0.6766 -0.1305 |
| CR06 (3741,48887) | C2 | HH VV | 2496.056 | -0.7555 0.0883 |
| CR07 (3978,49017) | C2 | HH VV | 2345.974 | -0.3238 0.4119 |
| CR08 (4218,49148) | C2 | HH VV | 2467.08 | -0.4423 0.0916 |
| CR09 (4443,49272) | C2 | HH VV | 2374.367 | 0.5184 0.7810 |
| CR10 (4687,49396) | C3 (4623, 49458) | HH VV | 2443.917 | 0.6300 0.4032 |
| CR11 (4939,49526) | C4 (5050, 49583) | HH VV | 2345.858 | -0.1654 -0.1964 |
| CR12 (5181,49658) | C4 | HH VV | 2333.409 | 0.2111 -0.2595 |
| | | | <i>RCS diff. Mean in HH, VV (A)</i> | <i>0.9339 0.9574</i> |

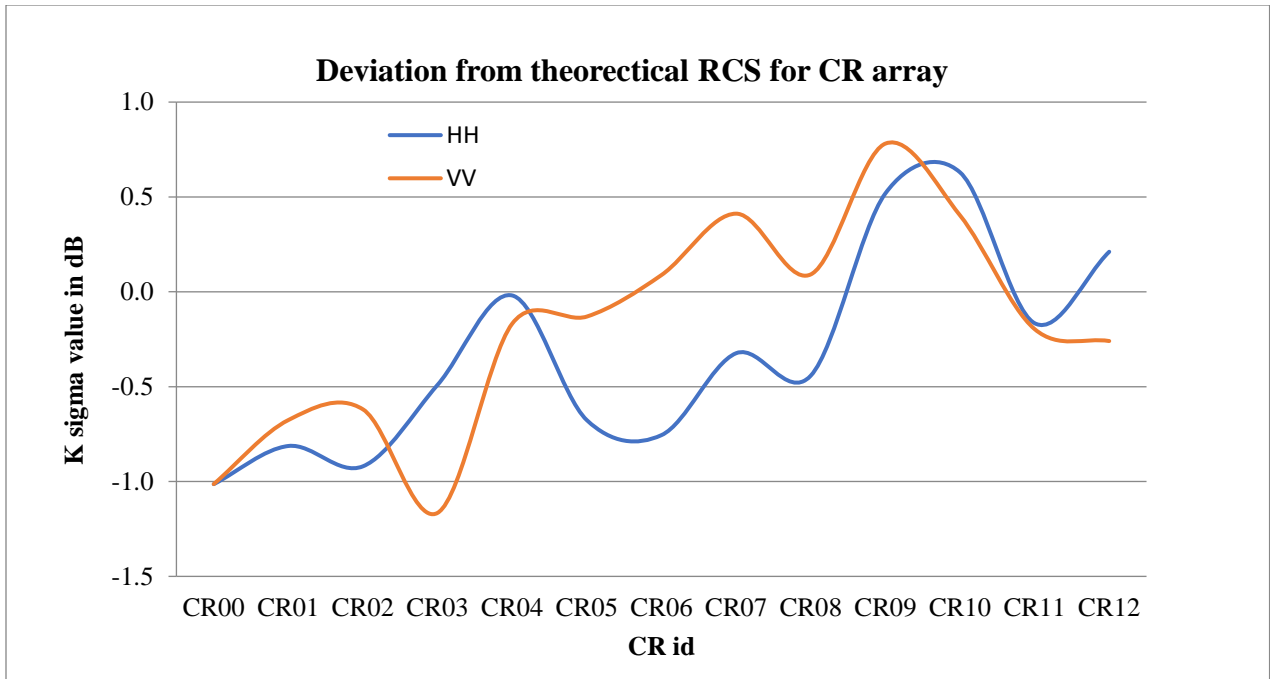


Figure 24: Deviation from theoretical RCS for CR array (HH and VV pol.)

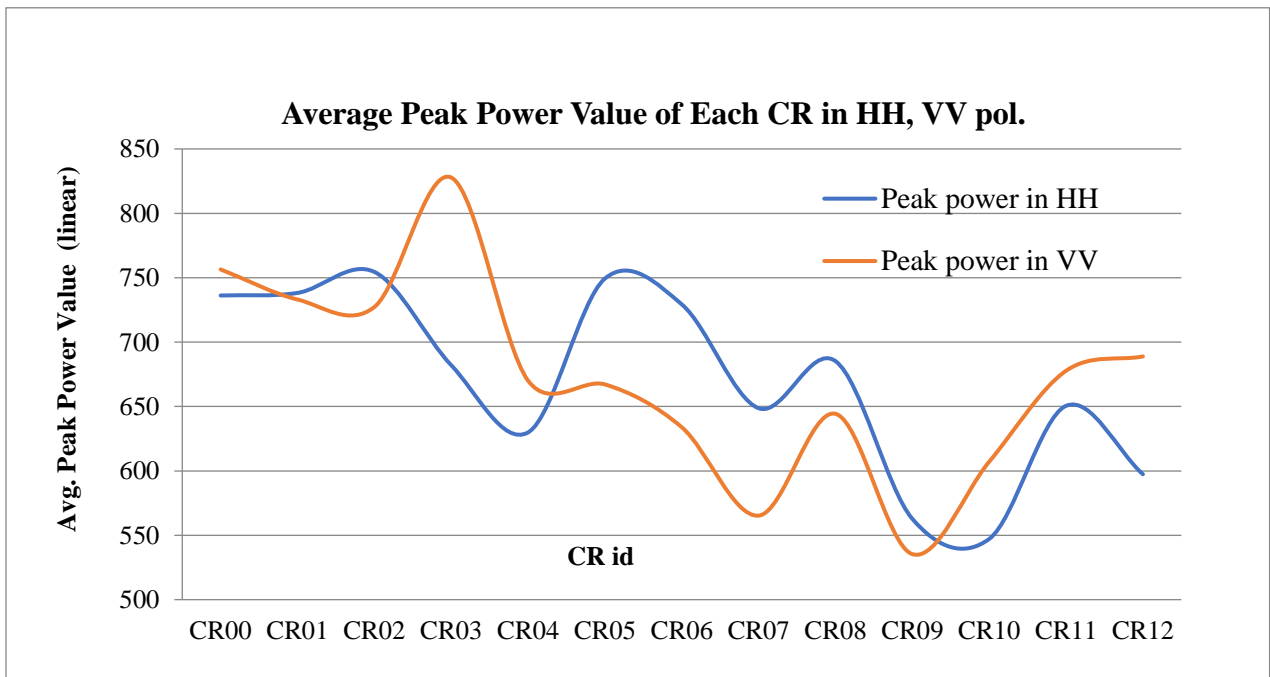


Figure 25: Peak power values for HH and VV pol. in linear amplitude units

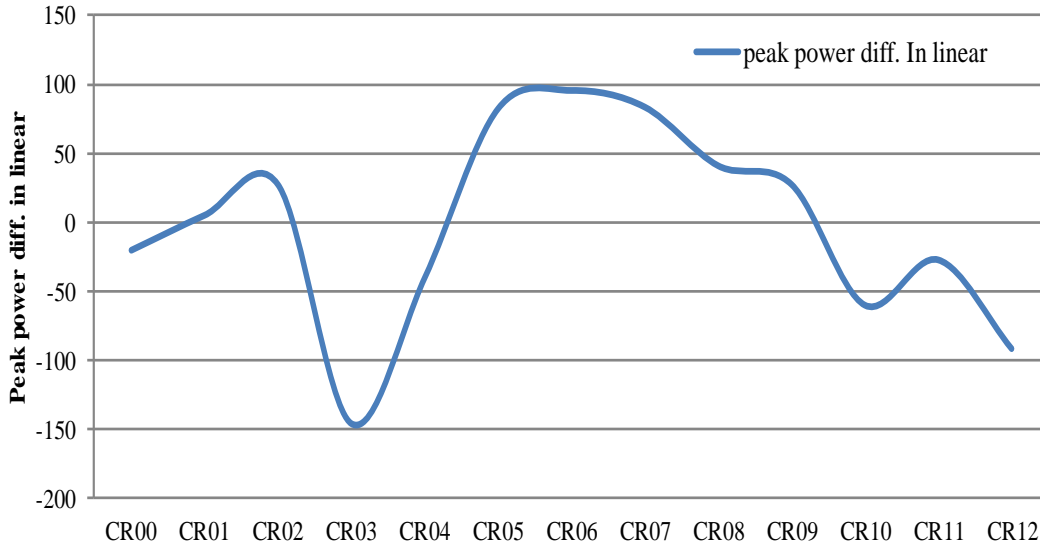


Figure 26: Peak power difference between HH and VV pol. in linear amplitude units

Peak phase values of each CR are calculated for HH and VV polarized channels as per Table 15. The peak phase difference of each CR for HH and VV channels are shown in Figure 28.

Table 15: Peak phase values for HH and VV polarization

| CR | Peak Phase in HH pol. (in degrees) | Peak Phase in VV pol. (in degrees) | Peak Phase difference (VV-HH) |
|------|------------------------------------|------------------------------------|-------------------------------|
| CR00 | -121.487 | -119.205 | 2.282 |
| CR01 | -130.337 | -123.324 | 7.013 |
| CR02 | -238.713 | -233.924 | 4.789 |
| CR03 | -68.943 | -66.111 | 2.832 |
| CR04 | -66.739 | -62.981 | 3.758 |
| CR05 | -69.134 | -67.018 | 2.116 |
| CR06 | -319.303 | 38.106 | 357.409 |
| CR07 | -4.406 | -2.057 | 2.349 |
| CR08 | -127.512 | -131.084 | -3.572 |
| CR09 | -182.427 | -185.639 | -3.212 |
| CR10 | -97.39 | -98.558 | -1.168 |
| CR11 | -244.346 | -245.052 | -0.706 |
| CR12 | -245.556 | -243.097 | 2.459 |
| | | <i>Mean Phase in deg.(phi_s)</i> | <i>1.5783°</i> |

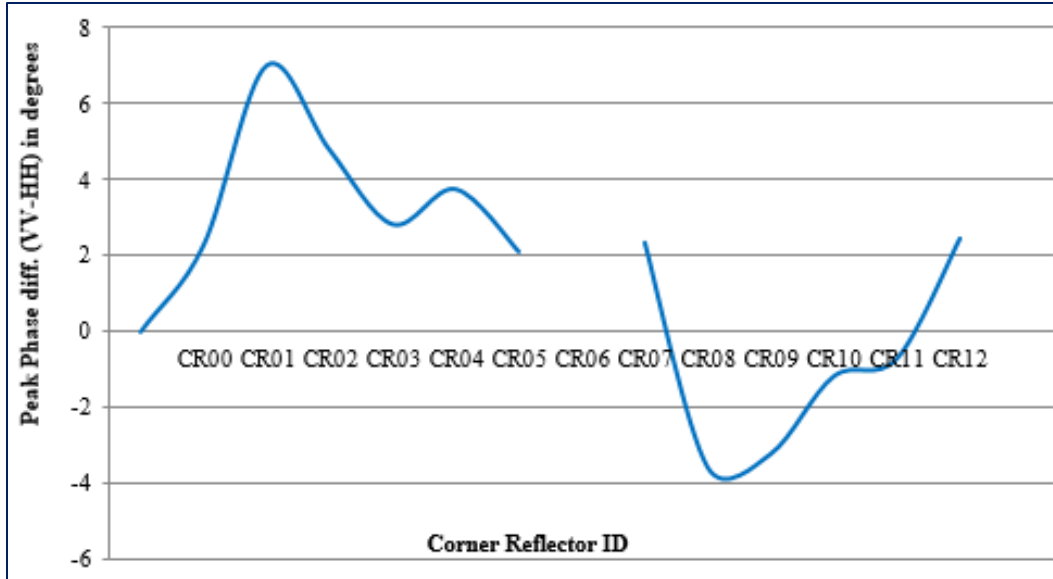


Figure 27: Phase difference HH-VV pol

Table 16: Range and Azimuth resolution estimated from IRF of the point targets

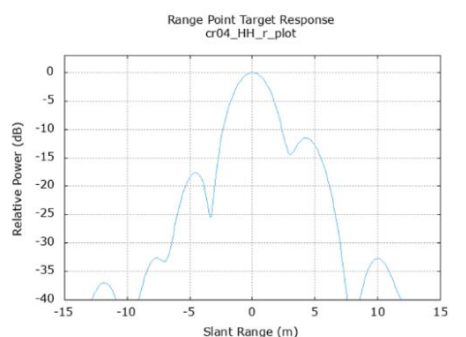
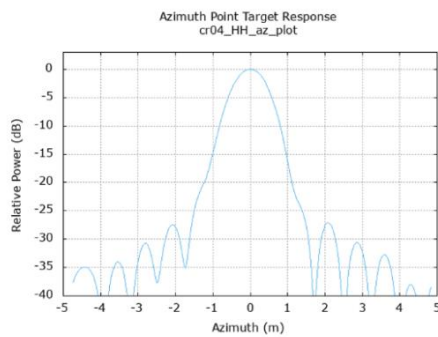
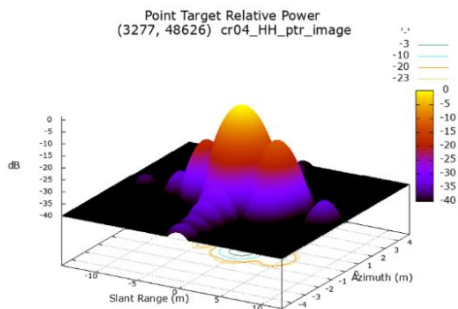
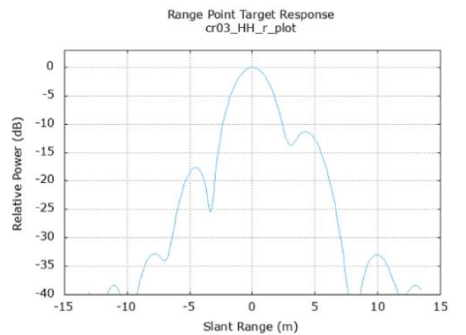
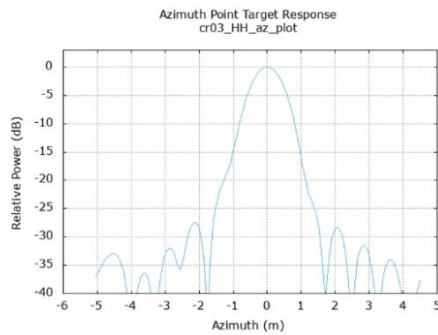
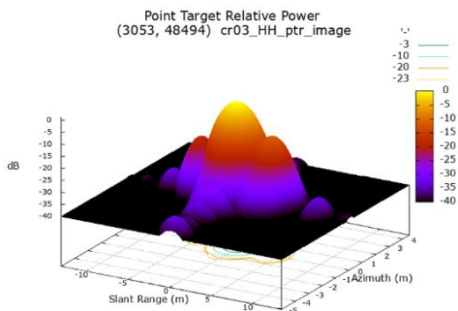
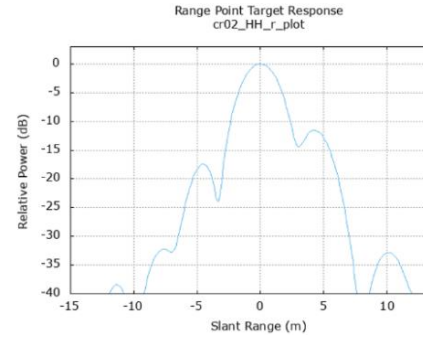
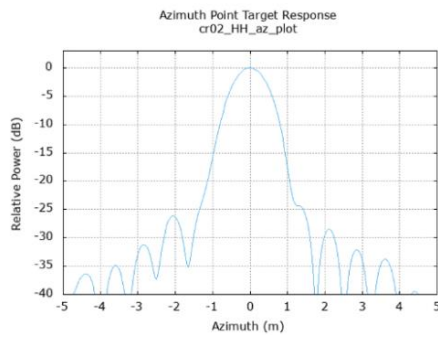
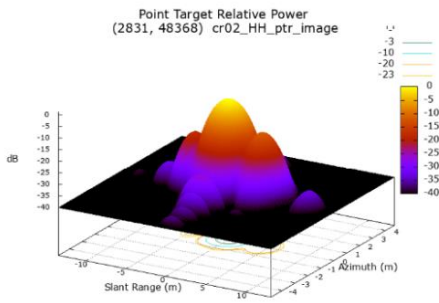
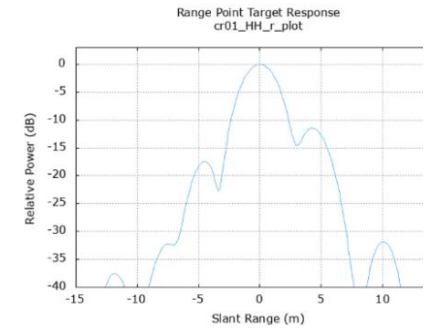
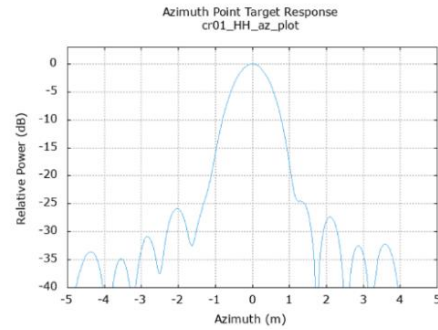
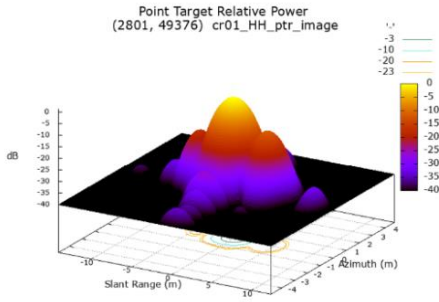
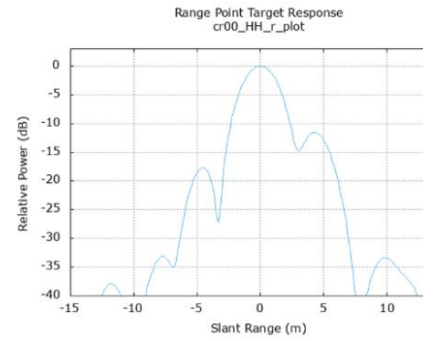
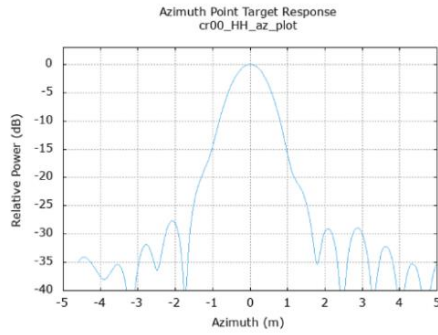
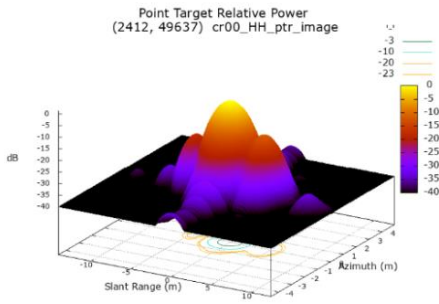
| CR | Range_3dB width | | Azimuth_3dB width | |
|-------------|----------------------------|---|------------------------------|---|
| | Estimated range resolution | Difference between estimated and specified range resolution (1.8 m) | Estimated azimuth resolution | Difference between estimated and specified azimuth resolution (0.8 m) |
| CR00 | 2.686 | 0.886 | 0.942 | 0.142 |
| CR01 | 2.627 | 0.827 | 0.94 | 0.14 |
| CR02 | 2.696 | 0.896 | 0.893 | 0.093 |
| CR03 | 2.626 | 0.826 | 0.945 | 0.145 |
| CR04 | 2.642 | 0.842 | 0.947 | 0.147 |
| CR05 | 2.688 | 0.888 | 0.883 | 0.083 |
| CR06 | 2.744 | 0.944 | 0.926 | 0.126 |
| CR07 | 2.666 | 0.866 | 0.951 | 0.151 |
| CR08 | 2.755 | 0.955 | 0.934 | 0.134 |
| CR09 | 2.64 | 0.84 | 0.926 | 0.126 |
| CR10 | 2.662 | 0.862 | 0.949 | 0.149 |
| CR11 | 2.743 | 0.943 | 0.915 | 0.115 |
| CR12 | 2.81 | 1.01 | 0.944 | 0.144 |

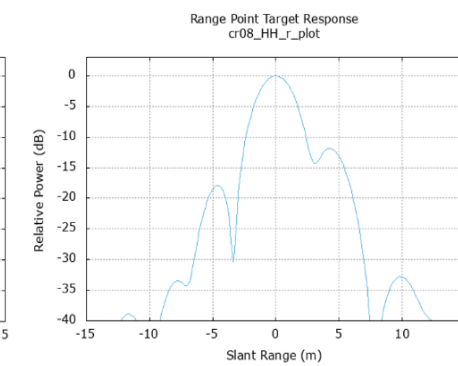
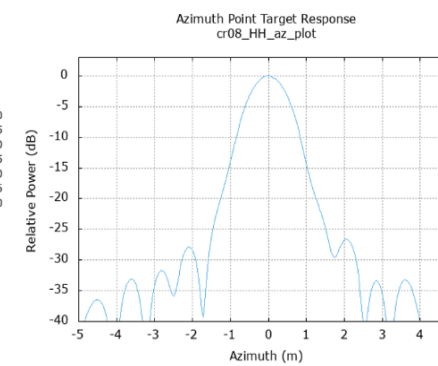
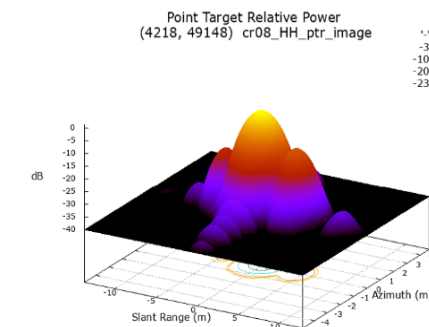
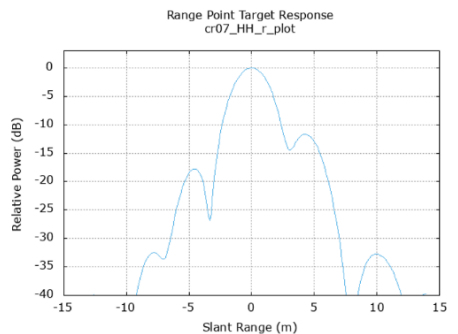
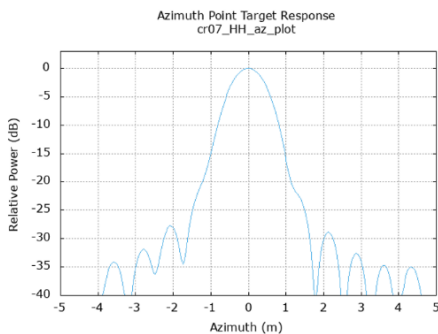
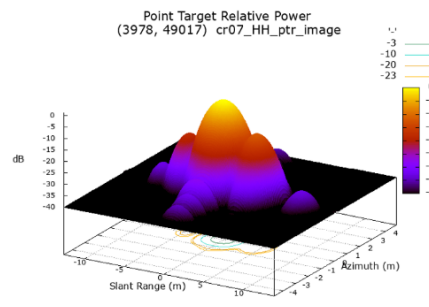
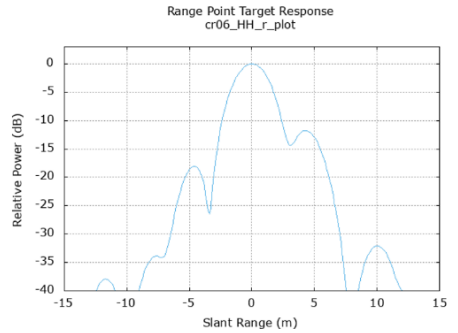
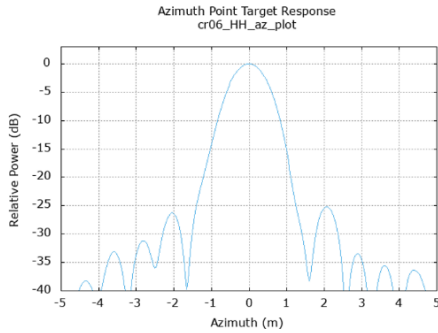
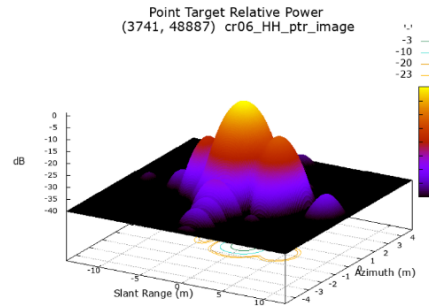
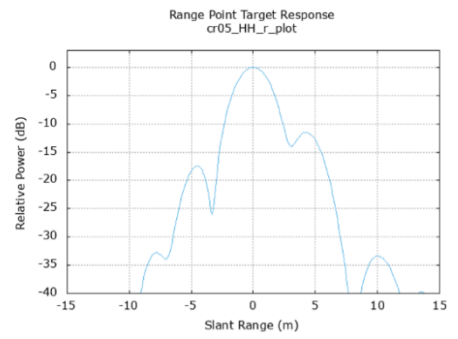
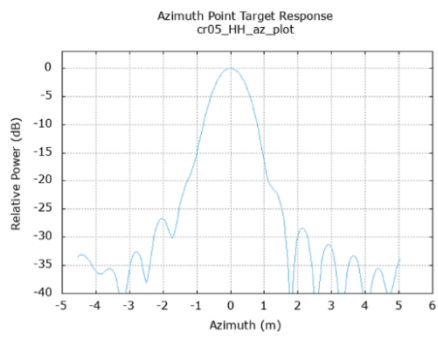
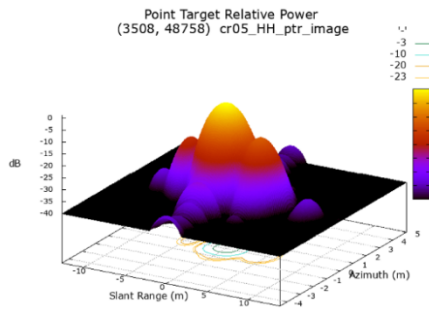
The range and azimuth resolution are estimated from the impulse response function of each corner reflector and their difference from the specified value is calculated and are shown in table 16. The range resolution is found to be 2.69 ± 0.06 meters and azimuth resolution as 0.93 ± 0.02 meters and the difference from the specified value was found to be 0.89 ± 0.06 and 0.93 ± 0.02 for range and azimuth respectively.

6.2.2 Impulse Response Functions for HH polarization



Figure 28: Location of CR's in SLC image of HH pol





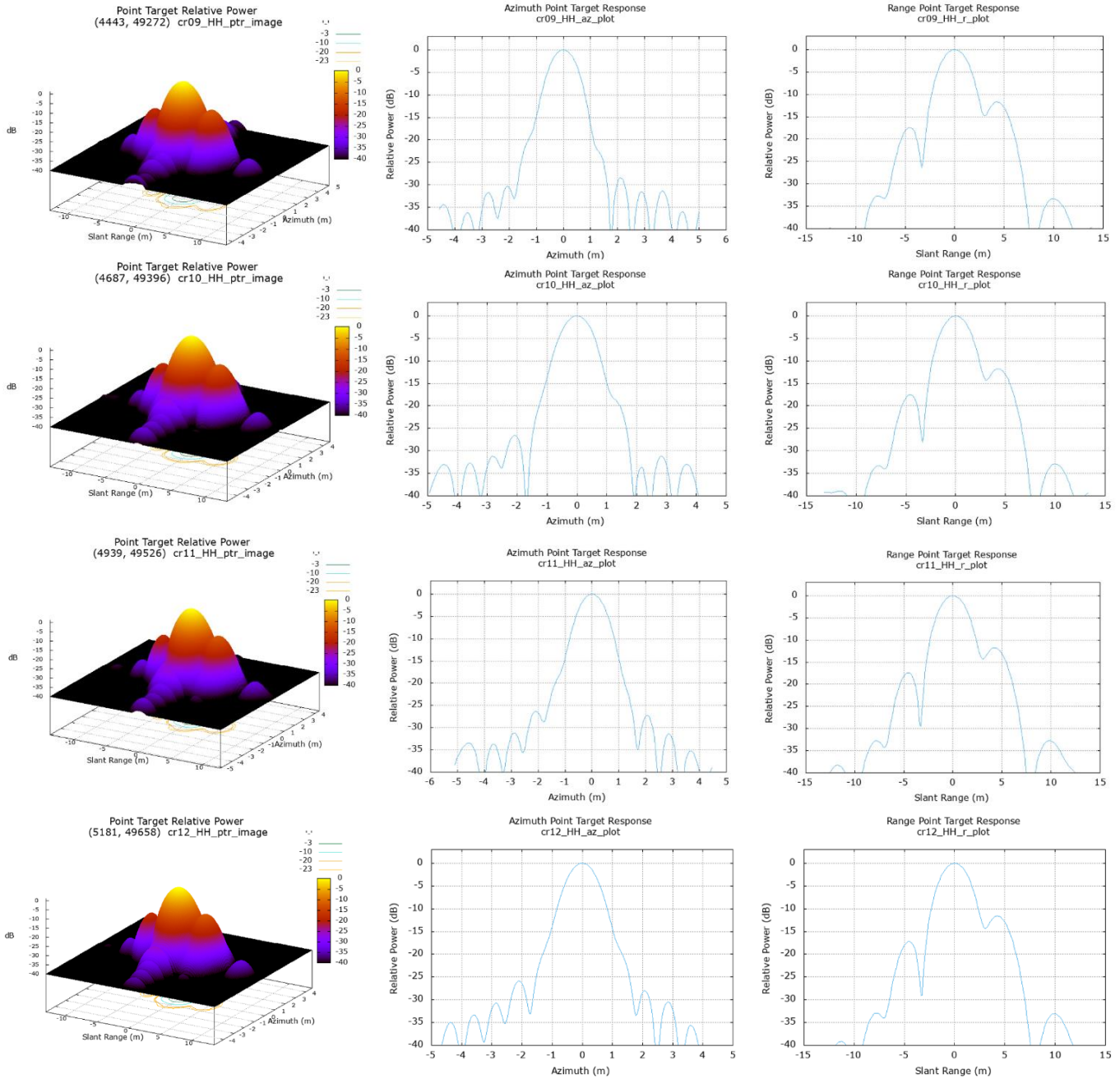
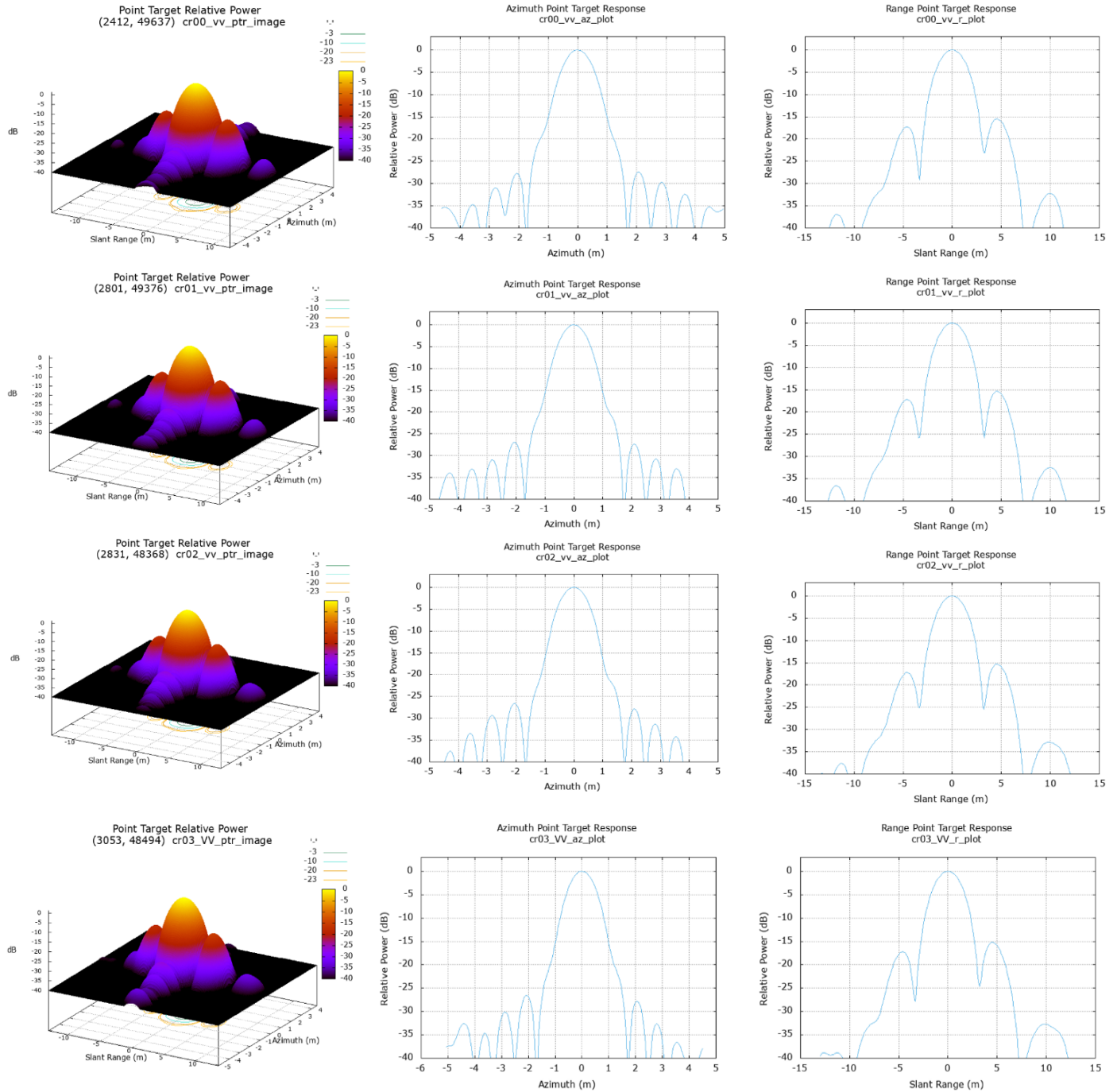
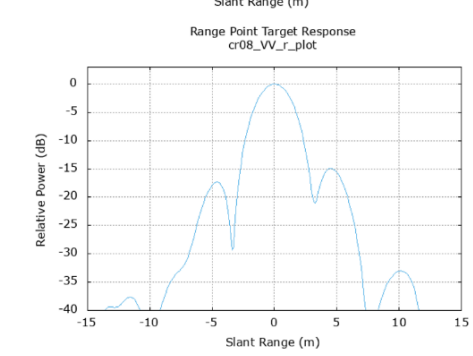
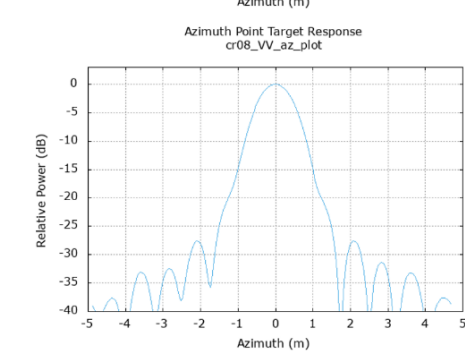
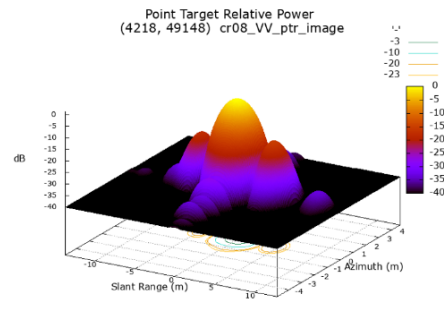
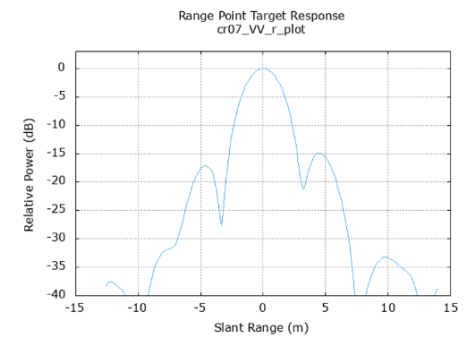
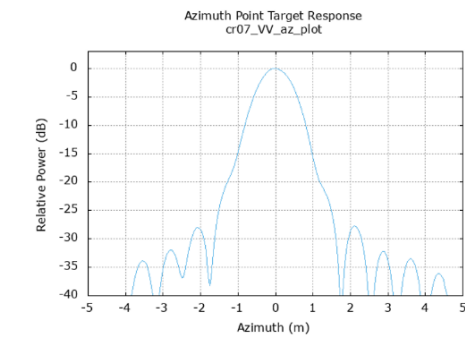
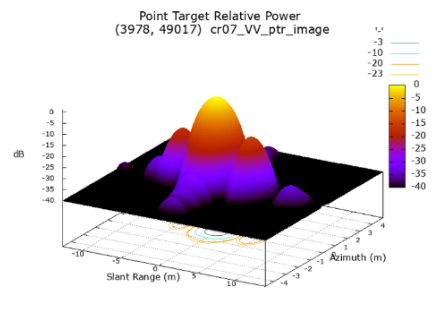
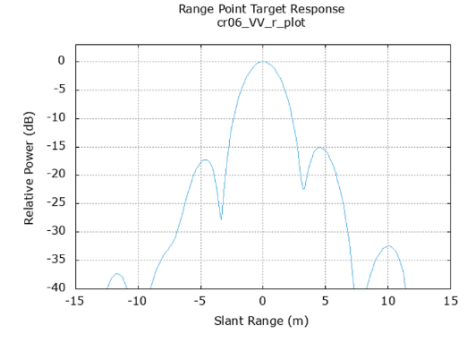
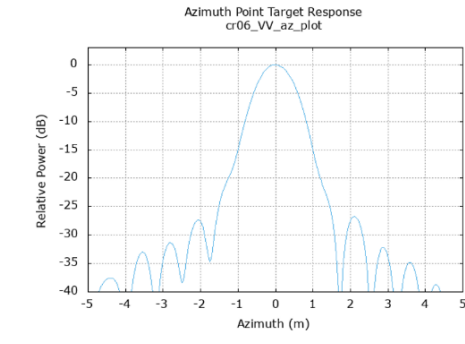
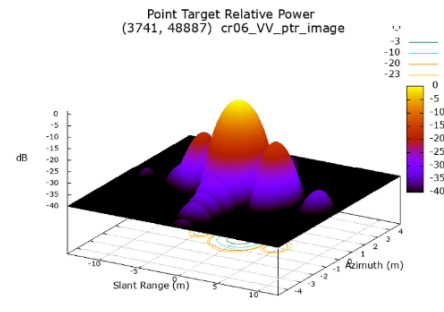
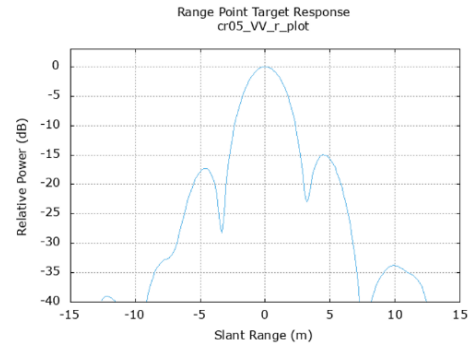
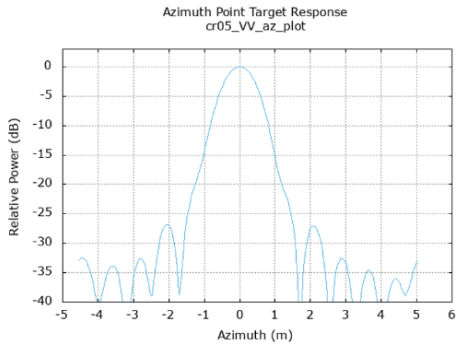
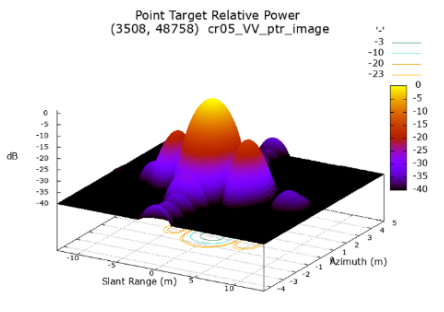
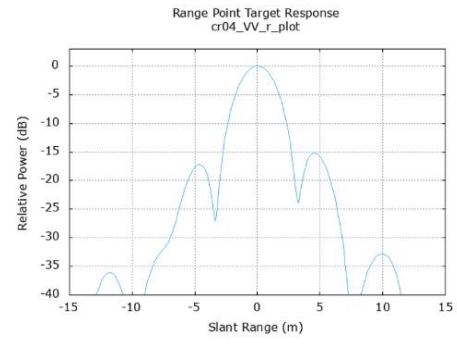
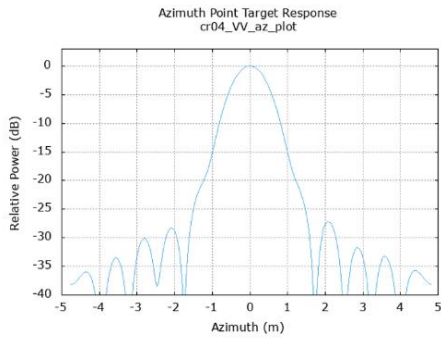
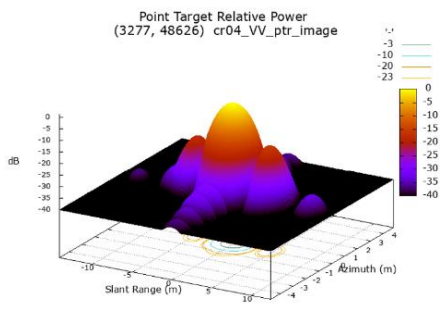


Figure 29: Impulse Response function of CR's using SLC image of HH pol

6.2.3 Impulse Response Functions for VV polarization





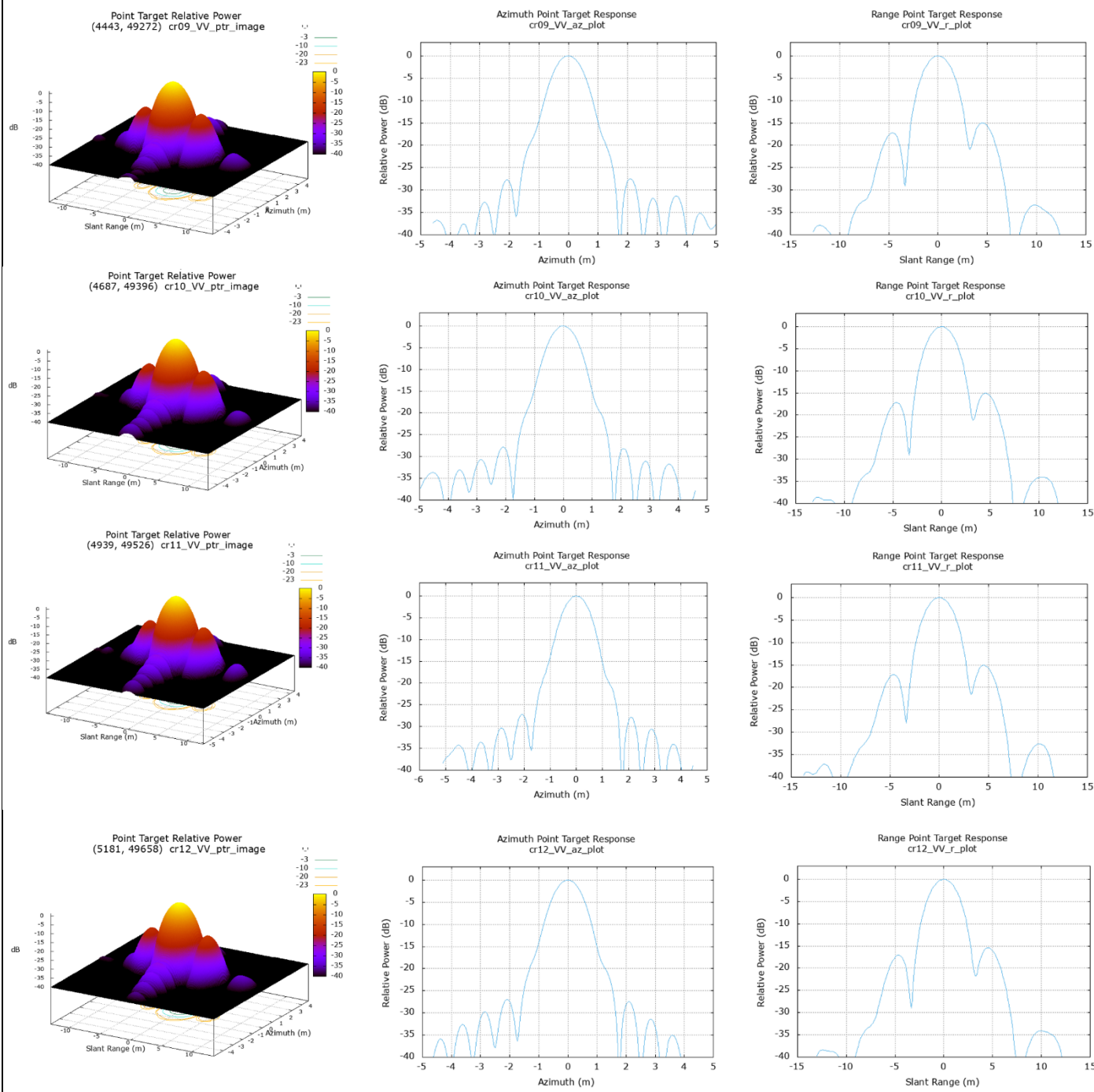


Figure 30: Impulse Response function of CR's using SLC image of VV pol

6.2.4 Channel Imbalance and Phase Bias

Co-channel imbalance (f) for each corner reflector is estimated for HH and VV polarizations using Equation 20 and is given in Table 18. The mean energy value of each target in co-pol channels is considered as the effective value of ' f ', which are pure energy values (without clutter energy) derived for co-polarized channels, as given in mentioned below in Table 20.

Table 17: Calculated Target Energy values after subtraction of clutter for quad pol

| CR | Calculated target energy after subtraction of clutter in VV pol.(linear) | Calculated target energy after subtraction of clutter in HH pol. (linear) | Calculated target energy after subtraction of clutter in HV pol. (linear) | Calculated target energy after subtraction of clutter in VH pol. (linear) |
|-------------|--|---|---|---|
| CR00 | 2158.490 | 2158.580 | 18.735 | 6.823 |
| CR01 | 2079.550 | 2146.040 | 81.108 | 72.689 |
| CR02 | 2062.540 | 2210.050 | 44.210 | 22.612 |
| CR03 | 2370.890 | 2029.640 | 97.339 | 77.731 |
| CR04 | 1918.820 | 1854.290 | 12.140 | 13.374 |
| CR05 | 1934.090 | 2193.250 | 59.399 | 30.442 |
| CR06 | 1828.900 | 2221.110 | 19.363 | 5.970 |
| CR07 | 1621.150 | 1920.410 | 30.010 | 15.669 |
| CR08 | 1862.400 | 2106.120 | 18.984 | 6.530 |
| CR09 | 1548.860 | 1645.380 | 22.868 | 12.513 |
| CR10 | 1761.160 | 1671.560 | 44.520 | 26.256 |
| CR11 | 1964.110 | 1950.120 | 27.016 | 52.985 |
| CR12 | 2003.340 | 1797.610 | 58.701 | 70.584 |

Table 18: Estimation of co channel imbalance (f)

| CR_id | Cal. Target energy after substr. Of clutter in VV (in linear) | Cal. Target energy after substr. Of clutter in HH (in linear) | square root of VV (in linear) | square root of HH (in linear) | Co-pol channel imbalance in linear (f) |
|-------|---|---|-------------------------------|-------------------------------|--|
| CR00 | 2158.490 | 2158.580 | 46.45955 | 46.46052 | 0.999979 |
| CR01 | 2079.550 | 2146.040 | 45.60208 | 46.32537 | 0.984387 |
| CR02 | 2062.540 | 2210.050 | 45.4152 | 47.01117 | 0.966051 |
| CR03 | 2370.890 | 2029.640 | 48.69179 | 45.05153 | 1.080802 |
| CR04 | 1918.820 | 1854.290 | 43.80434 | 43.06147 | 1.017251 |
| CR05 | 1934.090 | 2193.250 | 43.97829 | 46.83215 | 0.939062 |
| CR06 | 1828.900 | 2221.110 | 42.76564 | 47.12865 | 0.907423 |
| CR07 | 1621.150 | 1920.410 | 40.26351 | 43.82248 | 0.918787 |
| CR08 | 1862.400 | 2106.120 | 43.15553 | 45.89248 | 0.940362 |
| CR09 | 1548.860 | 1645.380 | 39.35556 | 40.56328 | 0.970226 |
| CR10 | 1761.160 | 1671.560 | 41.96618 | 40.88472 | 1.026451 |
| CR11 | 1964.110 | 1950.120 | 44.31828 | 44.16016 | 1.003581 |
| CR12 | 2003.340 | 1797.610 | 44.75869 | 42.39823 | 1.055673 |
| | | | <i>Mean f in linear</i> | | 0.985387 |

Cross channel imbalance (g) is the difference between energy of a featureless homogenous patch estimated for HV and VH polarizations Equation 22 and Equation 20. The estimated cross-channel imbalance (g) values are given by Table 19.

Table 19: Estimation of cross channel imbalance (g)

| Values derived from SLC image using ENVI software | HV | VH |
|---|------------------------|-------------|
| Real | 0.000011 | 0.000008 |
| Imaginary | 0.000026 | 0.000021 |
| Amplitude (dB) | 0.00002823119 | 0.000022472 |
| Phase (dB) | 1.17055567 | 1.20681737 |
| <i>g (dB)</i> | <i>1.256271</i> | |

Phase anomaly between co-channels of HH and VV polarization at each of the corner reflector $\phi_t + \phi_r$ is estimated. The phase bias of co-channel ϕ_s is estimated on each corner reflector using equation 21. While for phase anomaly between cross channels –HV and VH $\phi_t - \phi_r$ of featureless homogenous patch is estimated using equation 23 and given by ϕ_d . The phase bias of co-channel and cross channel are estimated from ϕ_s and ϕ_d which are mentioned in table 20.

Table 20: Estimated Phase bias in transmitter and receiver for co-pol and cross-pol channels

| | In radians | In degrees |
|----------|------------|------------|
| Φ_d | -0.03626 | -2.077642 |
| Φ_s | 0.027547 | 1.578333 |
| Φ_t | -0.00436 | -0.249655 |
| Φ_r | 0.031904 | 1.827988 |

6.2.5 Polarimetric signatures after radiometric and phase correction

The radiometric and phase calibration correction has already applied for the dataset. Before radiometric and phase calibration, the polarization signatures have double peaked nature due to 180° phase offset between the HH and VV channels. The polarization signatures generated after radiometric and phase corrected dataset is shown in Figure 31 (Alexander, Bruce and Brian 2014). After correction the shapes of the polarimetric signatures at the corner reflector pixels should closely resemble the ideal shapes as shown in Figure 31 and signatures generated from the dataset used in study are shown in Figure 32.

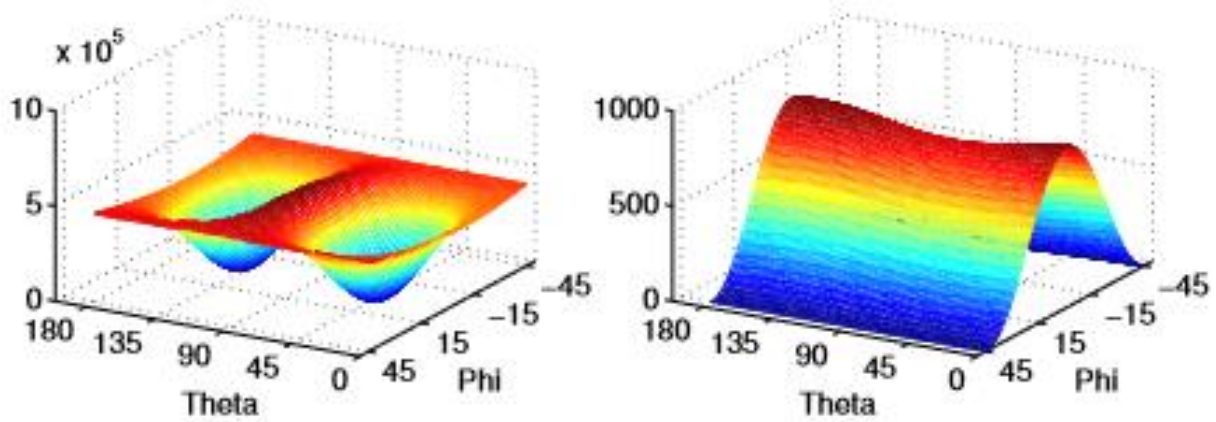


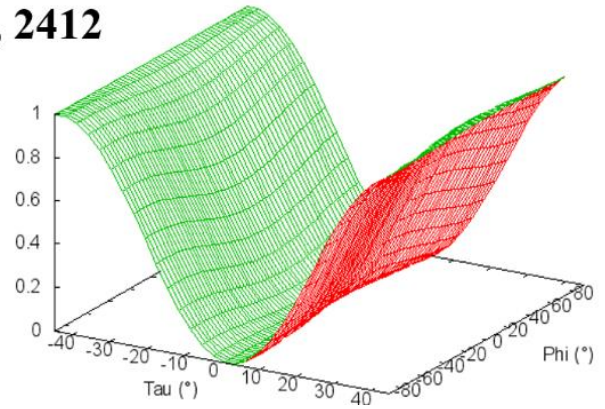
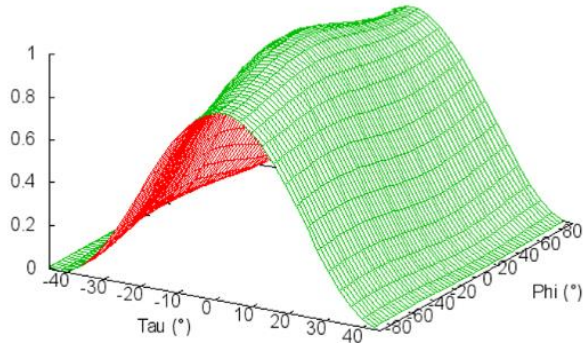
Figure 31: Polarimetric Signature of corner reflector in ideal case: Co-polarization signature of corner reflector before (after) radiometric and phase calibration shown in left (right) panel. ©(Alexander, Bruce and Brian 2014)

6.2.6 Polarimetric signatures of each CR

Normalized Polarimetric Signature : Co-polarisation channel

Normalized Polarimetric Signature : Cross-polarisation channel

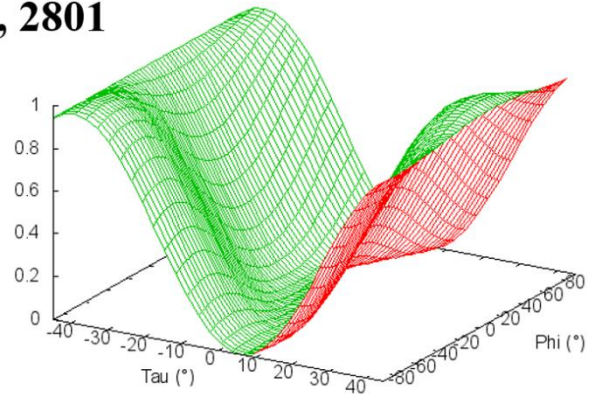
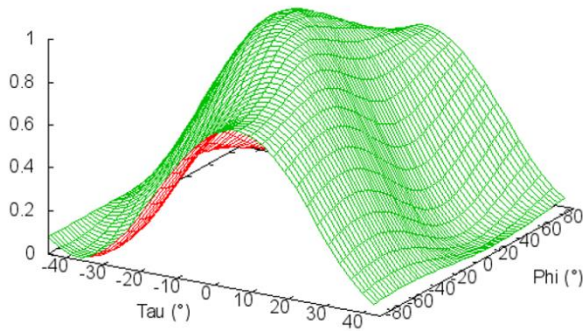
CR00: 49637, 2412



Normalized Polarimetric Signature : Co-polarisation channel

Normalized Polarimetric Signature : Cross-polarisation channel

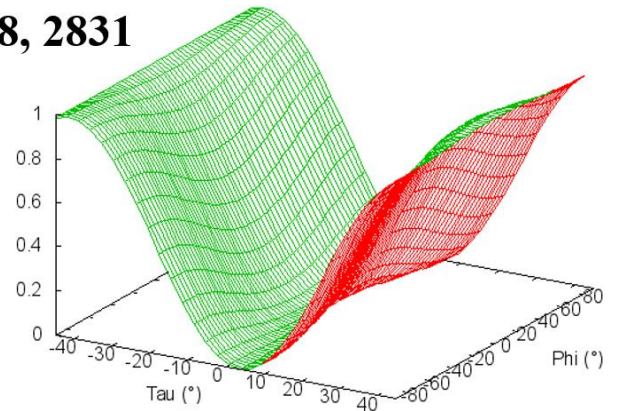
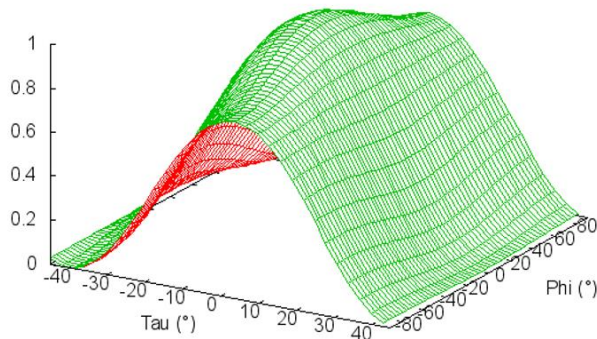
CR01: 49376, 2801



Normalized Polarimetric Signature : Co-polarisation channel

Normalized Polarimetric Signature : Cross-polarisation channel

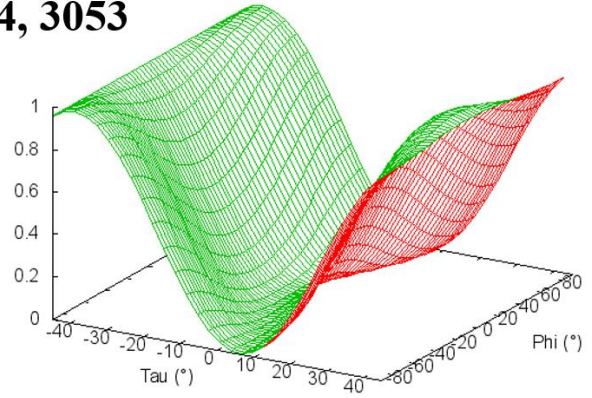
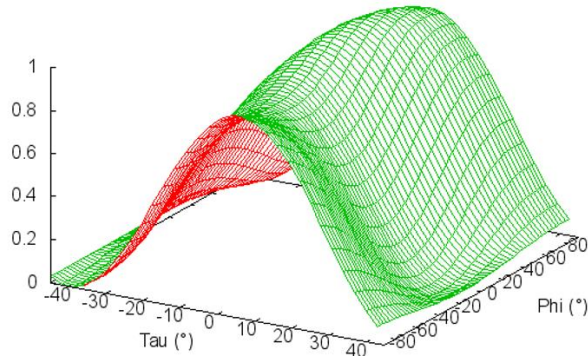
CR02: 48368, 2831



Normalized Polarimetric Signature : Co-polarisation channel

Normalized Polarimetric Signature : Cross-polarisation channel

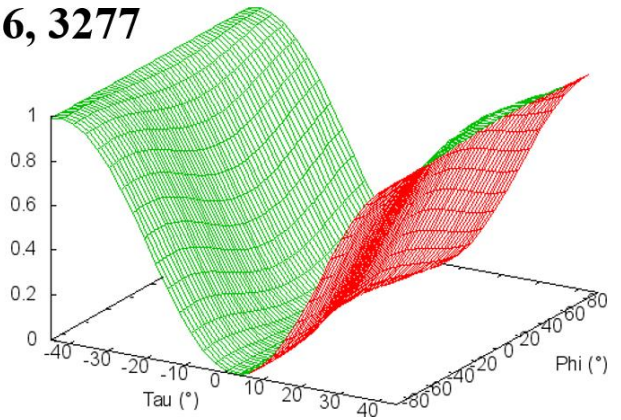
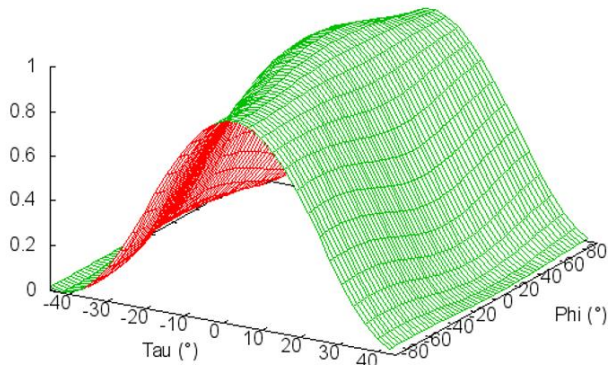
CR03: 48494, 3053



Normalized Polarimetric Signature : Co-polarisation channel

Normalized Polarimetric Signature : Cross-polarisation channel

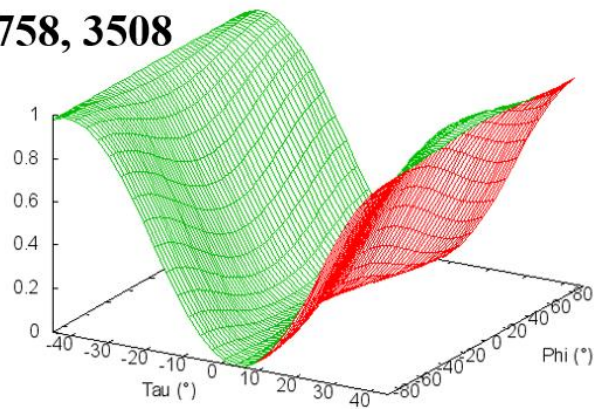
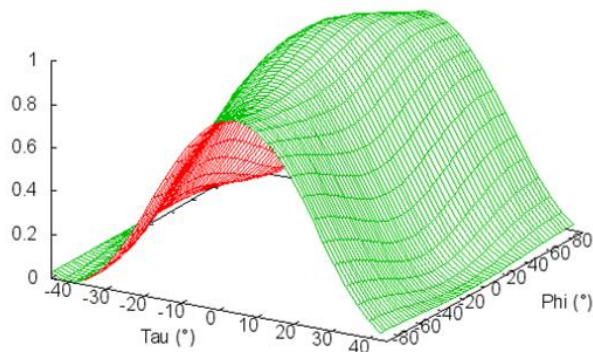
CR04: 48626, 3277



Normalized Polarimetric Signature : Co-polarisation channel

Normalized Polarimetric Signature : Cross-polarisation channel

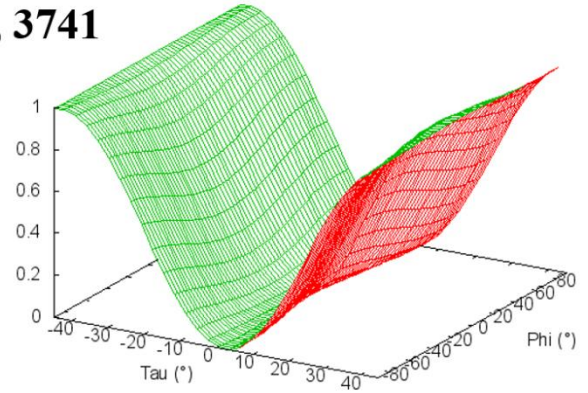
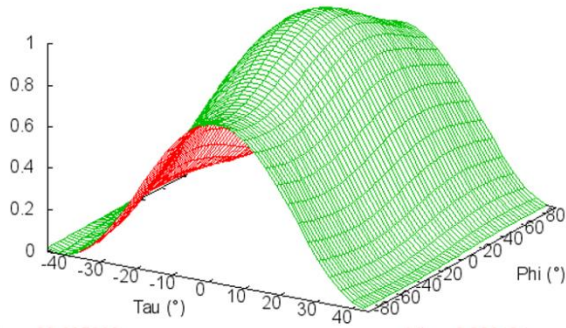
CR05: 48758, 3508



Normalized Polarimetric Signature : Co-polarisation channel

Normalized Polarimetric Signature : Cross-polarisation channel

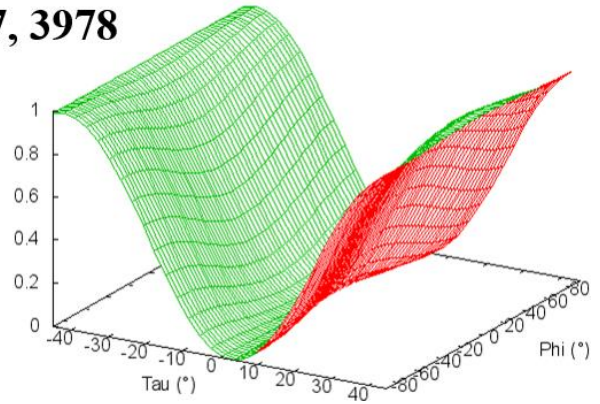
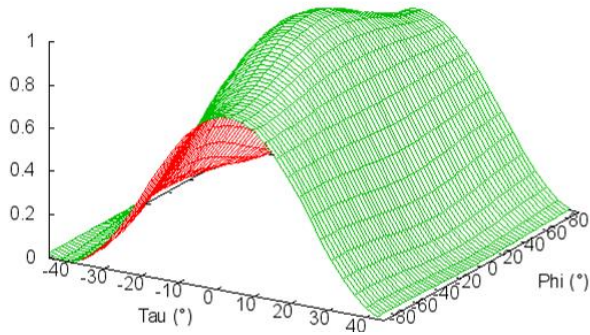
CR06: 48887, 3741



Normalized Polarimetric Signature : Co-polarisation channel

Normalized Polarimetric Signature : Cross-polarisation channel

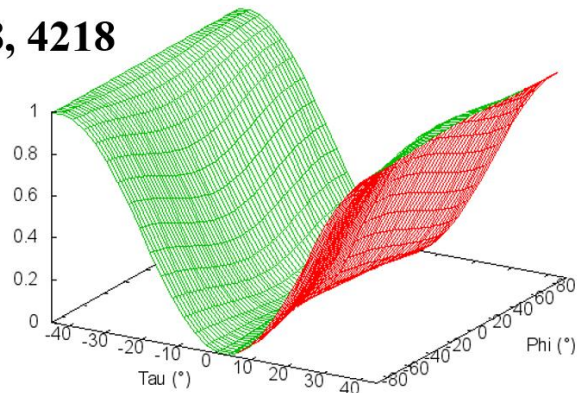
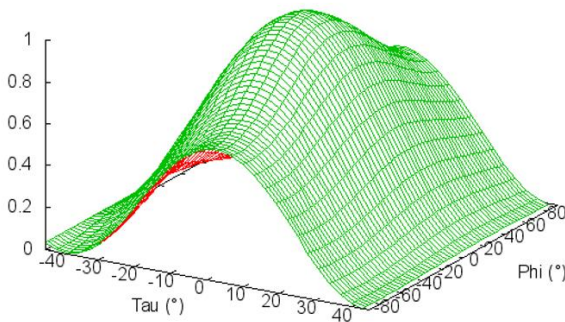
CR07: 49017, 3978



Normalized Polarimetric Signature : Co-polarisation channel

Normalized Polarimetric Signature : Cross-polarisation channel

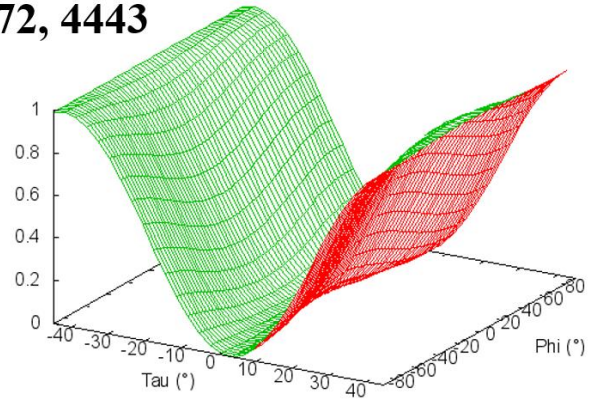
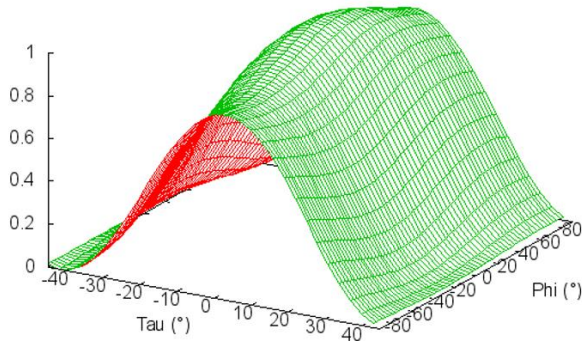
CR08: 49148, 4218



Normalized Polarimetric Signature : Co-polarisation channel

Normalized Polarimetric Signature : Cross-polarisation channel

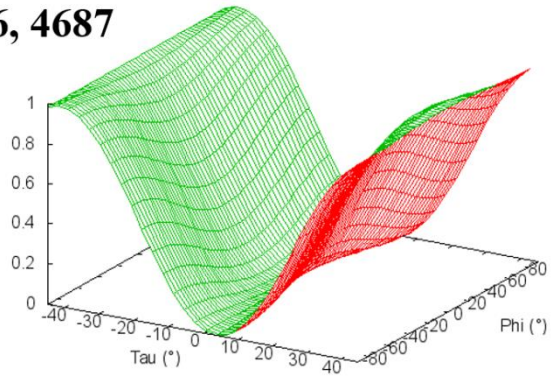
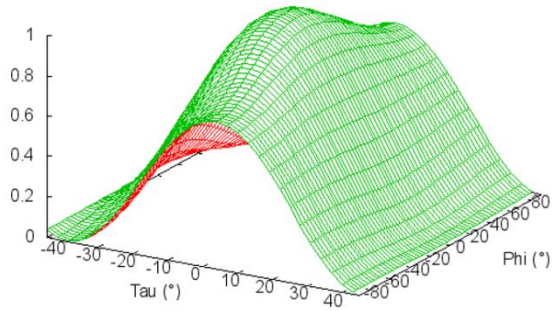
CR09: 49272, 4443



Normalized Polarimetric Signature : Co-polarisation channel

Normalized Polarimetric Signature : Cross-polarisation channel

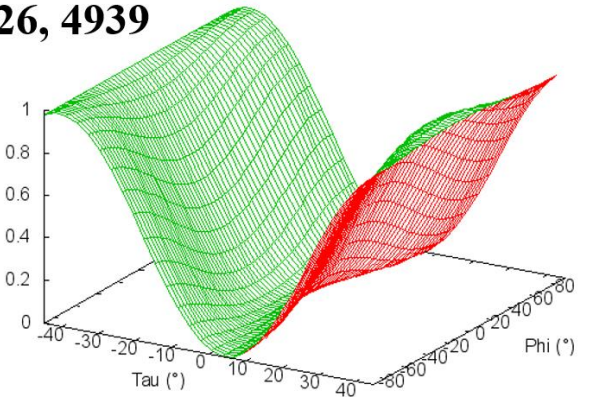
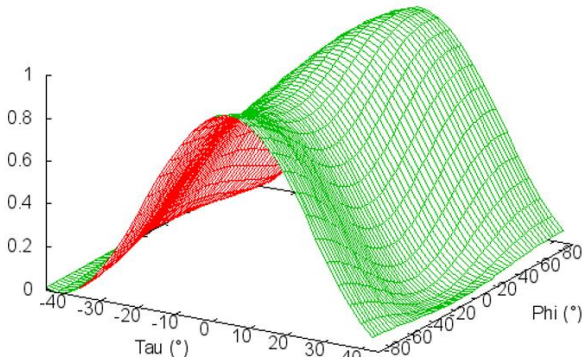
CR10: 49396, 4687



Normalized Polarimetric Signature : Co-polarisation channel

Normalized Polarimetric Signature : Cross-polarisation channel

CR11: 49526, 4939



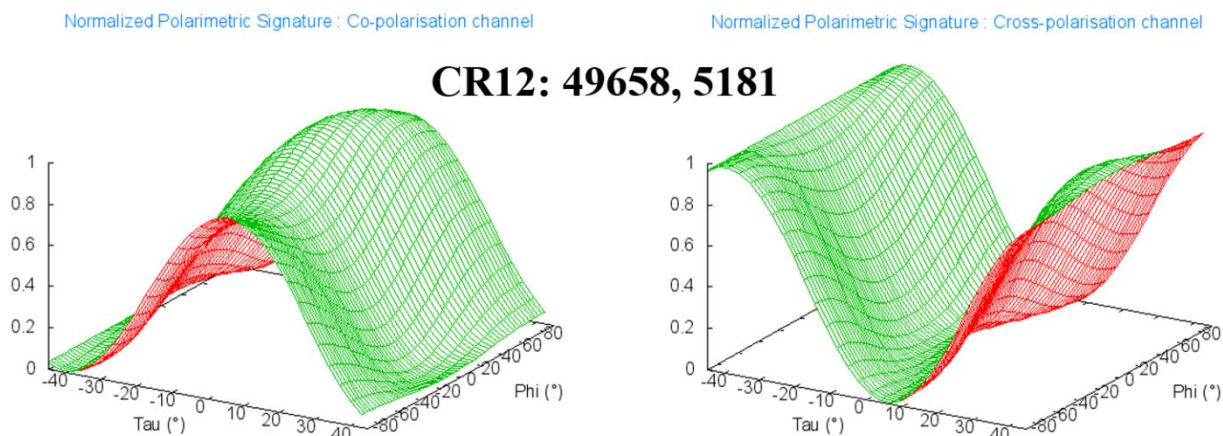


Figure 32: Polarimetric Signatures of Triangular Trihedral Corner Reflector after Radiometric and Phase Calibration.

The polarimetric signatures of the 2.4 m corner reflectors are shown in above Figure 32, which closely depict the ideal shape of the triangular trihedral corner reflector. The phase offset is reasonable and even though there are some visible distortions in the co-pol and cross-pol signatures generated for the corner reflector, the distortions are not high. Therefore, the dataset is radiometrically calibrated and the presence of phase bias is negligible.

Polarization Parameters

Following the above methodology the SLC data that are radiometrically and phase calibrated. This dataset contains residual cross talks and channel imbalances of the polarization channels. This partial calibrated dataset is used as the input for polarimetric correction. This correction excludes cross talk calibration while maintaining radiometric and phase calibration.

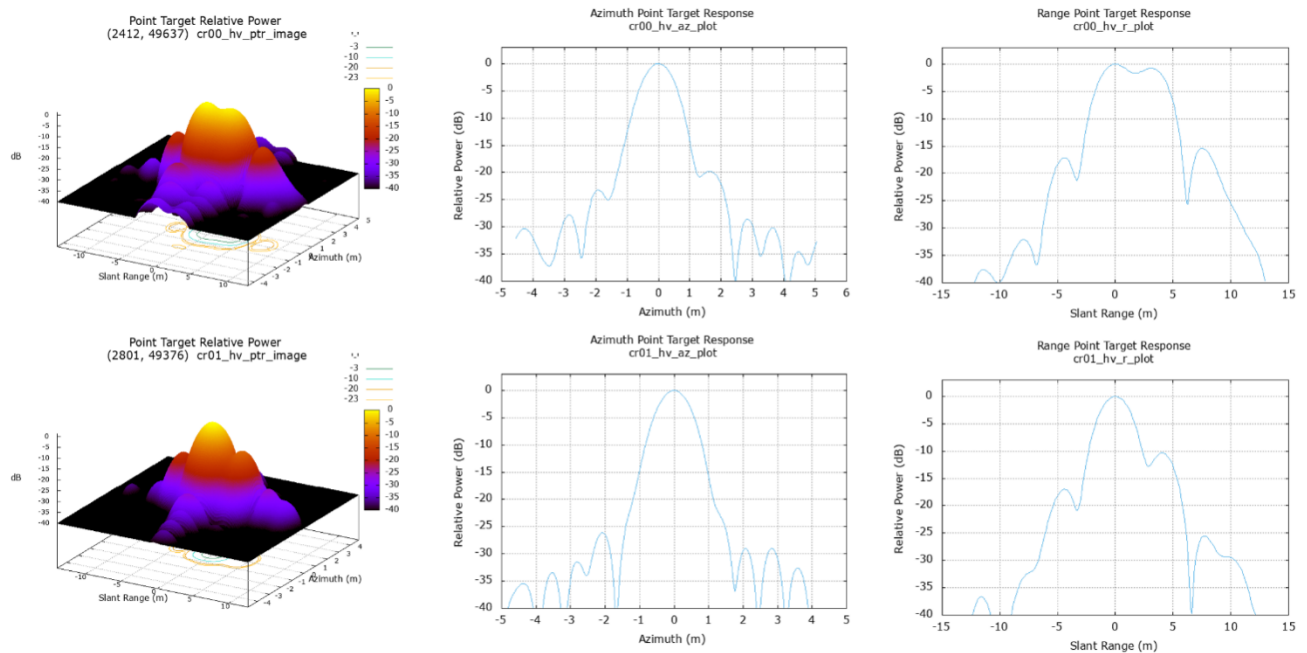
6.3.1 Impulse Response Function for HV polarization

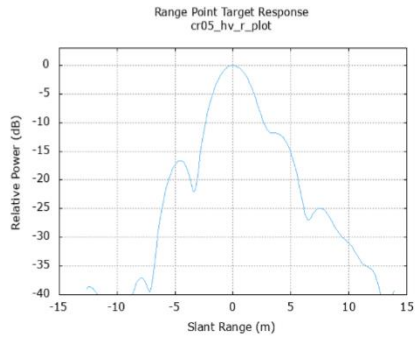
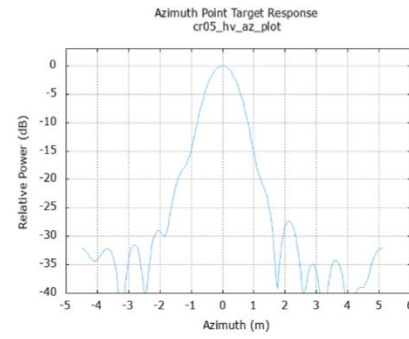
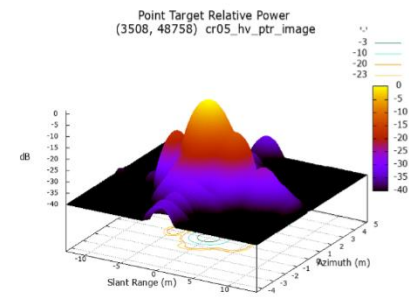
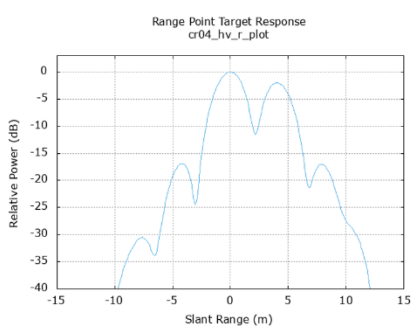
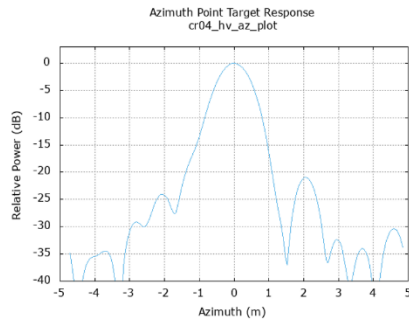
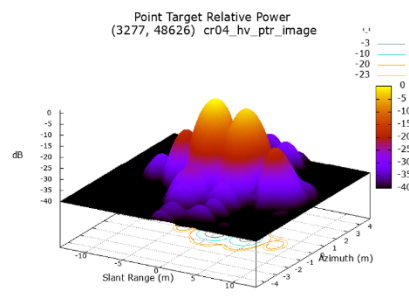
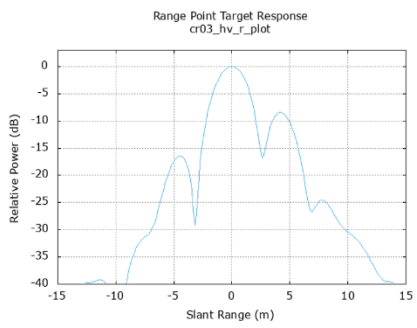
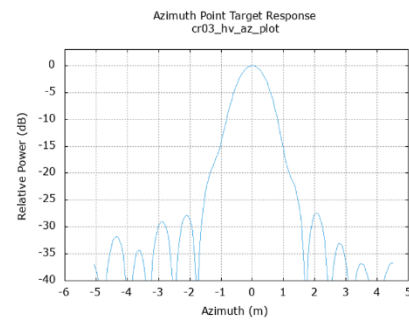
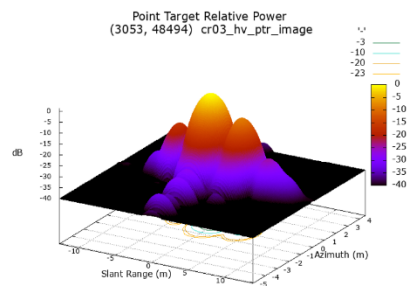
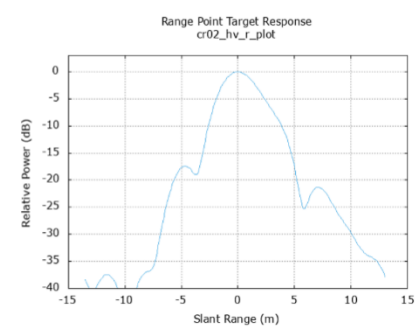
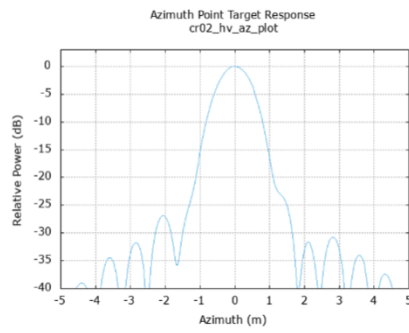
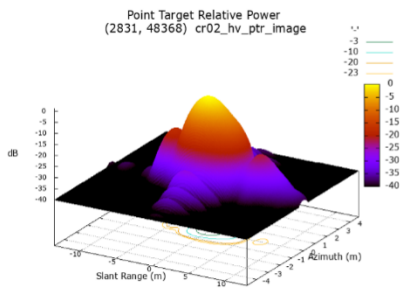
The well cross talk calibrated dataset shouldn't have target energy in cross polarized channels. But in this dataset the presence of corner reflectors is clearly visible in the SLC image of cross polarized data as shown below in Figure 33. This is also due to cross talks and channels imbalance errors. Hence cross talk and channel imbalance correction is required for this dataset.

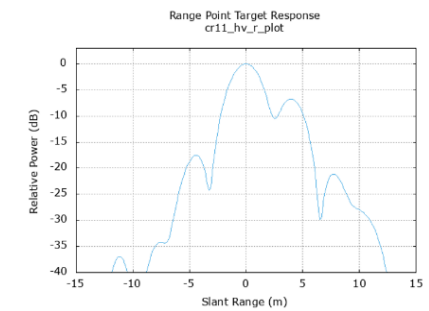
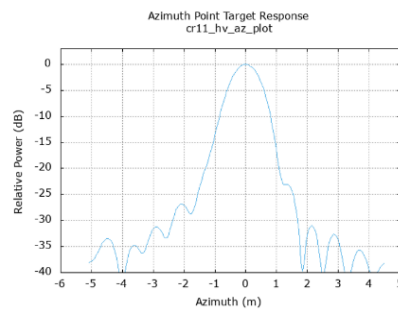
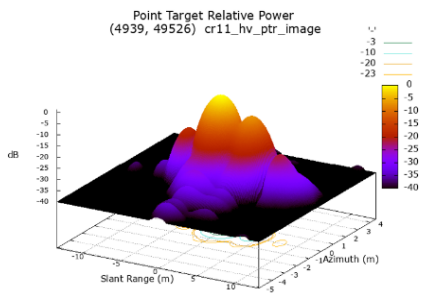
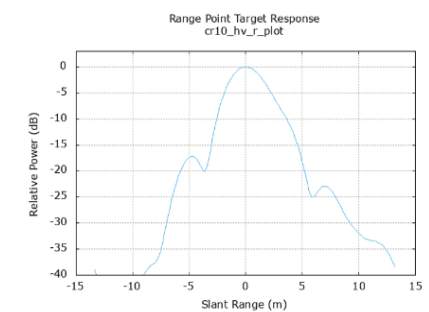
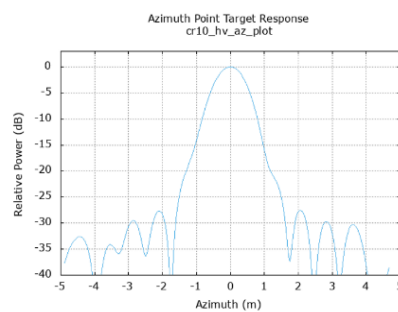
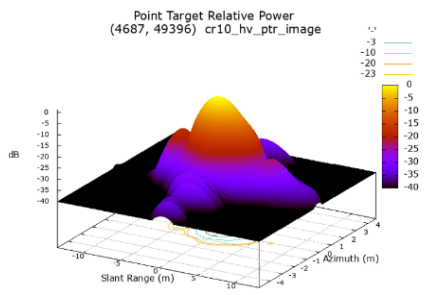
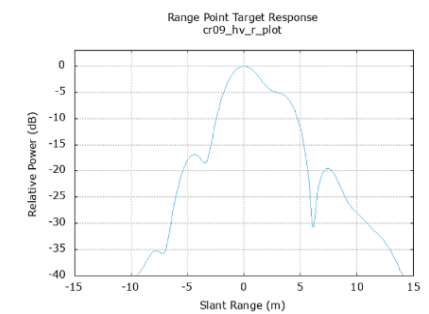
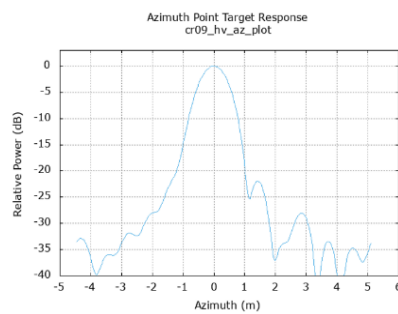
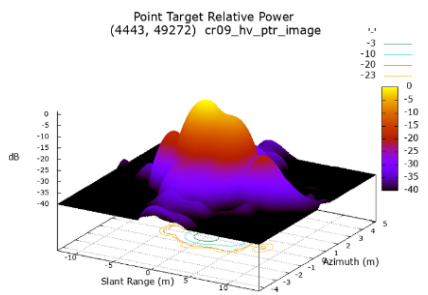
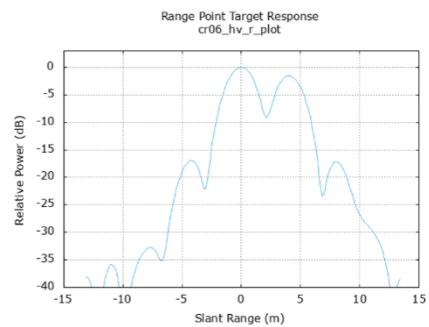
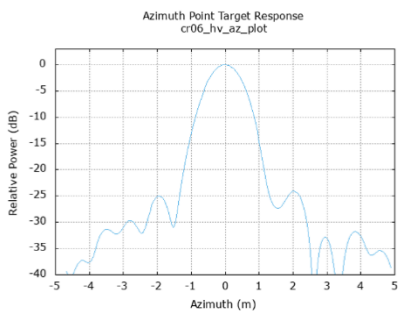
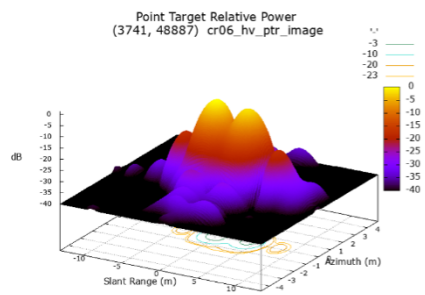
The impulse response for each corner reflector which are generated in cross-pol channel (HV) is shown in Figure 34.



Figure 33: Location of CR's in SLC image of HV pol







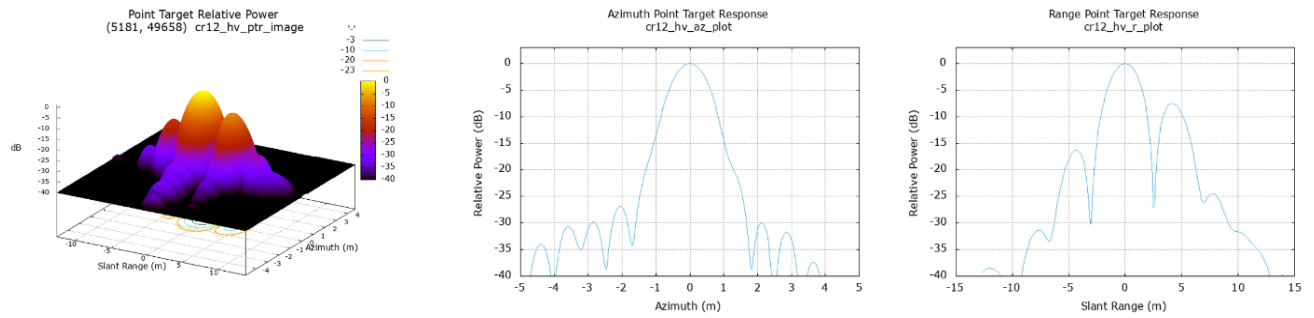


Figure 34: Impulse Response of CR using SLC image of HV

6.3.2 Estimation of cross talk and channel imbalance by Quegan's Method

Using Quegan algorithm the following cross talk and channels imbalance parameters are estimated with the procedure mentioned in the above section. The estimated cross talk and channel imbalances for dataset in given in the Table 21 and its contains absolute amplitude values in linear form.

Table 21: Estimation of cross talk and channel imbalance using Quegan algorithm

| | u_abs (linear) | v_abs (linear) | z_abs (linear) | w_abs (linear) | alpha_abs (linear) |
|------|----------------|----------------|----------------|----------------|--------------------|
| CR00 | 2.2547 | 4.7745 | 2.9872 | 5.7732 | 0.7884 |
| CR01 | 0.5634 | 1.2853 | 0.4756 | 1.1738 | 1.461 |
| CR02 | 0.5246 | 1.1457 | 3.2758 | 5.5407 | 0.1754 |
| CR03 | 0.4214 | 1.6154 | 0.2978 | 0.8121 | 3.2765 |
| CR04 | 0.2088 | 0.4691 | 0.6816 | 1.9522 | 0.3553 |
| CR05 | 0.9832 | 0.6207 | 0.3574 | 0.3387 | 0.8972 |
| CR06 | 0.1394 | 0.6383 | 0.073 | 0.9152 | 0.9781 |
| CR07 | 1.9697 | 1.9171 | 2.6269 | 2.6188 | 0.754 |
| CR08 | 0.0019 | 0.9061 | 0.0011 | 0.3821 | 1 |
| CR09 | 4.5734 | 4.4968 | 4.6416 | 4.4497 | 1.0103 |
| CR10 | 0.1707 | 0.3853 | 0.1106 | 0.3303 | 1 |
| CR11 | 0.0158 | 0.1181 | 5.16E-06 | 0.4141 | 219.049 |
| CR12 | 0.2365 | 0.333 | 2.4281 | 2.5775 | 0.4084 |

6.3.3 Polarimetric Signatures- GRD Data

Polarimetric signatures are generated for the same study area dry lake, Rosamond using ground range detected (GRD) of quad polarization data. The covariance matrix of 3x3 is used to generate the signatures which is radiometric and polarimetric corrected dataset. The ideal polarimetric signature of the corner reflector for co-pol and cross-pol channel is shown in Figure 35, the estimated signatures in this section should match with ideal case.

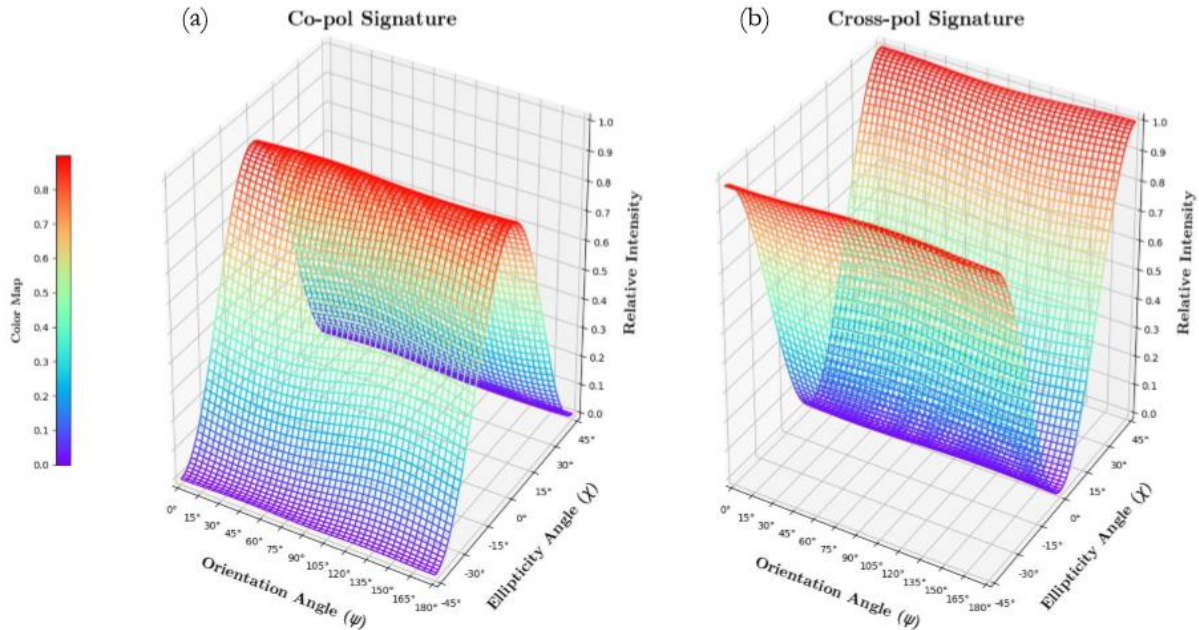
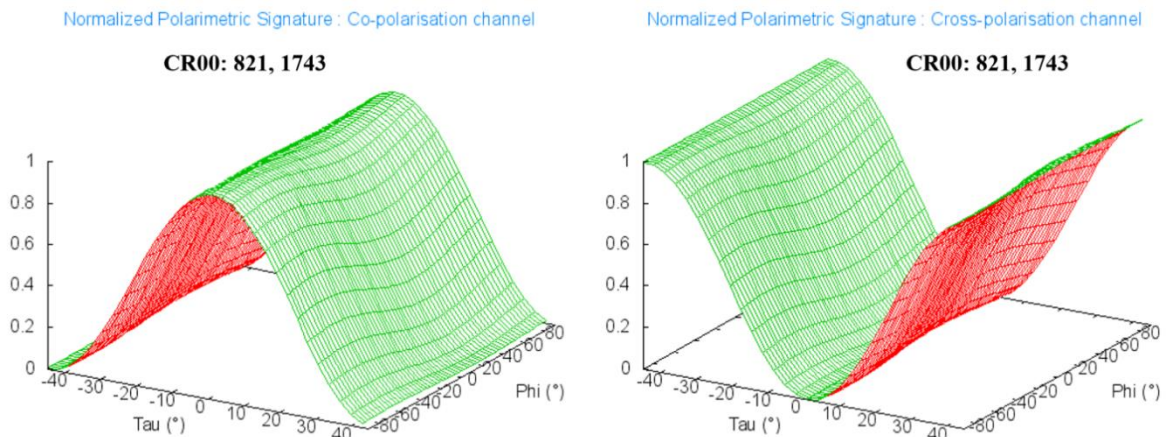


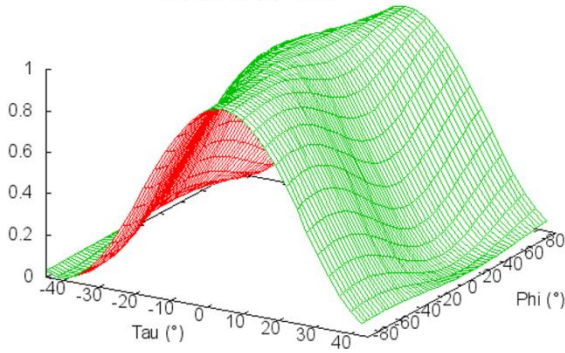
Figure 35: Polarimetric signature of triangular trihedral corner reflector (ideal case) © (Abhisek, Shashi and Valentyn 2019).

Polarimetric signature of triangular trihedral corner reflector



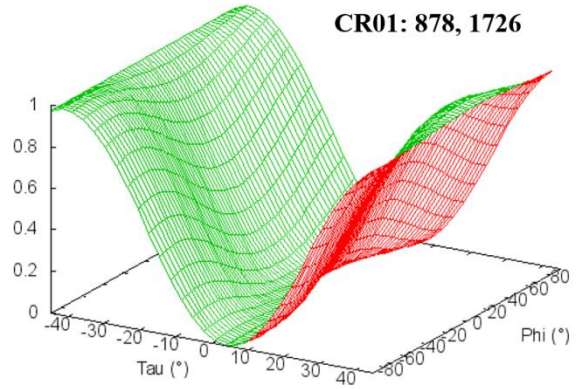
Normalized Polarimetric Signature : Co-polarisation channel

CR01: 878, 1726



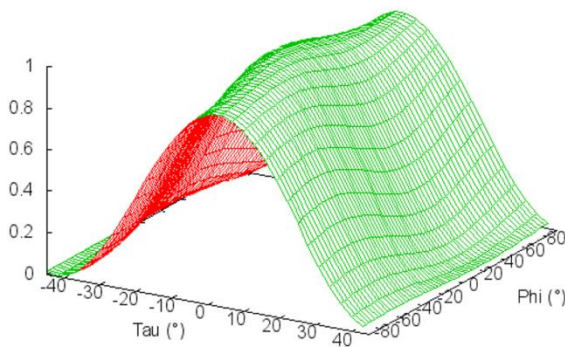
Normalized Polarimetric Signature : Cross-polarisation channel

CR01: 878, 1726



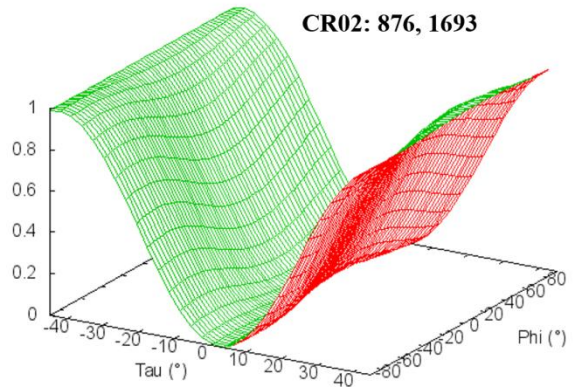
Normalized Polarimetric Signature : Co-polarisation channel

CR02: 876, 1693



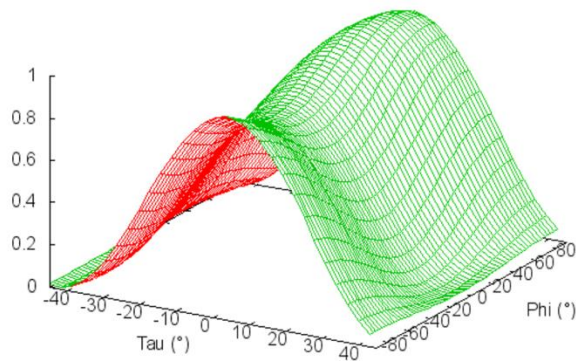
Normalized Polarimetric Signature : Cross-polarisation channel

CR02: 876, 1693



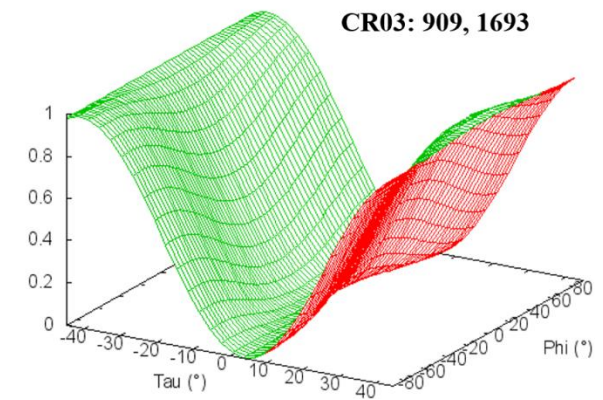
Normalized Polarimetric Signature : Co-polarisation channel

CR03: 909, 1693



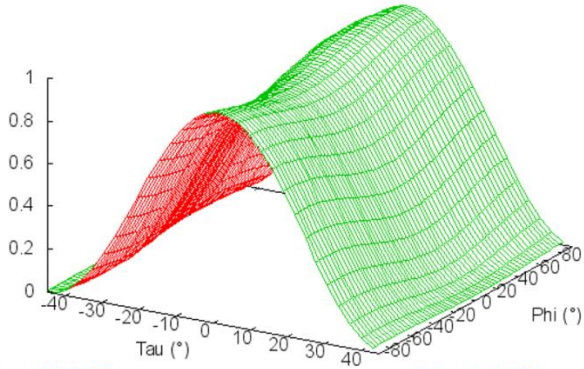
Normalized Polarimetric Signature : Cross-polarisation channel

CR03: 909, 1693



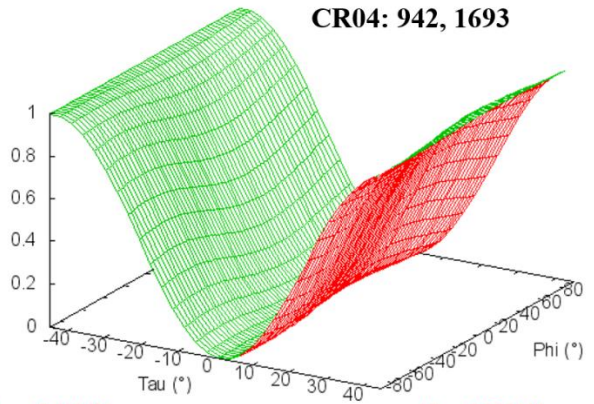
Normalized Polarimetric Signature : Co-polarisation channel

CR04: 942, 1693



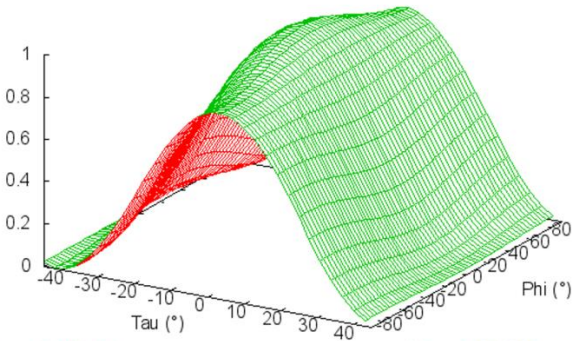
Normalized Polarimetric Signature : Cross-polarisation channel

CR04: 942, 1693



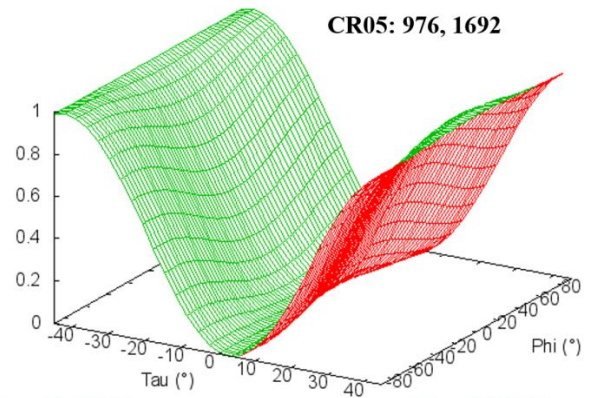
Normalized Polarimetric Signature : Co-polarisation channel

CR05: 976, 1692



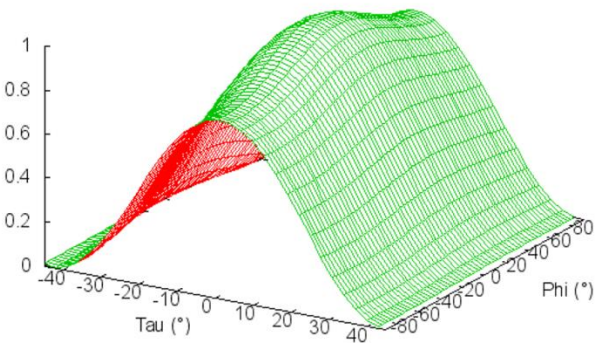
Normalized Polarimetric Signature : Cross-polarisation channel

CR05: 976, 1692



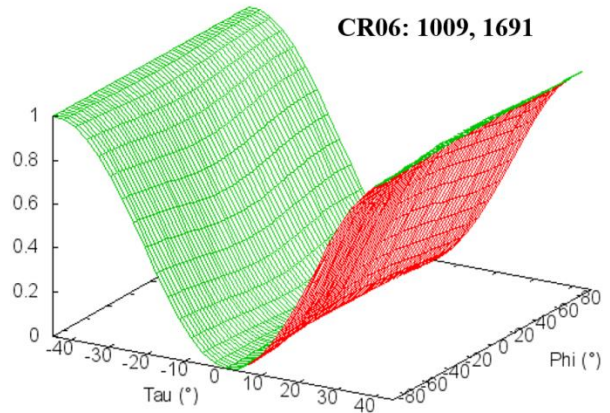
Normalized Polarimetric Signature : Co-polarisation channel

CR06: 1009, 1691



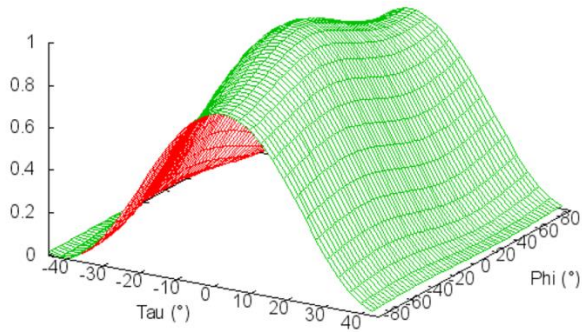
Normalized Polarimetric Signature : Cross-polarisation channel

CR06: 1009, 1691



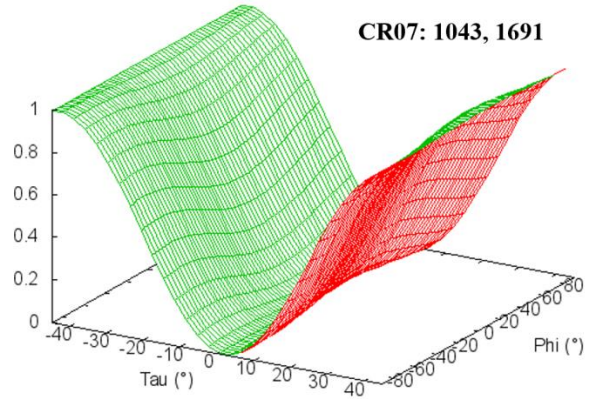
Normalized Polarimetric Signature : Co-polarisation channel

CR07: 1043, 1691



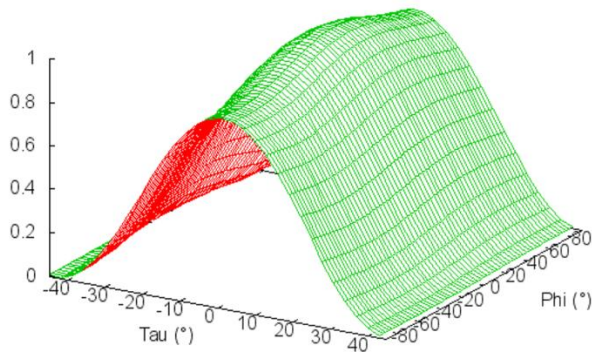
Normalized Polarimetric Signature : Cross-polarisation channel

CR07: 1043, 1691



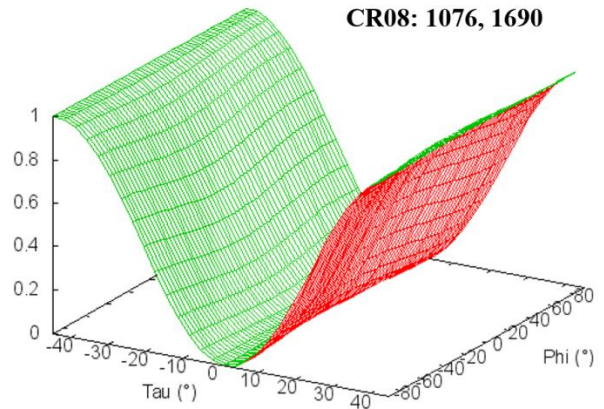
Normalized Polarimetric Signature : Co-polarisation channel

CR08: 1076, 1690



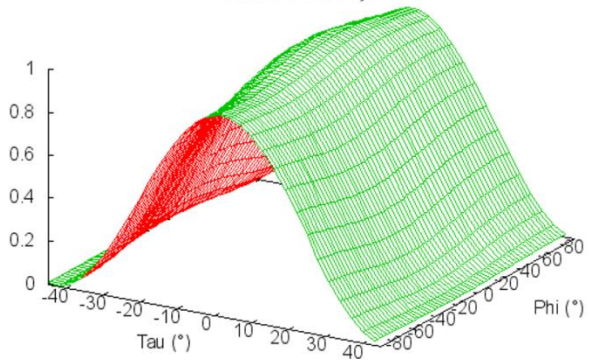
Normalized Polarimetric Signature : Cross-polarisation channel

CR08: 1076, 1690



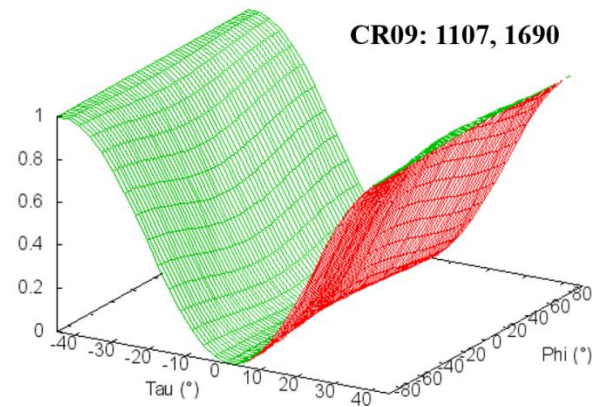
Normalized Polarimetric Signature : Co-polarisation channel

CR09: 1107, 1690



Normalized Polarimetric Signature : Cross-polarisation channel

CR09: 1107, 1690



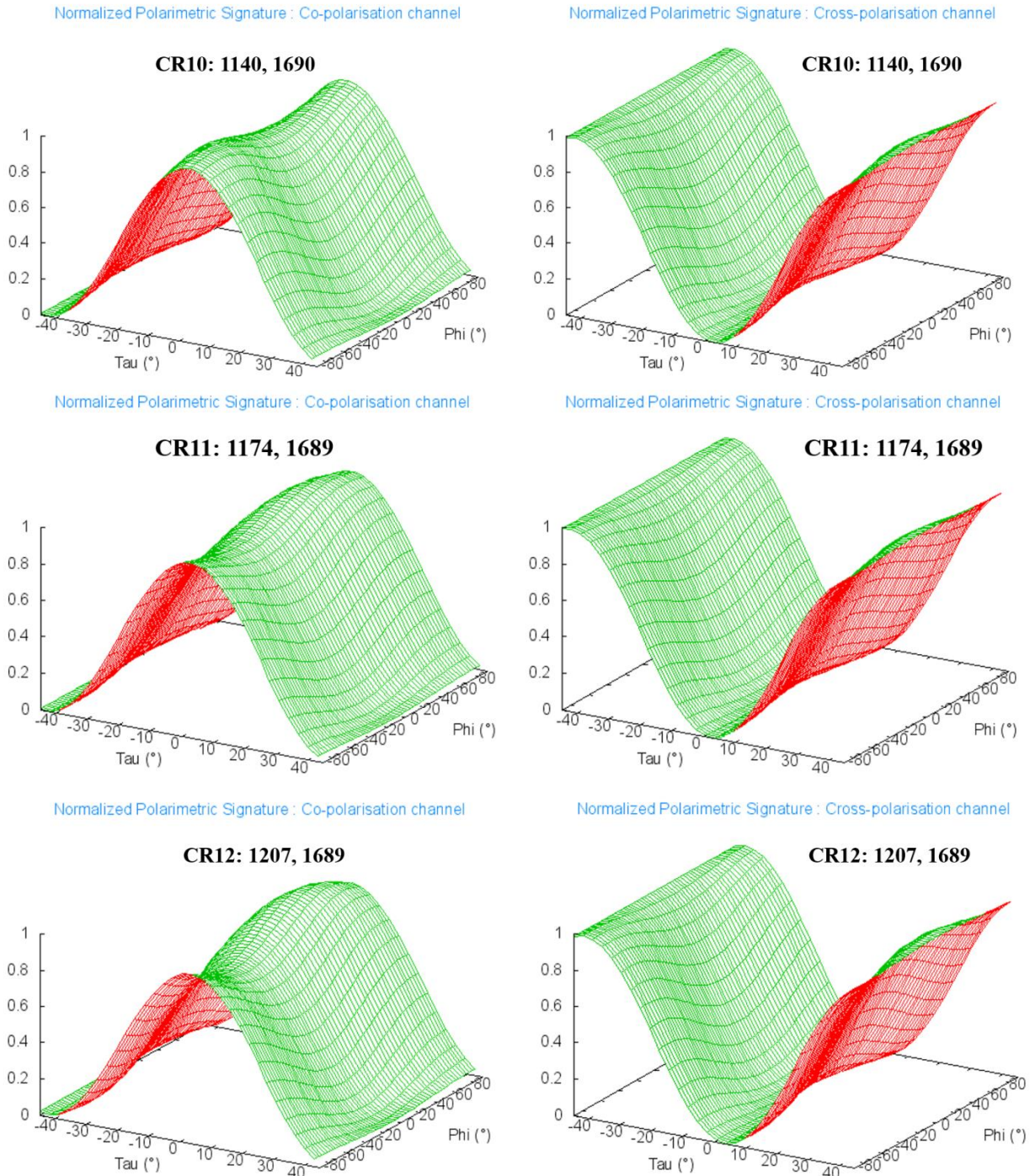


Figure 36: Polarimetric signatures of each CR after cross talk and channel imbalance calibration

The GRD dataset used for polarimetric signature generation has cross talk and channel imbalances correction (information provided by data site) i.e., no channel imbalance and cross talk error. The above generated polarimetric signatures are similar to the ideal signature and it is

observed that the distortions present in polarimetric signatures are acceptable, which proves that dataset's can be used. Similarly, for SLC data has to be generated.

6.3.4 Opportunistic Targets- Windmills present in the UAVSAR L band SLC data

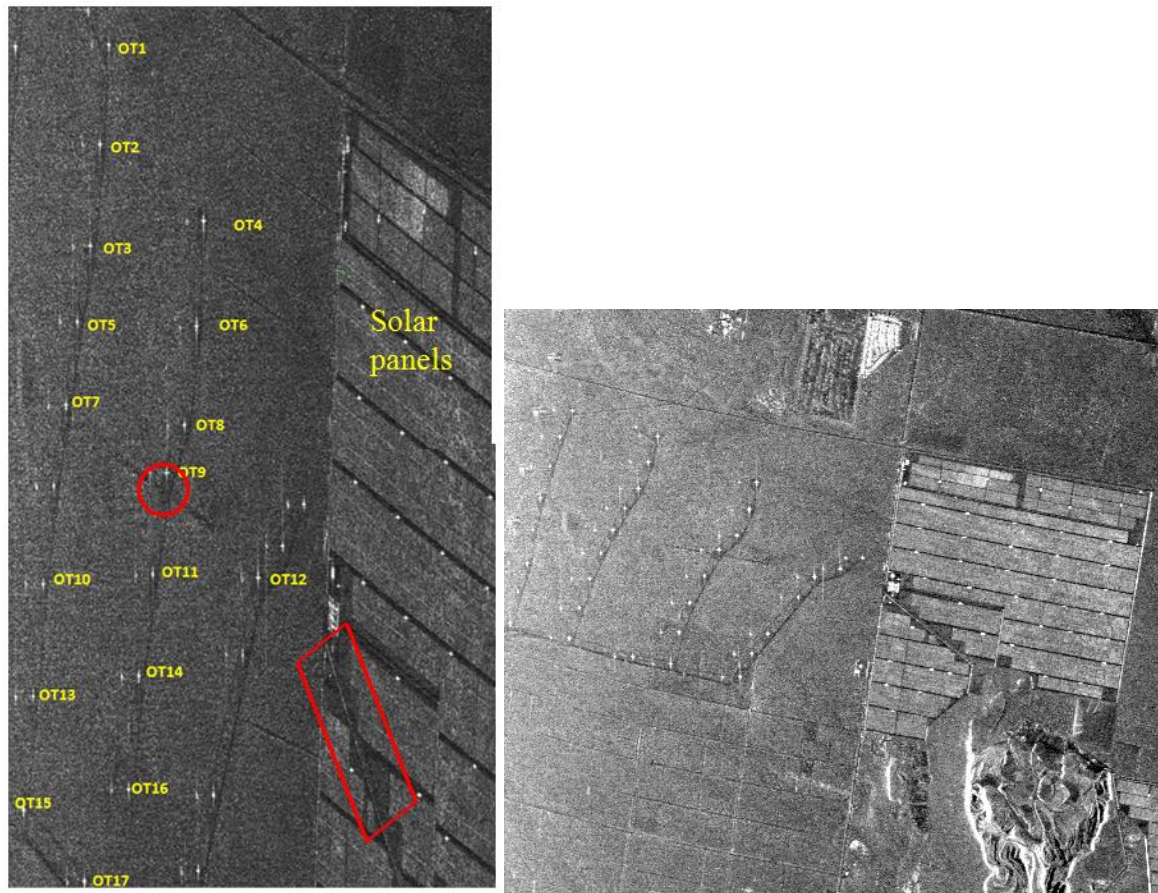


Figure 37: The SLC/MLC (left/right) tile of UAVSAR L-band data showing windmills

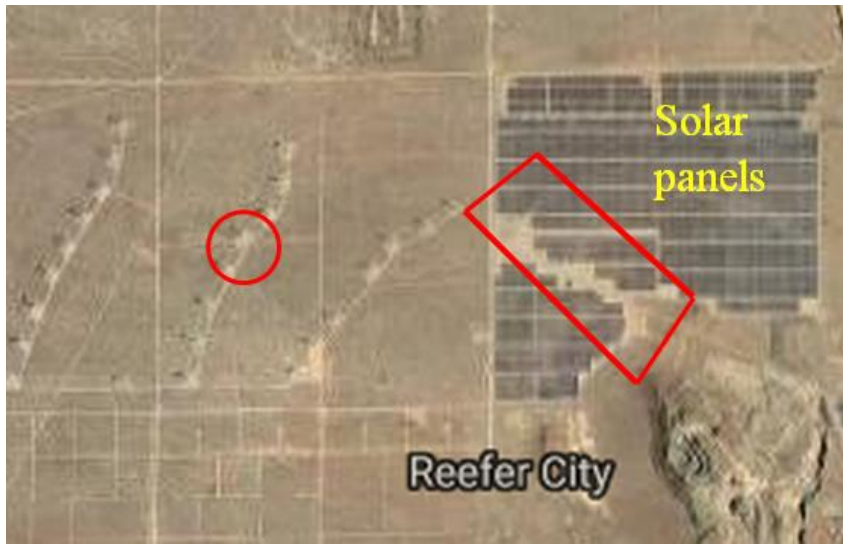


Figure 38: Showing windmills in Google Earth image

In this study we used windmills as opportunistic targets (details in Table 22) for validation of azimuth and range resolutions. The above Figures 37 & 38 shows the windmills which are visible in the SLC, Multi look data and Google earth image for verification of them.

Table 22: Range and Azimuth resolution at 3dB width using opportunistic targets (windmills)

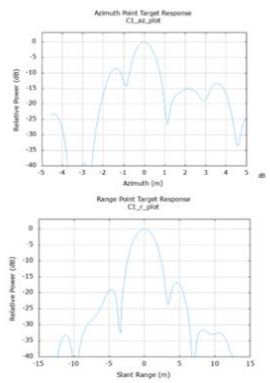
| Opportunistic Targets (OT) | Polarization | Range_3dB width | Azimuth_3dB width | SCR (in dB) |
|----------------------------|--------------|-----------------|-------------------|-------------|
| OT01 (363, 5799) | VV | 2.952 | 0.845 | 40.1827 |
| OT02 (341, 6043) | VV | 2.880 | 0.945 | 44.5314 |
| OT03 (318, 6293) | VV | 2.697 | 0.986 | 45.8941 |
| OT04 (595, 6231) | VV | 2.725 | 0.943 | 46.6587 |
| OT05 (286, 6477) | VV | 2.853 | 0.822 | 37.6775 |
| OT06 (578, 6490) | VV | 2.731 | 0.808 | 41.7496 |
| OT07 (258, 6682) | VV | 2.852 | 1.041 | 43.9584 |
| OT08 (549, 6732) | VV | 2.733 | 1.047 | 42.5240 |
| OT09 | VV | 2.830 | 0.993 | 47.5683 |

| | | | | |
|-----------------------------|----|-------|-------|---------|
| (507, 6865) | | | | |
| OT10 (204, 7138) | VV | 2.913 | 0.914 | 42.0526 |
| OT11 (473, 7112) | VV | 2.771 | 1.043 | 33.6091 |
| OT12 (730,7123) | VV | 2.786 | 0.958 | 46.7286 |
| OT13 (179, 7414) | VV | 2.764 | 1.219 | 38.5753 |
| OT14 (439, 7363) | VV | 2.767 | 0.919 | 41.9744 |
| OT15 (155, 7693) | VV | 2.906 | 0.846 | 42.1335 |
| OT16 (413, 7641) | VV | 2.850 | 0.877 | 43.5783 |
| OT17 (305, 7867) | VV | 2.757 | 0.915 | 44.1853 |

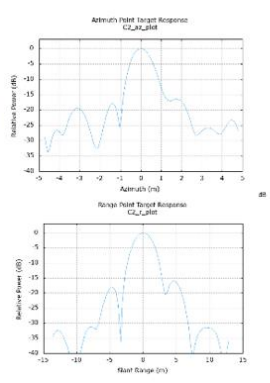
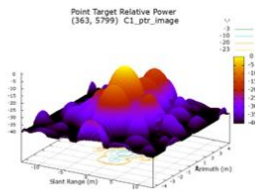
Clutter = 424, 6382

From the above Table 22 we observed that the azimuth resolution is 0.84 meters and range resolution is 2.81 meters respectively which is approximately close to the specified values. IRF are generated for each OT and are shown in below Figure 39.

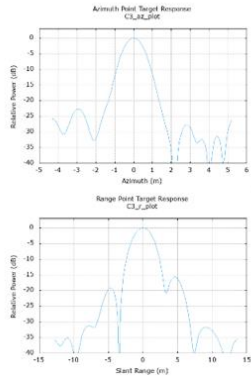
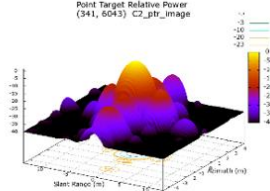
Response functions from the windmills



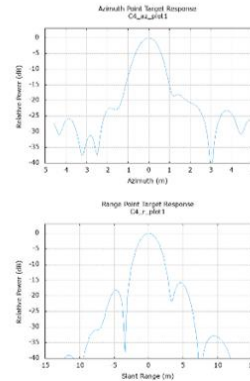
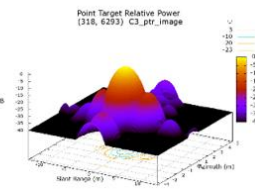
CR1



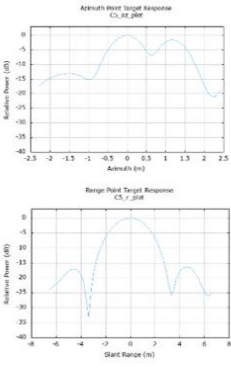
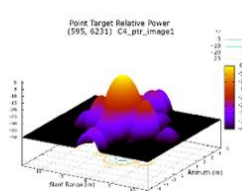
CR2



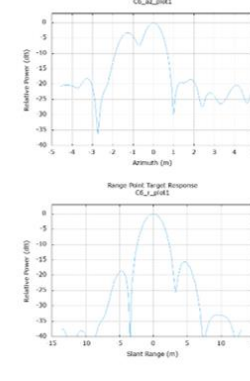
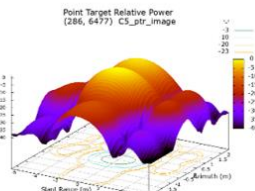
CR3



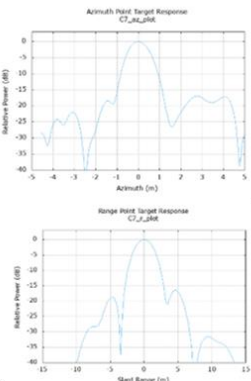
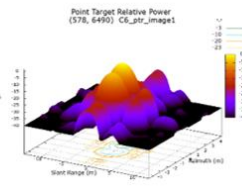
CR4



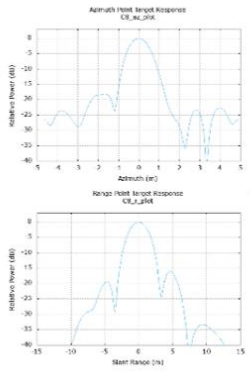
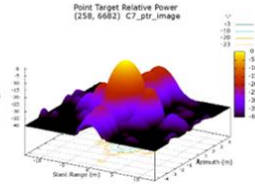
CR5



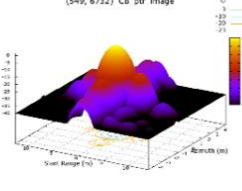
CR6

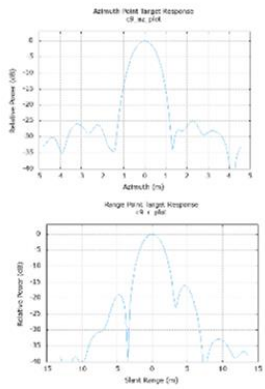


CR7

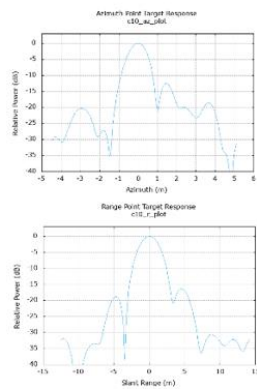
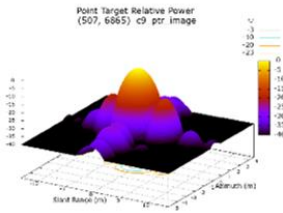


CR8

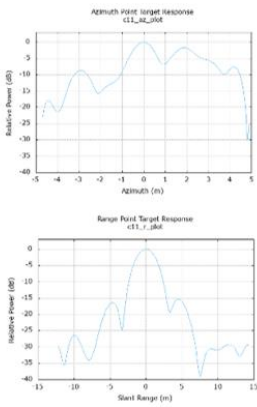
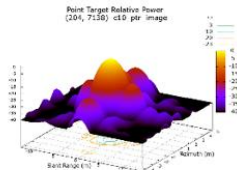




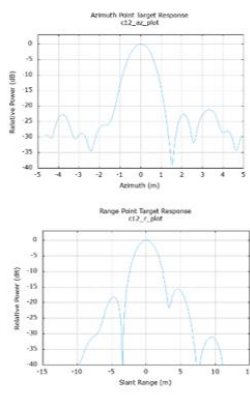
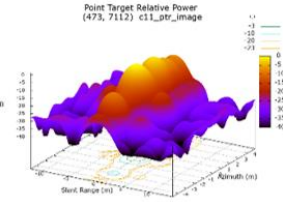
CR9



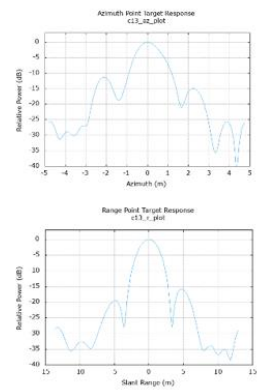
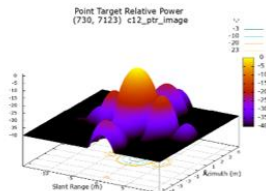
CR10



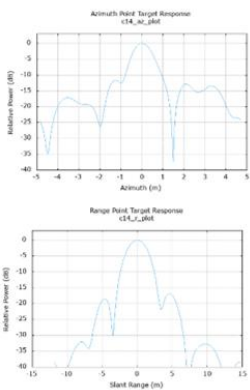
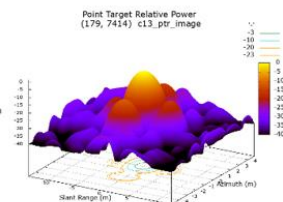
CR11



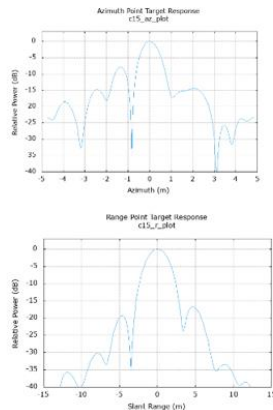
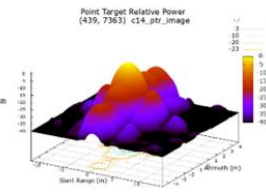
CR12



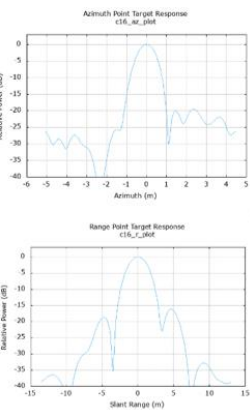
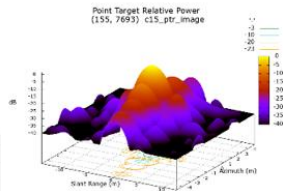
CR13



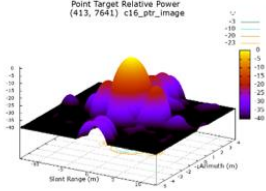
CR14



CR15



CR16



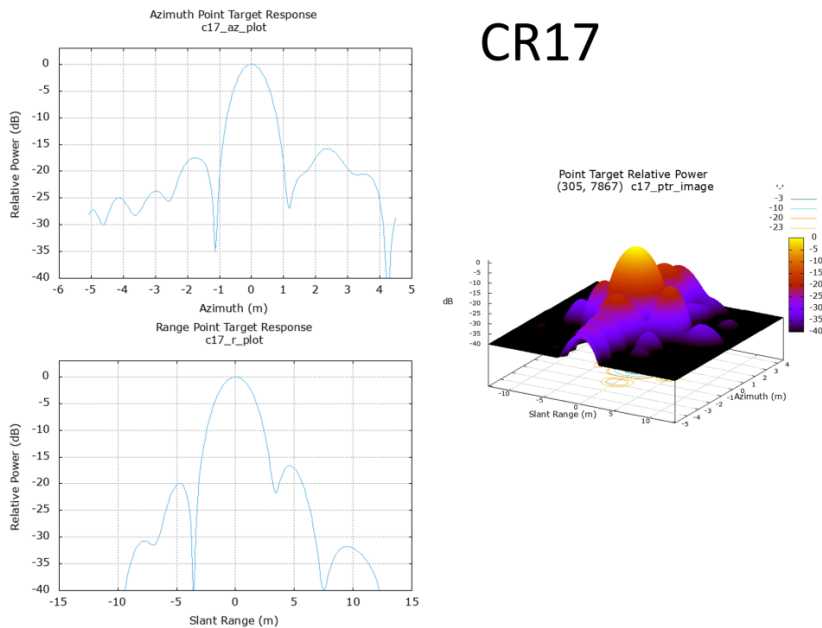


Figure 39: Impulse response function of windmills using SLC HH pol. data

6.3 Results for Gamma Naught stability analysis carried out for Amazon Rainforest and Boreal Forest- Canada.

Inter-annual variation of gamma naught values over Amazon rainforest: Using C-band

The inter-annual variation of gamma naught over Amazon rainforest is shown in Figure 40 for the years 2015, 2016 & 2017 respectively using C band data from Sentinel-1 satellite. The time series graph helps to understand the changes in gamma naught values, which occurred in the observation period and to observe the stability of rainforest in different polarization of the data. Amazon Rainforest has Rainy and dry seasons, rainy season starts from October to May and Dry / summer season is from June to September. In Rainy season, heavy rainfall occurs up to 80 to 430 inches (rainforest.mongabay, n.d.), which leads to ice formation, hailstorm and presence of moisture on leaves.

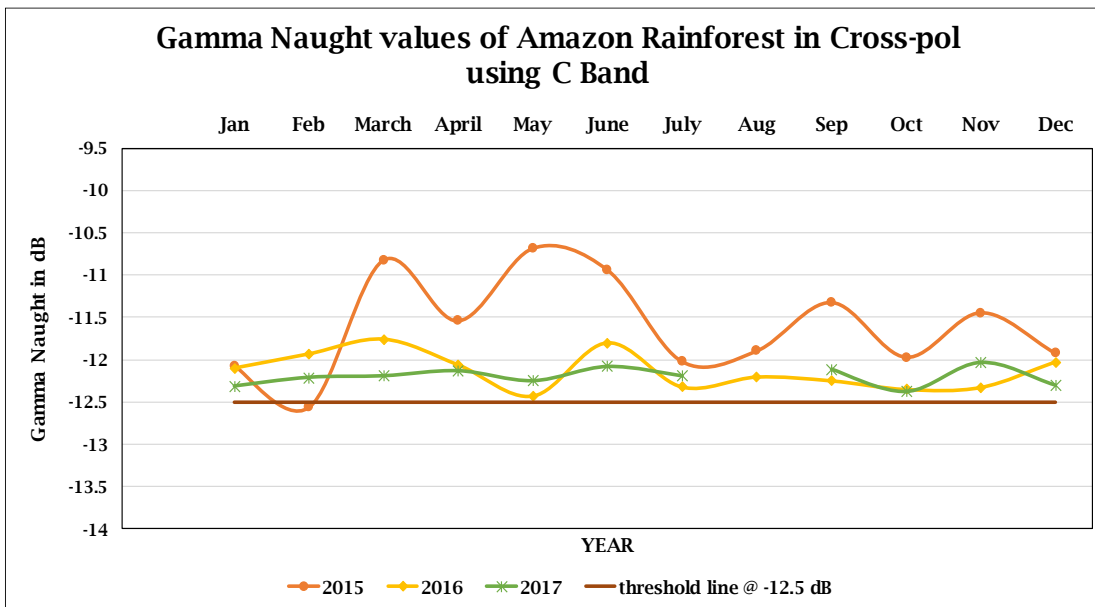
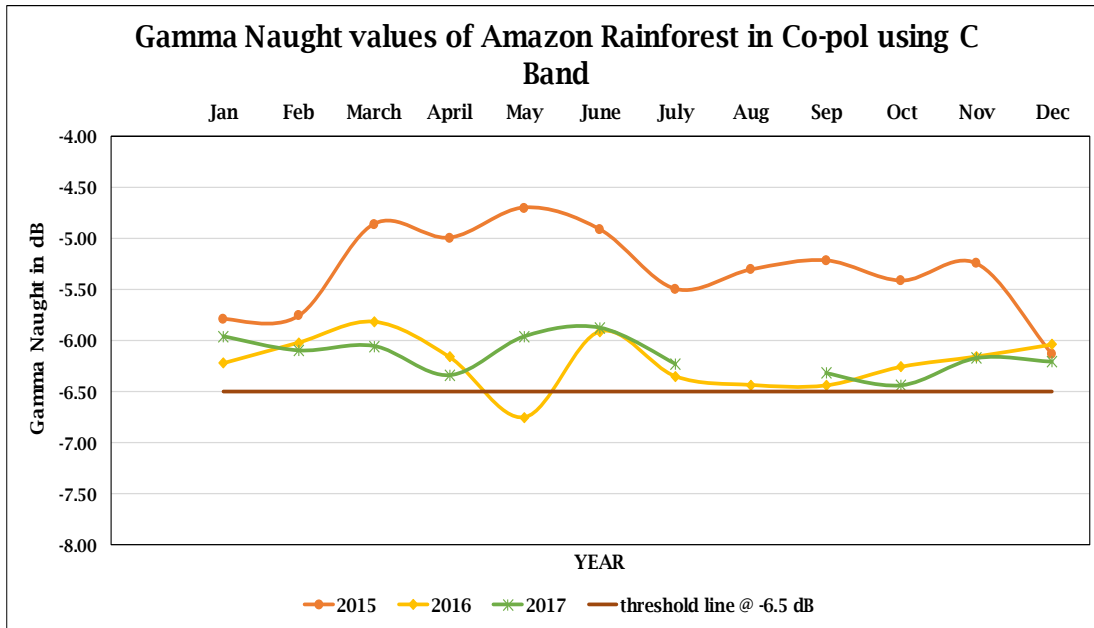


Figure 40: Inter-annual Gamma Naught values of Amazon in Co & Cross-pol using C band

From the above graph the 2015-year data-line, shows that the gamma naught values of co-pol (HH, VV) in the rainy season (March, April, May and June) are near to -4.70 dB, and in the dry season i.e., from July to November, the gamma values are consistent and near to -5.5dB. Throughout the year, the gamma naught values in co-pol (HH, VV) vary from -5.79 dB to -6.04 dB, while in cross-pol (HV, VH), the values vary from -12.07 dB to -11.92 dB. For the year 2016, the gamma naught values observed to be mostly consistent, with minor disturbance in May. Throughout the year, the

calculated gamma naught values in co-pol (HH, VV) vary from -6.22 to -6.04 dB. The gamma value in cross pol (HV, VH), observed to be varying from -12.09 to 12.03 dB. The year 2017, the gamma naught values observed are consistent, without any noticeable variation in calculated gamma values. Throughout the year, the calculated gamma naught values in co-pol (HH, VV) vary from -5.96 to -6.21dB. The gamma value in cross pol (HV, VH), observed to be varying from -12.3 to -12.45 dB.

Even with the presence of sudden rise and fall of the gamma naught values, it is observed that the graphs patterns are similar and approximately overlapping each other. From the above inter annual graphs and discussions, the calculated average gamma naught value is -5.88 ± 0.29 dB in co-pol (HH, VV) and -11.95 ± 0.29 dB in cross-pol (HV, VH). Consistent stability is observed over the study area of Amazon Rainforest. Meanwhile, understanding the aftermath on gamma values due to season change is the key factor deciding the stability of the rainforest. These values are found to be similar to the results obtained for Amazon rainforest using RISAT-1 MRS mode data for the study period 2014-2015 (*Sharma, et al., 2017*).

Variation of gamma naught values observed in Rainy and Dry season: Using C-band data

Understanding the variations in gamma naught values due to change in seasons of the Amazon rainforest is important as it decides the stability throughout the year of the distributed target site. Amazon rainforest is more prone to rainy season rather than other seasons. The Amazon rainforest has *Rainy* Season-October to May and *Dry* Season-June to September. Accordingly, data is separated and plotted for rainy and dry seasons, which is distinguished by yellow and blue colors respectively as shown in Figure 41.

In Amazon forest the gamma naught values in co-pol (HH, VV), are varying from -5 dB to -6.34 dB in rainy season and -4.91 dB to -6.44 dB in dry season respectively. If we observe the above graph, the years (2015, 2016, and 2017) considered has -5.5 dB as constant gamma-naught value in both rainy and dry seasons. The gamma naught value in co-pol can be written as -5.86 ± 0.51 dB in rainy season and -5.83 ± 0.55 dB in dry season.

In cross-pol, the gamma naught value varies within -12.07 dB to -12.31 dB in rainy season and -10.94 dB to -12.11 dB in dry season respectively. From the graph, a constant -11.5 dB is observed for gamma value in both seasons. It can be represented as -11.96 ± 0.46 dB in rainy season and -11.93 ± 0.43 dB in dry season.

Between rainy and dry season, seasonal variation observed was 0.03 dB in co-pol (HH, VV) and 0.03 dB in cross-pol (HV, VH). The above difference due to season change is minimal, thus proved that gamma naught value is stable throughout the year independent of season change.

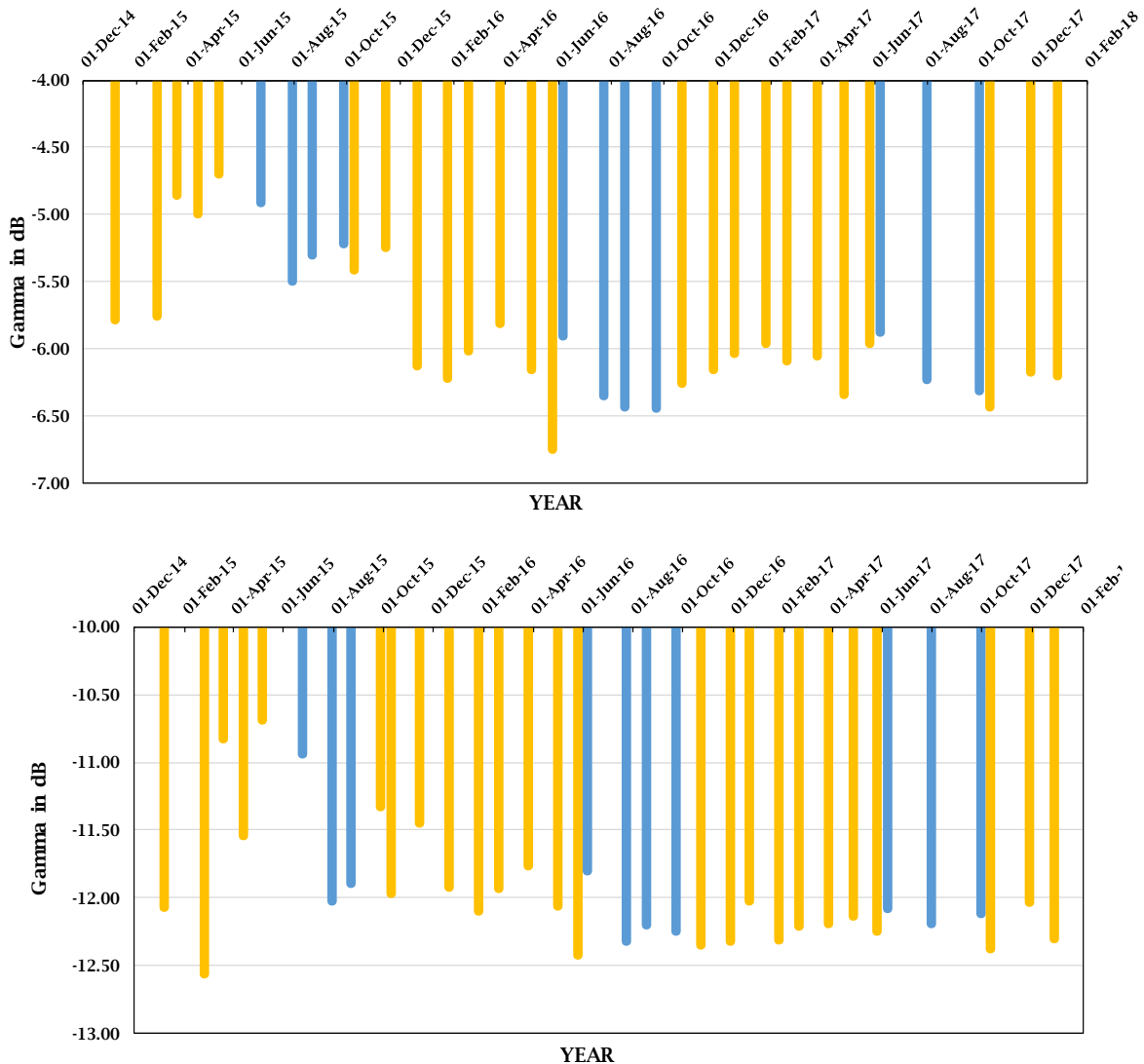


Figure 41: Intra-annual gamma naught values of rainy (yellow) and dry (blue) seasons in co & cross-pol using C band.

Annual Variation of gamma naught values: Using L band ALOS PALSAR 2 mosaic data.

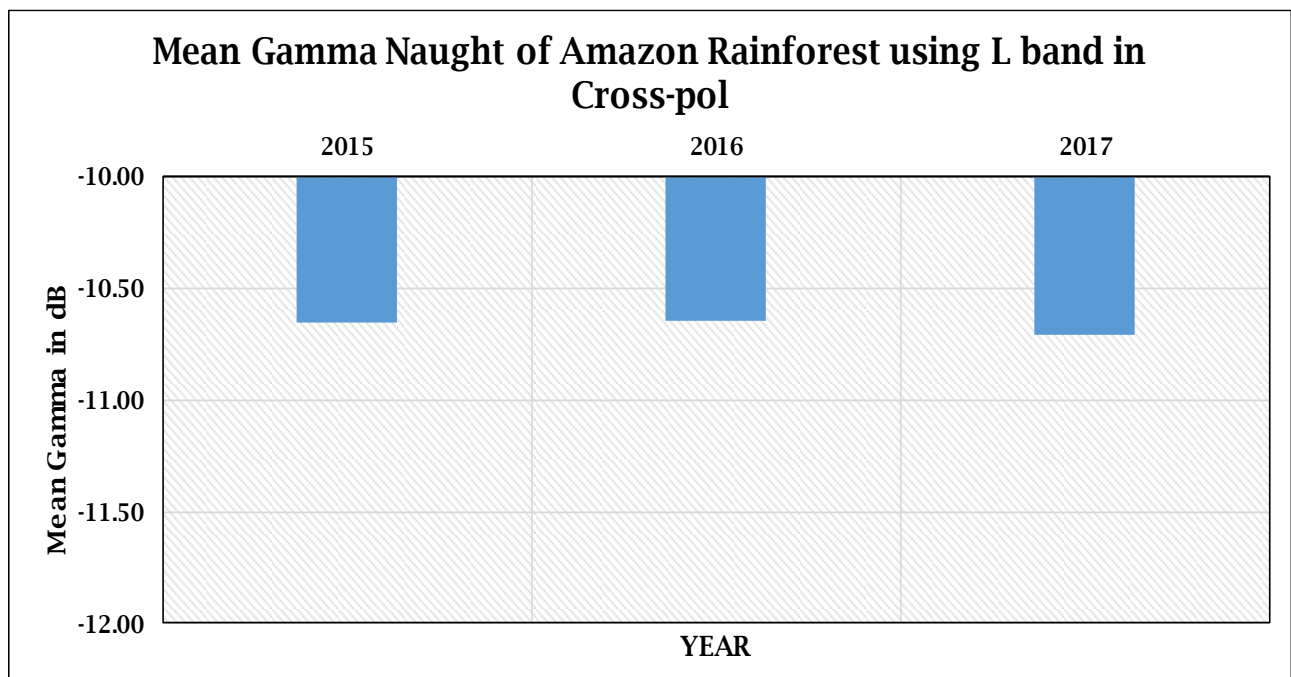
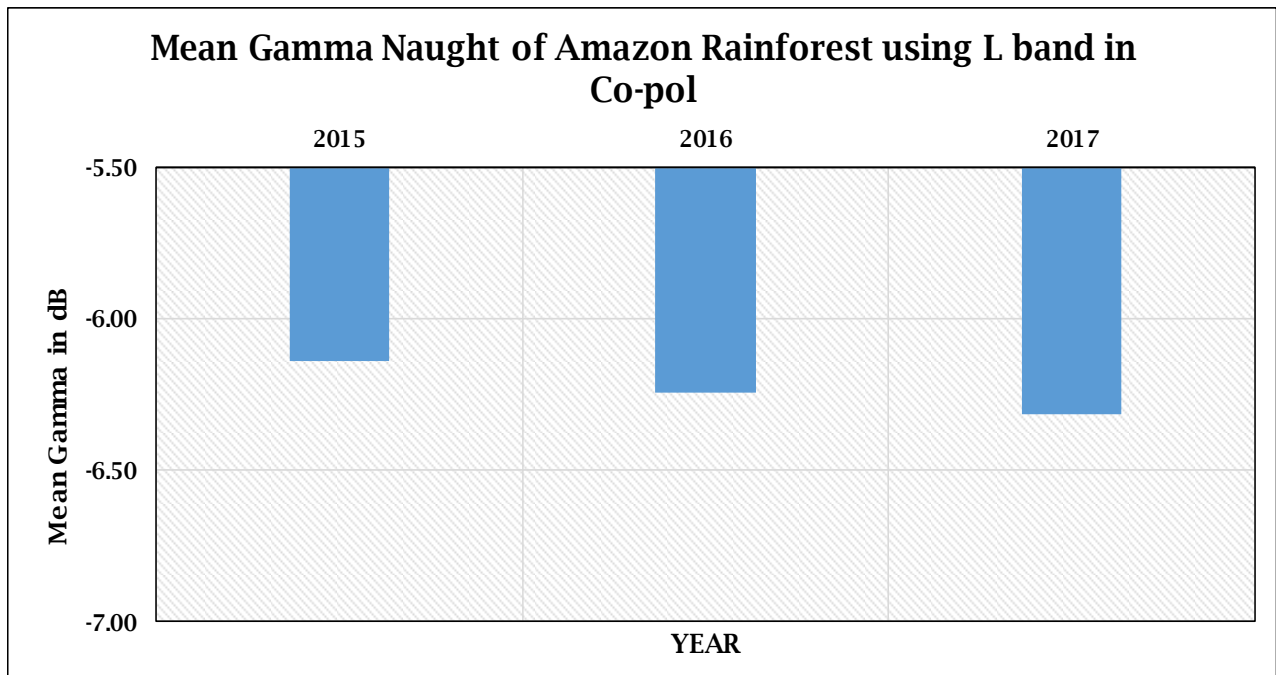


Figure 42: Annual Mean Gamma Naught values of Amazon in co & cross-pol using L band

Gamma naught values of Amazon rainforest are calculated for the years 2015, 2016 and 2017 using L-band mosaic product of ALOS-2 as shown in Figure 42. The graph helps in observing

that, the gamma naught values are -6.13 dB, -6.24 dB and -6.31 dB in co-pol (HH, VV) and -10.65 dB, -10.65dB and -10.71 dB in cross-pol (HV, VH) respectively. The gamma values fluctuates within -0.36 to -0.19 dB in co-pol and -1.84 dB to -1.79 dB in cross-pol. The gamma naught values are -6.23 ± 0.08 dB in co-pol and -10.67 ± 0.03 dB in cross-pol. The observed gamma naught values in L band is nearly the same as C band value.

All the section above helps in understanding the stability pattern of Amazon rainforest during the seasonal change and throughout the year, while the Figure 43, helps in quantitative comparison of the L and C band calculated gamma naught values to determine suitable frequency data.

Annual Comparison of the Mean Gamma Naught values obtained from the data of Sentinel-1 and ALOS PALSAR 2.

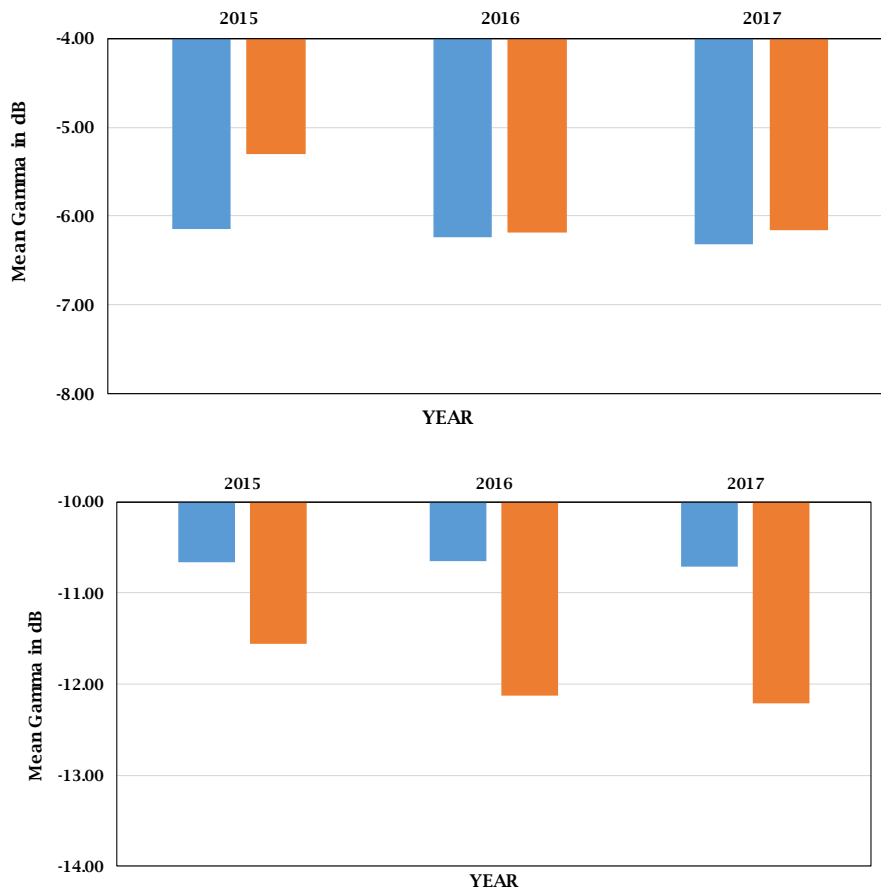


Figure 43: Annual Quantitative Comparison of L (blue) and C (orange) band's Mean Gamma Naught values in Co & Cross-pol.

This Section shows the quantitative difference between L and C band calculated gamma naught values, which helps in determining suitable frequency data to conduct the stability studies for distributed targets. Average mean gamma naught values of L and C band are used to construct the above graph (Figure 43).

In co-pol (HH, VV) the gamma naught values of L and C band are -6.14 dB and -5.30 dB in year 2015, -6.24 dB & -6.19 dB in year 2016 and -6.31 dB & -6.15dB in year 2017 respectively. Likewise, in cross-pol (HV, VH), the gamma naught values of L and C band are -10.65 dB & -11.56 dB in year 2015, -10.65 dB & -12.13dB in year 2016 and -10.71 dB & -12.21 dB in year 2017 respectively. From the above values, the average gamma naught value of co-pol and cross-pol can be rewritten as -5.88 ± 0.29 dB & -11.95 ± 0.29 dB of L band and -6.23 ± 0.08 dB & -10.67 ± 0.03 dB of C band respectively.

From the above results, it is observed that the gamma naught values of Amazon rainforest are nearly same for both L and C band in co-pol data during the study period except for 2015 where the difference was found to be ~ 0.7 dB. However, for cross-pol data, the difference between the L-band and C-band results was found to be more in all the years. The gamma naught values derived from L-band data were close to the specified value of -12.5 dB. The reason might be attributed to the high wavelength of L-band than C-band. The return from it is just not from the canopy but it also strikes the branches, twigs, leaves of the tree, before getting backscattered to the sensor.

Inter-annual gamma naught values of C and L band data are shown in Figure 43. The gamma naught value of C band, data are -5.30 dB, -6.19 dB and -6.15 dB in co-pol and -11.56 dB, -12.13 dB and -12.21 dB in cross-pol for the years 2015, 2016 and 2017 respectively.

Comparison with the results reported in the literature

1. Prototyping Radio-metrically Terrain Corrected Sentinel-1 Data at the Alaska Satellite Facility: (Hogenson)

The RCS results show that the co-pol product was near or at the accepted value of -6.5 dB in Gamma naught over the Amazon rainforest. The average cross-pol RCS was around -12.5 for

these products. Both processors preserved the calibration quality of the original GRD products provided by ESA.

2. PALSAR radiometric and geometric calibration:*(Isoguchi, 2010)*

Amazon forest provides a constant and almost seasonally independent gamma-naught for a wide range of incidence angles and can be used as a reference calibration target. JERS-1 SAR confirmed that the NRCS-NORMALIZED RADAR CROSS SECTION of the Amazon forest is seasonally independent with a value of -7.5 dB and a seasonal variation of 0.27 dB thus, the corresponding gamma-naught is -6.5 dB. PALSAR data has strip mode, average gamma naught of -6.52 dB with standard deviation of 0.22dB for all incidence angles. SCANSAR has -6.65dB with deviation of 0.4dB

3. Long-term stability of L-band normalized radar cross section of Amazon rainforest using the JERS-1 SAR: *(Shimda M. , 2005)*

This paper describes the long-term stability of L-band synthetic aperture radar (SAR) data observed over the Amazon and the applicability of the Amazon as a calibration reference. The author evaluated 139 Japanese Earth Resources Satellite 1 (JERS-1) SAR images acquired over the southwest Amazon during six and a half years (1992–1998), including wet and dry seasons. During each season, the data appeared to be stable, with mean values of -6.81 and -7.08 dB, standard deviations of 0.20 and 0.18 dB, and a 0.27 dB difference between the two seasons. The Amazon is thus a stable reference for calibration.

4. PALSAR CAL-VAL Summary: *(Shimda M., 2007)*

The statistical analysis shows that the seasonal variation is only 0.25 dB, which shows the stability of Amazon rainforest. The limited condition for the deployment of the corner reflector requires the inclusion of the Amazon based calibration both for relative and absolute calibration. At the beginning of the PALSAR Cal-Val, they determined the gain, offset among the beams, so that the gamma naught could be constant over the incidence angle, i.e., $\gamma^\circ = \frac{\sigma^\circ}{\cos\theta} = \text{constant}$. Where, θ is the incidence angle. They confirmed the validity of this assumption using the 10 Amazon data for the strip mode and two data for the SCANSAR.

Canadian Boreal Forest

Variation of gamma naught observed throughout the year: Using C band data

Below Graph, as shown in Figure 44, is the average Mean Gamma Naught of Canadian Boreal Forest in dual pol (VV, VH) from the year 2015-2017

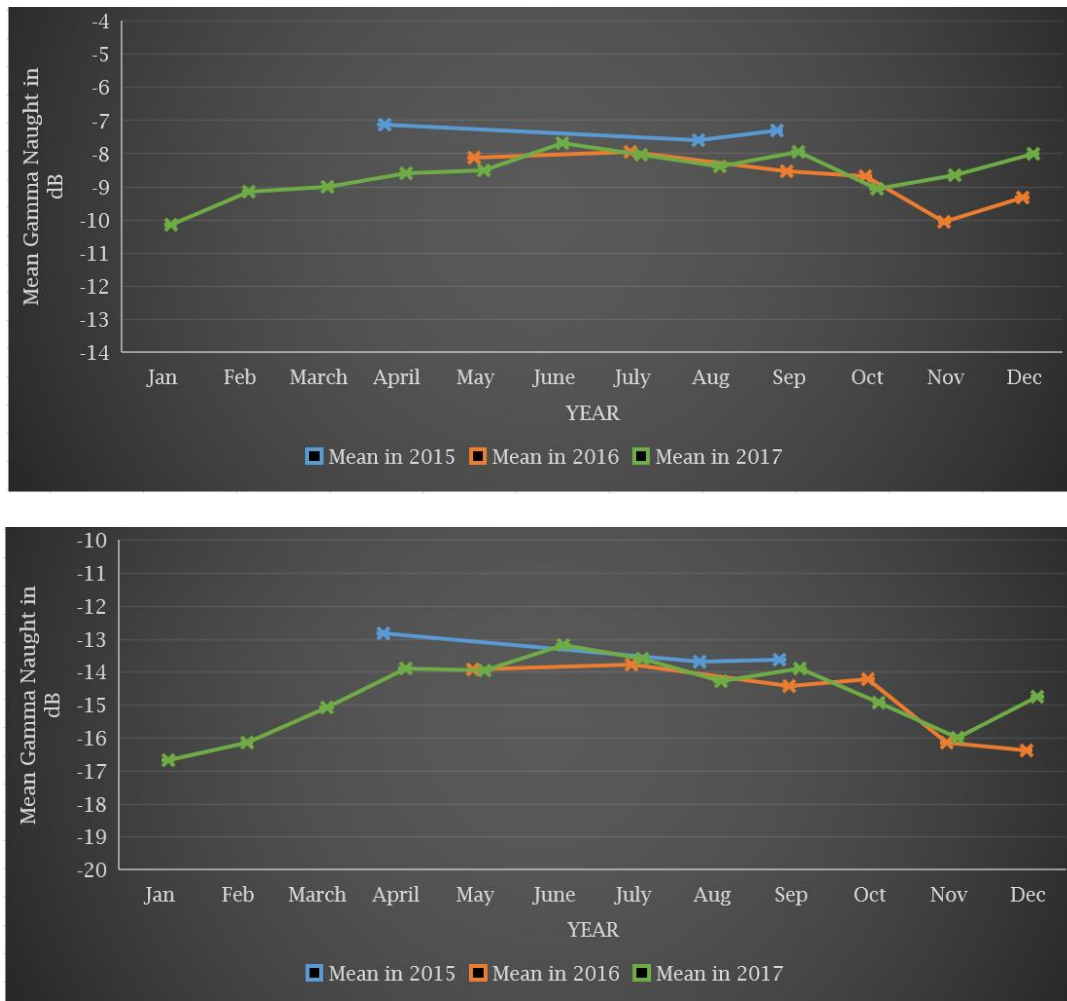


Figure 44: Monthly variation of average gamma naught in VV & VH pol. using C band.

The Figure 44 displays gamma naught values over Canadian Boreal rainforest calculated for the years 2015, 2016 & 2017 respectively using C band data from Sentinel-1 satellite. Boreal forest has summer (temperature ranges from -7°C to 21°C) and winter seasons (temperature ranges from -54°C to -1°C), it starts from December to February and summer season is from June to August. The freezing temperature in winter helps in ice formation over tree canopy and the summer

temperature is above freezing point leads to melting of ice and thus changes in the gamma naught values are observed.

From the above graph year 2015 data-line, shows that the gamma naught value in VV pol. which vary from -7.14 to -7.31 dB. The data available in this year falls in summer season, due to temperature above zero degree helps in melting of accumulated ice providing variation in gamma naught value. Throughout the year, the gamma naught value is -7.34 ± 0.23 dB respectively. While in VH, the gamma value varies from -12.84 dB to -13.64 dB, the gamma naught value is -13.37 ± 0.48 dB

From the above graph 2016-year data-line, the gamma naught values observed to be mostly consistent, with minor disturbance in November. The disturbance may be due to formation of ice on the target which affects gamma naught value. Throughout the year, the calculated gamma naught values in VV vary from -8.14 to -9.33 dB and the value is -8.71 ± 0.70 dB. The gamma value in VH, observed to be varying from -13.93 to 16.38 dB and the value is -14.68 ± 1.03 dB

From the above graph 2017-year data-line, the calculated gamma naught values observed are increasing and consistent, without any noticeable variation in calculated gamma values. Throughout the year, the calculated gamma naught values in VV vary from -10.16 to -8.02 dB and the value is -8.57 ± 0.65 dB. The gamma value in VH, observed to be varying from -16.7 to -14.76 dB the value is -14.60 ± 1.18 dB

Even with presence of sudden rise and fall of the gamma naught values of the years 2015 to 2017, it is observed that the graphs patterns are similar and proximately overlapping each other. From the above temporal graphs and discussions, the calculated average gamma naught value is -8.16 ± 0.53 dB in VV and -14.1 ± 0.89 dB in VH. Consistent stability is observed over the study area of the boreal forest. Meanwhile, understanding the aftermath on gamma values due to season change is also the key factor in deciding the stability of the boreal forest.

Variation of gamma naught observed in Summer and Winter season: Using C band data

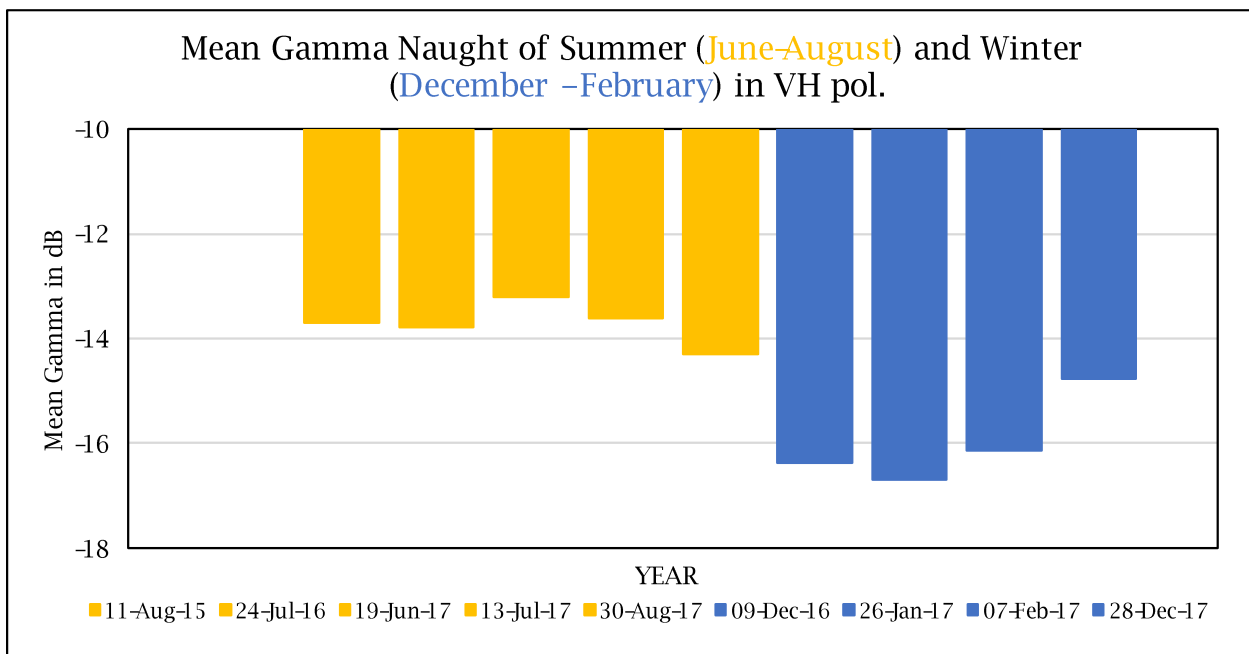
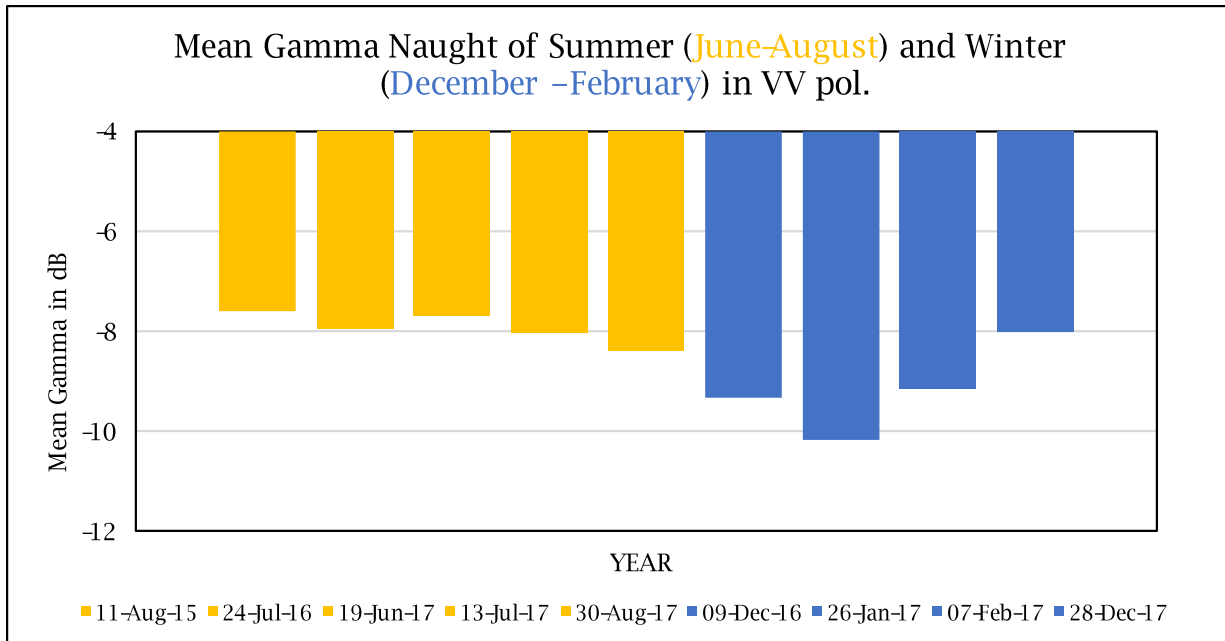


Figure 45: Seasonal variation graph for summer and winter in VV & VH pol. using C band data

As season changes, backscatter from the target varies which cause changes in gamma naught calculations as shown in Figure 45. Understanding these variations in gamma naught values due to change in seasons of the boreal forest is important in deciding the stability of the distributed target site. Winter season in Boreal forest area starts from December to February and summer season from June to August. Accordingly, data is separated and plotted for winter and summer

seasons, which is distinguished by yellow and blue colors respectively. The backscatter in forests was indeed determined by the dielectric properties of the forest floor (snow cover and soil moisture). Since almost all images were acquired when the ground was either wet or covered with wet snow, it has not been possible to compare with typical backscatter values of dry-unfrozen conditions i.e., comparison with -6.5 dB threshold.

In winter season, temperature is below the freezing point - formation of dry snow occurs, which results in change of Gamma naught values. Temperature above 0 °C, leads to melting of snow into water, affecting the backscatter values of the forest, which is observed in summer. In boreal forest the gamma naught value in VV pol is -7.60 dB to -8.39 dB in summer and -9.32 dB to -8.01 dB in winter season. We observed that there is constant value of -7.5 dB in both the summer and winter seasons respectively. The gamma naught value is -7.5 ± 0.43 dB in summer season and -8.5 ± 0.66 dB in winter. The gamma naught value in VH pol is -13.69 dB to -14.29 dB in summer and -16.38 dB to -14.76 dB in winter season. We observed that there is constant value of -13.5 dB in both the summer and winter seasons respectively. The gamma naught value is -13.5 ± 0.22 dB in summer season and -15.5 ± 0.49 dB in winter.

Between rainy and dry season, seasonal variation observed was 1.73 dB in VV and 2.27 dB in VH. The variation in gamma naught is of noticeable difference and proves that seasonal change effect the gamma naught value.

Mean Gamma Naught of ALOS PALSAR 2 - L Band mosaic data.

The Figure 46 shows mean Gamma naught of L-band (1.2 GHz) which is mosaic product. Gamma naught values of boreal forest are calculated for the years 2015, 2016 and 2017. The graph helps in observing that; the gamma naught values are -6.74 dB, -6.33 dB and -6.71 dB in HH pol. and -12.99 dB, -12.26 dB and -13.11 dB in HV pol. The mean gamma values -6.59 ± 0.23 dB in co-pol and -12.77 ± 0.46 dB in cross-pol. The calculated gamma naught values are identical and proves that stability is observed in boreal forest. All the section above helps in understanding the stability pattern of boreal forest, and below graph (Figure 47) helps in quantitative comparison of the L and C band calculated gamma naught values.

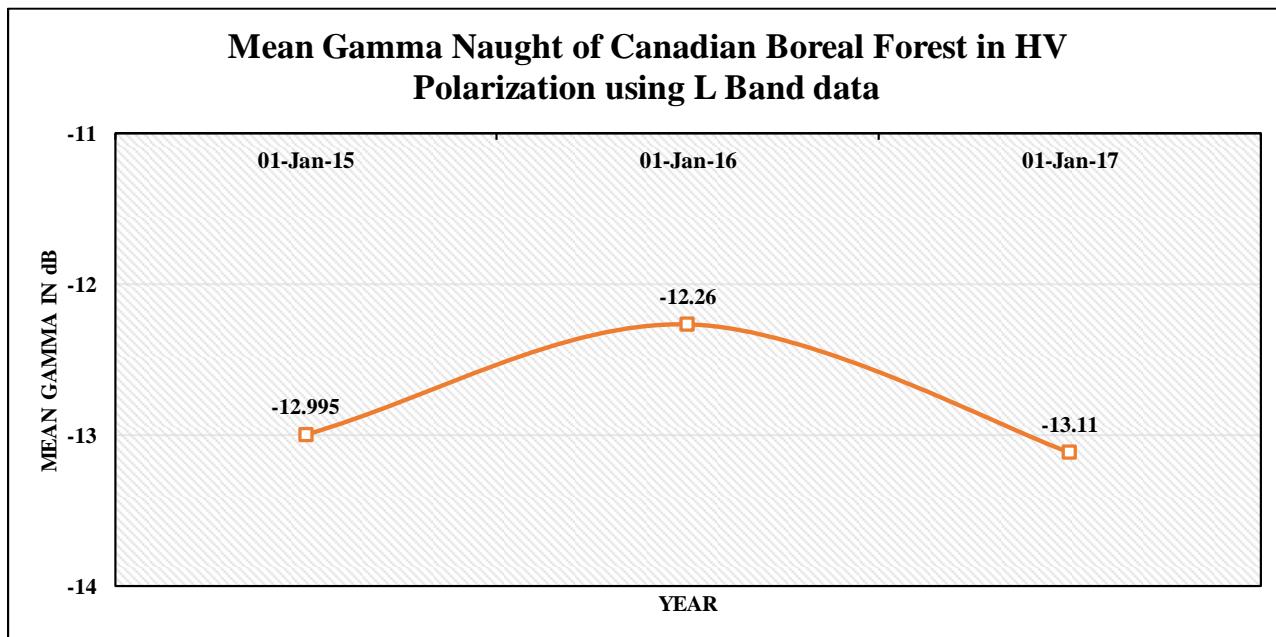
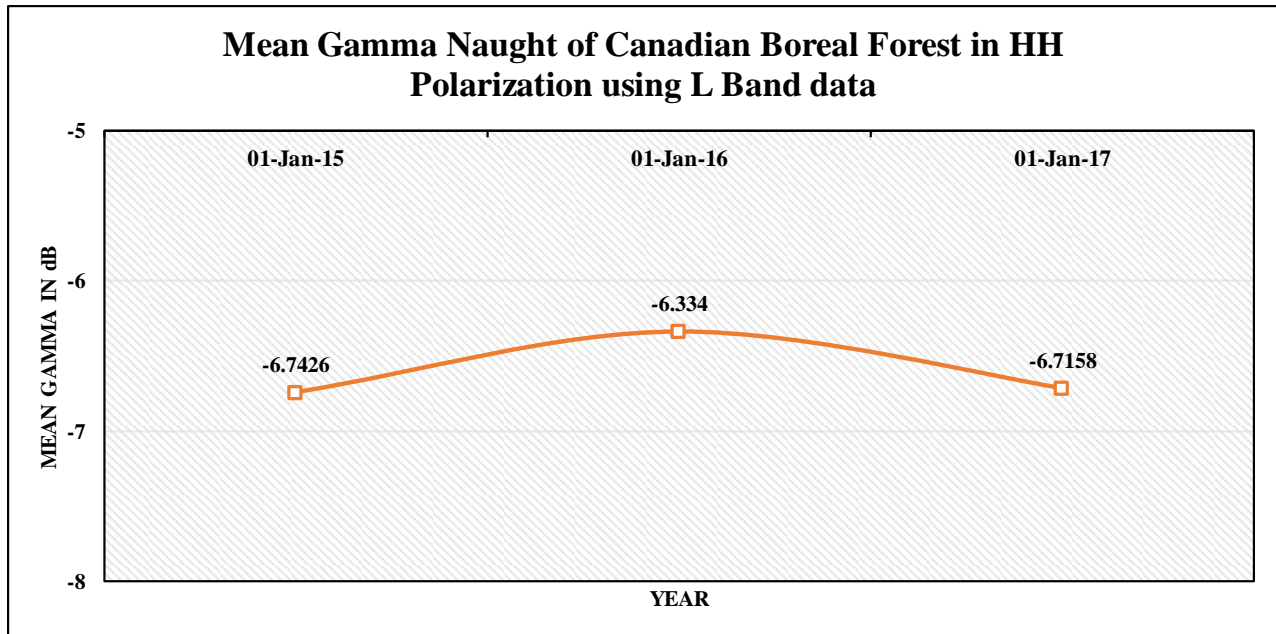


Figure 46: Mean Gamma Naught in HH & HV pol using L band

Comparison of the Mean Gamma Naught values obtained from the data of Sentinel-1 and ALOS PALSAR 2.

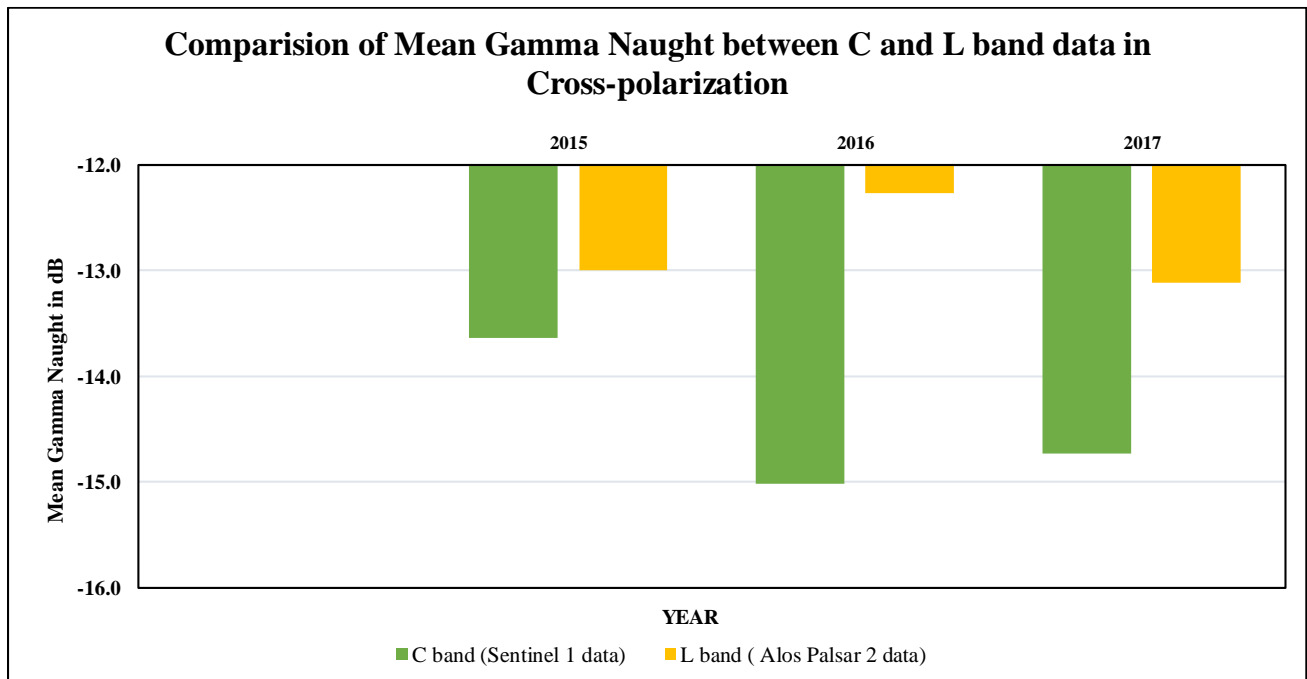
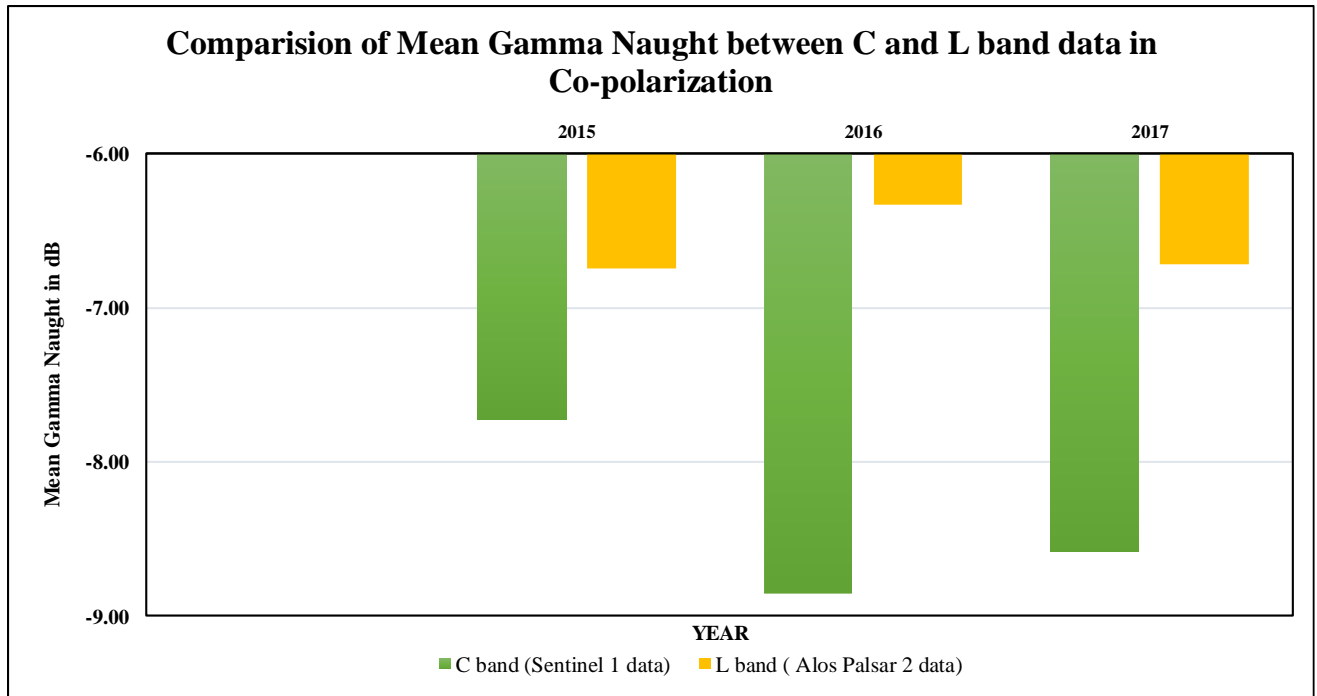


Figure 47: Comparison of C and L band, Annual Gamma Naught in Co & Cross-pol

This Section shows the quantitative difference between C and L band calculated gamma naught values, which helps in determining suitable frequency data to conduct this kind of stability

studies for distributed targets. Average mean gamma naught values of L and C band are used to construct the above graph as shown in Figure 47.

The gamma naught values of C band in co-pol are -7.72 dB in year 2015, -8.85 dB in year 2016, -8.58 dB in year 2017 respectively. While gamma naught values in L band are -6.74 dB, -6.33 dB, -6.72 dB for 2015, 2016 and 2017 respectively. The gamma naught values of C band in cross-pol are -13.64 dB in year 2015, -15.01 dB in year 2016, -14.73 dB in year 2017 respectively. While gamma naught values in L band are -13.00 dB, -12.26 dB, -13.11 dB for 2015, 2016 and 2017 respectively. From the above values, the average gamma naught value of co-pol and cross-pol can be rewritten as -7.5 ± 0.24 dB and -13.5 ± 1 dB of C band and -6.5 ± 0.1 dB & -12.5 ± 0.29 dB of L band respectively.

The gamma naught values of L band are mostly identical without any disturbances. To check the validity of the gamma values obtained from L band, data of same area is downloaded from “Alaska data facility” and “ALOS 2 Jaxa” sites. The following results are obtained:

| L BAND DATA | | | |
|---|----------|--|---------|
| Data from Alaska Data facility 25m | | Data from ALOS 2 data site 100m FNF | |
| Date | Co-pol | Date | Co-pol |
| 22-Feb-07 | -10.9356 | 2007 | -6.823 |
| 25-Nov-07 | -8.4434 | 2008 | -6.9982 |
| 10-Jan-08 | -9.4605 | 2009 | -7.1147 |
| 12-Jan-09 | -9.2805 | 2010 | -6.977 |
| 14-Apr-09 | -6.9395 | | |
| 18-Jan-11 | -8.9642 | | |
| 02-Aug-12 | -8.9814 | | |

From the above table it is observed that gamma naught values of L band data are same as gamma values of C band data derived from Sentinel 1. While gamma naught values of ALOS 2 data are

ideal to -6.5 dB. It can be concluded that C band calculated gamma values and calculated gamma values from L-band data are true because the same values are also observed in previous works.

Comparison with the results reported in the literature

1) Estimation of Biophysical Parameters in Boreal Forests from ERS and JERS SAR Interferometry by MAURIZIO SANTORO(SANTORO 2003)

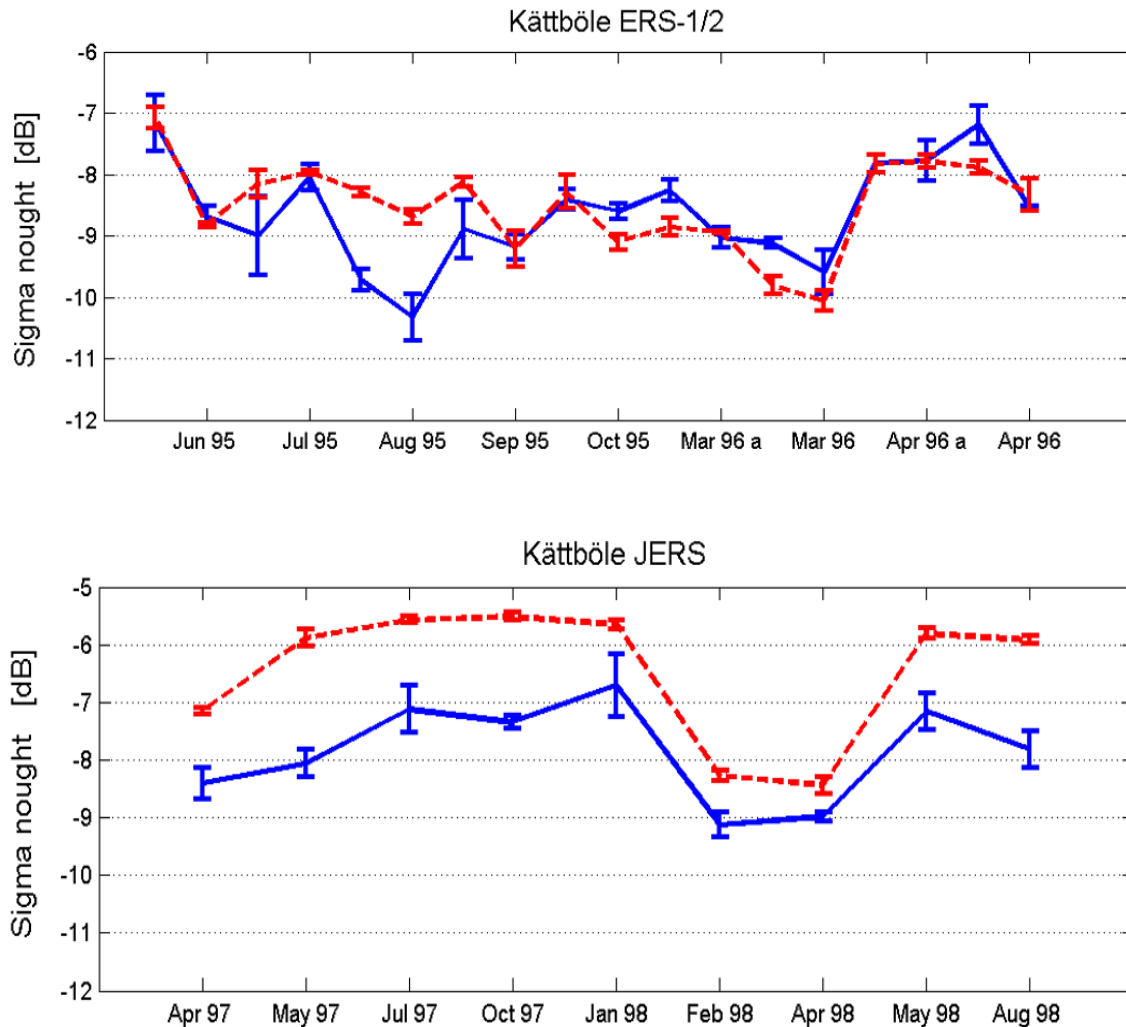


Figure 48: Run of ERS& JERS backscatter in sparse (solid line) and dense forest (dashed line) ©(SANTORO 2003), Study region: Kattabole, Sweden (part of Boreal Forest).

Observations with ERS (C band) data: as shown in Figure 48, it is observed that in dense forest the backscatter was around -8dB and decreased when temperature was below freezing point. In sparse forest, the backscatter shows larger variability and dependent of season. In case of snow

fall it is transparent to radar wave, giving rise to low backscatter. Observations with JERS (L band) data (Figure 48), it is observed that influence of wetlands was stronger on the ERS than on the JERS backscatter. The backscatter of dense and sparse forest was around -6 and -8dB. For dry-unfrozen conditions both in sparse and dense forests the backscatter was found to be higher than for winter-frozen conditions. A frozen canopy and a frozen ground give scatter with less power because the dielectric constant is much smaller. Moreover, an incoming wave penetrates the canopy deeper and the percentage of ground seen by the radar increases. Dry-unfrozen conditions occurred in Kättböle, between May and October 1997 and then again starting in May 1998.

2) RADARSAT -1 Image Quality and Calibration Performance Maintained Beyond 12 Years of Operation by Satish k Srivastava (Satish K srivastava n.d.)

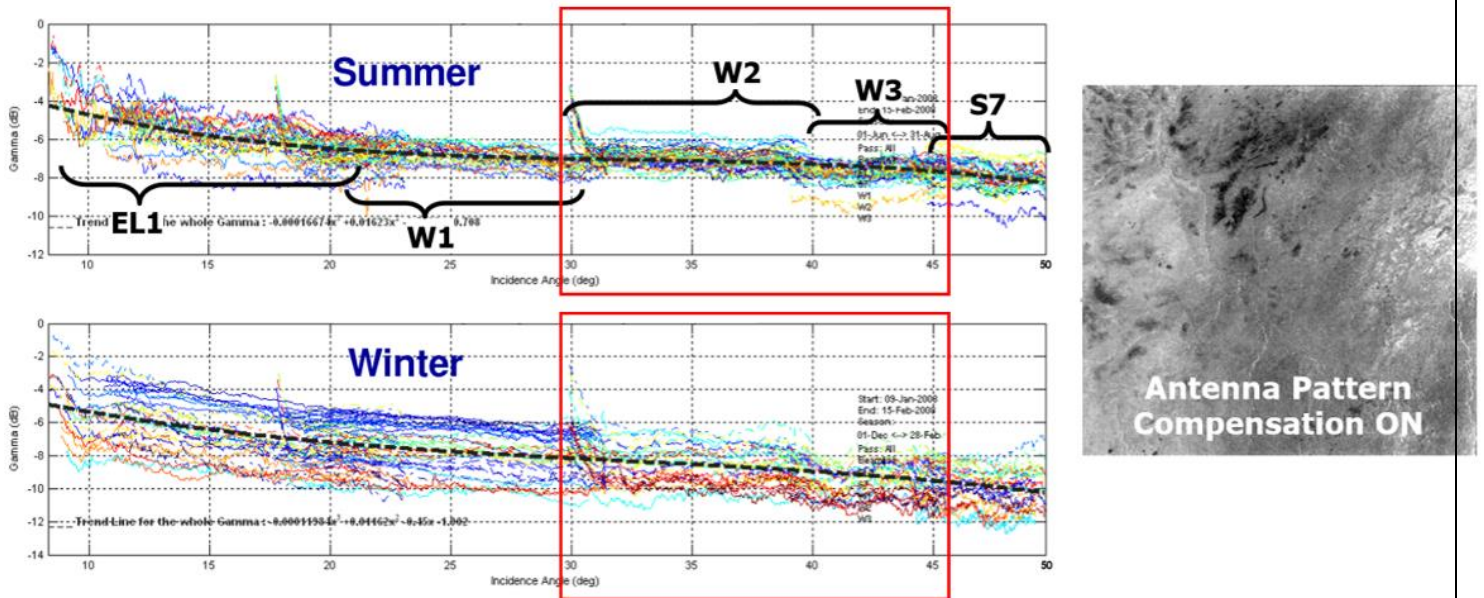


Figure 49: Boreal forest seasonal reflectivity ©(Satish K srivastava n.d.)

The above Figure 49 shows that gamma naught values obtained for Ontario, boreal forest using RADARSAT-1 image. Assuming that beams remain calibrated, gamma naught values are extracted with respect to incidence angle. Sentinel-1 C band has incidence angle from 30° to 45°, which is used for studying stability of boreal forest. With respect to 30° to 45° incidence angle, during summer the gamma naught values are -7.5dB to -8.5dB and in winter the gamma naught values are -8.5 dB to -10 dB, which are observed from the figure above.

The above observed gamma naught values happen to be same as gamma naught values calculated using C band frequency data, mentioned in above section. The inference jotted down in this section helps in proving that calculated gamma naught values are true and are verified with the results obtained from 12 years' study of image quality and calibration performance.

7 Summary and Conclusions

7.1 Conclusions for Stability analysis for corner reflectors deployed in Surat Basin, Australia

Temporal stability assessment of the Radar Cross Section and image quality parameters for the deployed corner reflector array at Surat basin, Australia was carried out. Three dates (25th July, 06th August and 18th August 2019) of Sentinel-1B C-band, SLC data have been used to estimate the mean Radar Cross Section (RCS) and image quality parameters utilizing corner reflector array. The impulse response functions of the deployed corner reflectors were studied and image quality parameters were estimated using the targets response function.

The theoretical peak RCS of a triangular trihedral of 1.5 m CR is 38.37 dBm² at C-band. The mean RCS of 1.5 m trihedral corner reflector was found to be 37.84 ± 0.334 dBm² with an average signal to clutter ratio of 35.55 ± 1.94 dB. The Peak to side lobe ratio is -22.23 ± 0.94 dB in Azimuth and -19.51 ± 0.87 dB in Range direction. Integrated side lobe ratio is -21.29 ± 1.35 dB in Azimuth and -18.59 ± 0.64 dB in Range direction. The Range resolution is close to given value and was found to be 2.66 ± 0.09 meters and the resolution in azimuth direction was found to be 21.87 ± 1.25 meters.

7.2 Conclusions for radiometric and polarimetric calibration of airborne UAVSAR L-band data.

Development of NASA-ISRO Dual frequency SweepSAR (NISAR) is under progress by ISRO in collaboration with Jet Propulsion Laboratory (JPL), NASA. It will provide S- and L-band space-borne SAR data with high repeat cycle, high resolution, and larger swath, with capability of full-polarimetric and Interferometric modes of operation. For the quantitative interpretation of images, acquired by SAR sensor, it is very much important to have properly calibrated data. Due to limited number of datasets available for ISRO's L&S airborne SAR mission (pre-cursor to

NISAR), full-pol data of UAVSAR is used in this study to derive the polarimetric distortion matrix (PDM) and validate the results. In this study, evaluation of the radiometric and polarimetric calibration of full-pol L-band airborne SAR data using point targets and distributed target have been carried out. Analysis of the impulse response function of the point targets show that the estimated azimuth resolution (0.93 ± 0.02 meters) and range resolution (2.69 ± 0.06 meters) are close to the specified values. The difference between the estimated and provided calibration constant was found to be in the range of $1 \text{ dB} \pm 0.45 \text{ dB}$ with a phase calibration error of 1.58° . Co-polarization channel imbalance (f) was found to be 0.985 ± 0.052 (linear units), which is estimated using corner reflectors. While cross polarization channel imbalance (g) was calculated as 1.256 dB which is derived using featureless homogenous area (distributed target). The phase anomaly between cross channel of HV and VH polarization was found to be -2.07° , which indicates that the phase error is high in receiving channel. The undulations present in the polarimetric signatures of co-pol and cross-pol after radiometric and phase correction, indicates that cross talk and channel imbalances are present. Polarimetric signature was also derived for point targets using polarimetric calibrated images. Estimation of polarimetric distortion matrix (PDM) was done using advanced and robust Quegan's algorithm. Application of estimated PDM to the radiometrically and phase corrected dataset is in progress to validate the results. After the validation, this methodology will be utilized for the polarimetric calibration of L&S airborne SAR data and upcoming NISAR data.

7.3 Conclusions for Gamma Naught stability analysis carried out for Amazon Rainforest and Boreal Forest- Canada.

This study aims at assessing the stability of the gamma naught for Amazon rainforest and Boreal forest during the time period 2015-2017. Intra-annual and inter-annual comparisons of gamma naught values were done and results are reported here for both C- and L-band using available SAR data of Sentinel -1A, 1B and ALOS-2 PALSAR mosaic data.

Using C-band data, average gamma naught value of Amazon rainforest is estimated as $-5.88 \pm 0.29 \text{ dB}$ in co-pol (HH, VV) and $-11.95 \pm 0.29 \text{ dB}$ in cross-pol (HV, VH) respectively. These values are found to be similar to the results obtained for Amazon rainforest using RISAT-1 MRS mode data for the study period 2014-2015 (Sharma, et al., 2017). The average gamma naught values of Amazon rainforest for rainy season are $-5.86 \pm 0.51 \text{ dB}$ & $-11.96 \pm 0.46 \text{ dB}$ and $-5.83 \pm$

0.55 dB & -11.93 ± 0.43 dB for dry season for co-polarisation and cross-polarization data respectively. Seasonal variation of 0.03 dB in co-pol (HH, VV) and 0.03dB in cross-pol was observed. The seasonal variation in gamma naught value is found to be minimal for C-band data. Using L band mosaic product, average gamma naught values of Amazon rainforest estimated - 6.23 ± 0.08 dB in co-pol & -10.67 ± 0.03 dB in cross-pol respectively. Due to non-availability of day wise data, Seasonal analysis were not performed.

In case of Boreal forest, the average gamma naught value for these years is found to be - 8.16 ± 0.53 dB in co-pol & -14.18 ± 0.89 dB in cross-pol. Average summer season gamma naught values are calculated as -7.5 ± 0.43 dB & -13.5 ± 0.22 dB for co-pol and cross-pol respectively. Estimated average gamma naught values for winter season are -8.5 ± 0.66 dB for co-pol data and - 15.5 ± 0.49 dB for cross-pol data. Seasonal variation of 1.73 dB in co-pol and 2.27 dB in cross-pol was observed. Using L band mosaic product, calculated gamma naught values are -6.59 ± 0.23 dB in co-pol and -12.77 ± 0.46 dB in cross-pol. Due to non-availability of day wise data, Seasonal analysis were not performed. From the above analysis, we concluded that boreal forest is stable since 2015 – 2017. The second objective of the study is the quantitative comparison of the C and L band results. The mean gamma values of C and L band results are -8.16 ± 0.53 dB & -14.18 ± 0.89 dB and -6.59 ± 0.23 dB & -12.77 ± 0.46 dB respectively which shows higher value for C-band than L-band.

The comparatively mean gamma values of Amazon rainforest for C and L band are - 5.88 ± 0.29 dB & -11.95 ± 0.29 dB and -6.23 ± 0.08 dB & -10.67 ± 0.03 dB respectively. The gamma values obtained using C band data are true and significant because near to real time data is available, while in L band the data used was the mosaic product of real time data and in-depth studies cannot be performed.

From this analysis, it can be concluded that Amazon rainforest is stable during the study period 2015 - 2017 and can be continued to be used as a calibration site for SAR data. Canadian boreal forest has the seasonal dependence and the variation was found to be more for cross-polarization (2.27 dB) than for co-polarization (1.73 dB) for C-band. Gamma naught stability analysis for the study area using available RISAT-1 data is in progress.

Acknowledgements

The authors gratefully acknowledge the encouragement and guidance received from Shri D. K. Das, Director, SAC. Authors express their sincere gratitude to Shri N. M. Desai, Associate Director, SAC, Ahmedabad for his support to carry out this activity. Thanks are also due to Deputy Director, EPSA, Dr. Raj Kumar for providing his critical comments for the improvement of the study. Authors would also like to thank former Director, Nirma University, Dr. Alka Mahajan for her support throughout the study. Authors gratefully acknowledge the encouragement and support received from Director, Nirma University, Dr. R. N. Patel. Authors also thankfully acknowledge the cooperation and technical help received from Shri V. M. Ramanujam and Shri Raghav Mehra for this activity.

References

1. Alexander, G Fore, D Chapman Bruce, and P Hawkins Brian. *UAVSAR Polarimetric Calibration*. California: California Institute of Technology, 2014.
2. Abhisek, Maiti, Kumar Shashi, and Tolpekin Valentyn. "Polarimetric Calibration of SAR by using Man-made Point Targets and Uniformly Distributed Natural Targets." 2019.
3. Ainsworth, T.L., and Ferro-Famil. "Orientation angle preserving a posteriori polarimetric sar calibration." *IEEE Transactions of Geoscience and Remote Sensing*, 2006.
4. "Canadian Boreal forest." *Canadian Boreal forest wikipedia*.
5. Chen, Xi, Wu Tao, and Zhong Xueliang. "Airborne Polarimetric SAR Experiments with Different Crosstalk Calibration Techniques." Chengdu: CIE International Conference on Radar- IEEE, 2011.
6. Dadhich, Gautam, Shweta Sharma, Mihir Rambhia, Alope K Mathur, P.R Patel, and Alpana Shulka. 2018. "Image Quality Characterization of Fine Resolution RISAT-1 data Using Impulse Response Function." *Geocarto International*, 2018.

DOI: 10.1080/10106049.2017.1421715
7. Freeman, A. 1994. *Radiometric Calibration of SAR Image Data*. California: Jet Propulsion Laboratory.

8. Freeman, A, T.C Dubois Curlander, and Klein J.D. 1988. *SIR-C Calibration Workshop Report*. workshop report, Centre for Radar studies-JPL.
9. Freeman, A. *Radiometric calibration of SAR image Data*. California: Jet Propulsion Laboratory, California Institute of Technology, 1995.
10. Garthwaite, M.C, S Nancarrow, A Hislop, M Thankappan, J.H Dawson, and S Lawrie. 2015. *The Design of Radar Corner Reflectors for the Australian Geophysical Observing System: A Single Design Suitable for InSAR Deformation Monitoring and SAR Calibration at Multiple Microwave Frequency Bands*. work report, Canberra: Geoscience Australia.
11. Hub, ESA. *Level-1 GRD products and IWS GRD resolution*. www.sentinel.esa.int/web/sentinel/home.
12. Hogenson, Kirk. "Prototyping Radiometrically Terrain Corrected Sentinel-1 Data at the Alaska satellite Facility." *UAF- Alaska Satellite Facility, NASA*.
13. Isoguchi, Osamu. "PALSAR radiometric and geometric calibration." *IEEE Transactions on Geoscience and Remote Sensing*, 2010.
14. Masanobu Shimda, Noriyuki Kawano, Manabu Watanabe, Takeshi Mottoka, and Mastsu Ohki. "Calibration and Validation of the PISAR -L2." JAPAN: Asia Pacific Conference on Synthetic Aperture Radar (APSAR), 2013.
15. Quegan, Shaun. "A Unified Algorithm for Phase and Cross talk Calibration of Polarimetric Data-Theory and Observations." *Transactions on Geoscience and Remote Sensing, IEEE* 32, no. 1 (1994).
16. Ronald, J Muellerschoen, Chapin Elaine, and Alex Fore. *Recent Airborne SAR Calibration Results Using the Rosamond Array for P, L, and Ka-band Data*. CEOS SAR CAL VAL, 2015.
17. *Rainforest.mongabay*. http://rainforest.mongabay.com/amazon/rainforest_ecology.html.
18. SANTORO, MAURIZIO. *Estimation of Biophysical Parameters in Boreal Forests from ERS and JERS SAR Interferometry*. Sweden: Department of Radio and Space Science CHALMERS UNIVERSITY OF TECHNOLOGY, 2003.

19. Shimada, M. 1996. "Radiometric and Geometric calibration of JERS-1 SAR." *Advance Space Research*.
20. Sharma, Shweta, et al. "Radiometric calibration stability assessment for the RISAT-1 SAR sensor using a deployed point target array at the Desalpar site, Rann of Kutch, India." *International journal of Remote Sensing* 38, no. 23 (2017): 7242-7259.
21. Shimda, M. "Long-term stability of L-band normalized radar cross section of Amazon rainforest using the JERS-1 SAR:." *Canadian Journal of Remote Sensing*, 2005: 132-137.
22. Shimda, Masanobu. "PALSAR CALVAL Summary (JAXA -PI193)." 2007.
23. Satish K srivastava, Stephane Cote. *Radarsat 1 Image Quality and Calibration Performace Maintained beyond 12 years of Operation*. Ottawa: Candian Space Agency.
24. Thankappan, Medhavy, Mark L. Williams, and John Dawson. 2011. *Corner Reflectors fr the Australian Geophysical Observing systema and Support for calibration of Satellite Borne Synthetic Aperture Radars*. Alaska: Geoscience Australia.
25. Pottier, Eric, Jong Sen Lee, and Laurent Ferro Famil. "Advanced Concepts of Polarimetry." 2007. earth.esa.int/landtraining07/polsar_advanced-concepts.pdf.